Diplomarbeit

Dämpfungsverhalten von vorgespanntem Textilbeton

ausgeführt zum Zwecke der Erlangung des akademischen Grads
Diplom-Ingenieur
eingereicht an der TU Wien, Fakultät für Bau- und Umweltingenieurwesen

---

Diploma Thesis

Damping behavior of prestressed textile-reinforced concrete

submitted in satisfaction of the requirements for the degree
Diplom-Ingenieur
of the TU Wien, Faculty of Civil and Environmental Engineering

Mohammadhossein Azadi, BSc

Matr.Nr.: 01528061

Betreuung: O.Univ.Prof. Dipl.-Ing. Dr.techn. **Johann Kollegger**
Ass. Prof. Dipl.-Ing. Dr.techn. **Philipp Preinstorfer**
Dipl.-Ing. Dr.techn. **Susanne Gmainer**
Institut für Tragkonstruktionen
Forschungsbereich Stahlbeton- und Massivbau
Technische Universität Wien
Karlsplatz 13 / Stiege 2 / 3.OG (Halbstock), 1040 Wien, Österreich

Wien, im April 2024

Preface

It is with great pleasure and a sense of accomplishment that I present this Master's Thesis, the culmination of my academic journey at the Vienna University of Technology. This work represents the culmination of years of dedicated study, research, and intellectual growth, and it is with immense gratitude that I acknowledge the invaluable contributions of those who have guided and supported me throughout this endeavor.

First and foremost, I would like to express my sincere gratitude to Ass. Prof. Dipl.-Ing. Dr. techn. Philipp Preinstorfer for his mentorship, support, and insightful guidance. His expertise and encouragement have been instrumental in shaping the trajectory of my research and academic pursuits. I would like to thank O.Univ.Prof. Dipl.-Ing. Dr.-Ing. M.Eng. Johann Kollegger for allowing me to conduct my research within his research field. I would also like to express my sincere appreciation to Dipl.-Ing. Dr.techn. Susanne Gmainer for her valuable insights and constructive feedback.

I am indebted to my parents for their unwavering support, encouragement, and belief in my abilities. Their sacrifices and love have been the cornerstone of my academic journey, and this thesis is a testament to their lasting influence on my life. To my girlfriend, your support, patience, and understanding have been a source of strength throughout this challenging journey. Your encouragement was the motivation that kept me going in moments of doubt.

Thank you all for being a part of this significant chapter in my academic and personal growth.

Vienna , in April 2024 Mohammadhossein Azadi

Kurzfassung

Beton ist traditionell ein wichtiger Baustoff, der im Allgemeinen mit großen Gebäuden und Infrastrukturen in Verbindung gebracht wird. Mit dem technologischen Fortschritt entstehen jedoch neue Anwendungen für dieses Material. Die vorliegende Arbeit ist das Ergebnis eines Projekts zur Untersuchung der Verwendung von textilbewehrtem Beton (TRC) bei der Herstellung von Skikernen.

Die Textilkomponente von TRC benötigt weniger Betondeckung zur Sicherstellung der Dauerhaftigkeit als konventionelle Stahlbewehrung. Dadurch können besonders schlanke Elemente wie Skikerne hergestellt werden. Die Realisierung dieser innovativen Anwendung erfordert jedoch eine gründliche Untersuchung und Dokumentation der mechanischen Eigenschaften von TRC.

Wenn ein schwingendes System ausgelenkt und wieder losgelassen wird, entstehen Schwingungen, die allmählich abklingen, bis das System zum Stillstand kommt. Ermöglicht wird dies durch die Dämpfung, die die Bewegung durch Dissipation von Energie reduziert, hauptsächlich durch Reibungsvorgänge, die kinetische Energie in irreversible Verlustwärme umwandeln. Trotz des allgemeinen Verständnisses können die Mechanismen im Detail komplex und nur teilweise bekannt sein, so dass für eine genaue Quantifizierung häufig experimentelle Untersuchungen erforderlich sind. Die Entwicklung realistischer Modelle der Dämpfungsmechanismen unter Einbeziehung von Materialparametern ist für ein umfassendes Verständnis unerlässlich und wird in umfassende Modelle schwingender Systeme integriert, in denen die Materialkonstanten experimentell bestimmt werden müssen.

Diese Arbeit beschäftigt sich speziell mit dem dynamischen Verhalten von vorgespannten TRC, wobei der Schwerpunkt auf der Bestimmung des Dämpfungsmaßes (ξ) liegt. Während die Bestimmung des Dämpfungsmaßes von TRC in [1] untersucht wurde, ist das dynamische Verhalten von vorgespannten TRC nach Kenntnis des Autors noch nicht untersucht worden.

Zur Bestimmung des Dämpfungsmaßes von TRC wurden Freischwingversuche durchgeführt. Es wurden verschiedene Probekörper mit unterschiedlichem Bewehrungsgrad, Vorspannkraft und Dicke hergestellt, um den Einfluss der einzelnen Parameter auf das Dämpfungsmaß zu untersuchen. Da der Rissgrad einer der Hauptparameter ist, der das Dämpfungsmaß beeinflusst, wurden alle Proben auf unterschiedliche Rissgrade geprüft. Außerdem wurden Zugversuche durchgeführt, um das Verbundverhalten des TRC zu bestimmen.

Abstract

Concrete has traditionally served as a primary material in construction, commonly associated with large buildings and infrastructure. However, as technology advances, new applications for the material are emerging. This thesis is the result of a project investigating the use of textile-reinforced concrete (TRC) in the manufacture of ski cores.

The textile component of TRC requires less concrete cover to ensure durability than conventional steel reinforcement. This makes it possible to produce exceptionally slender elements such as ski cores. However, the realisation of this innovative application requires a thorough study and documentation of the mechanical properties of TRC.

When a vibrating system is deflected and released, it initiates oscillations that gradually diminish until the system stops, facilitated by damping, which reduces motion by dissipating energy primarily through frictional processes that convert kinetic energy into irreversibly lost heat. Despite a general understanding, detailed mechanisms can be complex and only partially understood, often requiring experimental studies for accurate quantification. The development of realistic models of damping mechanisms, incorporating material property parameters, is essential for a thorough understanding, integrated into comprehensive models of vibrating systems where material constants must be determined experimentally.

This thesis focuses specifically on the dynamic behaviour of prestressed TRC, with particular emphasis on determining the damping ratio (ξ). Whilst there has been research into the determination of the damping ratio of TRC in [1], to the author's knowledge the dynamic behaviour of prestressed TRC has not been investigated.

In order to determine the damping ratio of TRC, free vibration tests were conducted. Different specimens with different reinforcement ratio, prestressing force, and thickness were fabricated to investigate the effect of each parameter on the damping ratio. Since cracking level is one of the main parameters influencing the damping ratio, all specimens were tested for different cracking level. Tensile tests were also conducted to determine the composite behavior of the TRC.

Contents

Symbol Directory

Latin Capital Letters

P	Prestressing force
T_n	Natural period
T_D	Damped period
F_n	Natural frequency
F_D	Damped frequency
$\mathbf{M}$	Diagonal matrix of the generalized modal masse M_n
$\mathbf{C}$	Nondiagonal matrix of coefficients C_{nr}
$\mathbf{K}$	Diagonal matrix of the generalized modal stiffnesses K_n
N_{cr}	Euler's critical buckling load
E_{cm}	Average modulus of elasticity of concrete
I	Second moment of area
K	Effective length factor

Latin Lowercase Letters

k	Spring stiffness
c	Viscous damping coefficient
c_{cr}	Critical damping coefficient
f_D	Damping force
f_S	Spring force
m	Mass
$u(t)$	Displacement
$\mathbf{u}(t)$	Displacement vector
$\dot{u}(t)$	Velocity
$\dot{\mathbf{u}}(t)$	Velocity vector
$\ddot{u}(t)$	Acceleration
$\ddot{\mathbf{u}}(t)$	Acceleration vector
$p(t)$	External force
$\mathbf{p}(t)$	External force vector
t	Thickness of specimen
l	Length of specimen
b	Width of specimen
f_c	Concrete compressive strenght
f_{ct}	Concrete bending tensile strength

Greek Lowercase Letters

ξ	Damping ratio
ρ	Reinforcement ratio
ω_n	Natural angular frequency
ω_D	Damped angular frequency

List of Figures

List of Tables

Chapter 1

Introduction

1.1 Background

Concrete has played a major role in the construction industry over the 120 years as one of the most important building materials. Its durability and compressive strength make it a very reliable building material. However, due to its very low tensile strength, it almost always requires a second material as reinforcement. Steel is currently the most commonly used reinforcement for concrete. However, new materials are beginning to emerge, such as carbon. Carbon can be used as reinforcement in forms such as rebars, which is very similar to steel reinforcement, and textile reinforcement. Textiles are very thin, around 1 mm, and require very little concrete cover, so they can be used to make super-thin reinforced concrete elements. In addition, textiles can be prestressed to achieve better structural properties. The focus of this research is to analyse the dynamic behaviour of prestressed thin textile-reinforced concrete slabs.

1.2 Problem Statement

The damping properties of concrete play a critical role in the dynamic response of structures subjected to external dynamic forces. However, the existing literature lacks a comprehensive investigation of how prestressing and textile reinforcement together affect the damping behavior of concrete. This research addresses this gap by investigating the effects of prestressing and textile reinforcement on the damping characteristics of concrete structures.

1.3 Objectives of the Study

The purpose of this study is to investigate and quantify the effect of prestressing, reinforcement ratio, and crack level on the *damping ratio* (ξ) and *damped natural frequency* (F_D) of thin prestressed textile-reinforced concrete slabs.

1.4 Limitations of the Study

To determine the damping ratio, only free vibration tests are performed. The free vibrations are caused by a initial displacement induced by a weight. The level of cracking has also been taken into account by increasing the initial curvature applied to the specimens. This study is based on a macroscopic perspective where the damping of individual material components is aggregated. The concrete specimens are all the same composition and belong to the HPC (high performance concrete) category. The textiles used are also the same and are made of carbon.

1.5 Thesis Organization

The subsequent chapters of this thesis are organized to provide a comprehensive exploration of the research study:

Chapter 2: Theoretical Framework establishes the theoretical foundation for the study, integrating key concepts and theories related to damping behavior, prestressing, and textile reinforcement. The theoretical framework guides the subsequent empirical investigations and provides a basis for interpreting the results.

Chapter 3: Materials and Methods details the methodology used for data collection and analysis, and describes the selection of materials, specimen preparation, and test equipment used. It provides a clear and detailed account of the procedures followed to ensure the validity and reliability of the study.

Chapter 4: Results and Discussion presents the empirical results obtained from the experimental investigations and examines the damping characteristics of prestressed textile-reinforced concrete. It analyzes the influence of prestressing, reinforcement ratio, and cracking level. In the discussion section, the results are critically interpreted and compared with theoretical predictions.

Chapter 5: Conclusions summarizes the key findings, contributions to the field, and their practical implications.

Appendices includes relevant supplementary materials such as detailed test data, additional figures, and tables.

Chapter 2

Theoretical Framework

2.1 Textile-Reinforced Concrete (TRC)

Steel has been the primary reinforcing material for concrete structures for more than hundred years. Despite the inherent strengths of concrete, such as its stiffness and robustness, the heavy nature of these steel-reinforced structures limits the feasible dimensions and designs of concrete elements. In addition, steel reinforcement is susceptible to corrosion, which can lead to deterioration of the concrete by reducing the effective cross-sectional area of the reinforcement, thereby increasing stress levels within the structure. A modern alternative to traditional steel reinforcement is the use of textile reinforcement, which promises improved durability and reliability for civil engineering projects [2].

Textile-reinforced concrete (TRC) is a novel composite material that integrates a cement-based matrix with non-corrosive fabric, showcasing superior mechanical attributes and an enhanced capability to bear loads. As such, TRC is highly favored for a broad array of structural purposes [3].

Defined by its incorporation of textiles as internal reinforcement, TRC employs textiles composed of long, woven, knitted, or non-woven fiber rovings arranged in at least two directions and set within an inorganic, fine-grained binder, usually cement-based. Fig. 2.1 depicts a detailed cross-section of TRC [4]. This material is well suited for the manufacture of thin, structurally sound components with intricate geometries [2]. TRC offers a significant advantage over conventional steel-reinforced concrete by eliminating the risk of electrochemical corrosion from salt ions present in certain environments [2] [5].

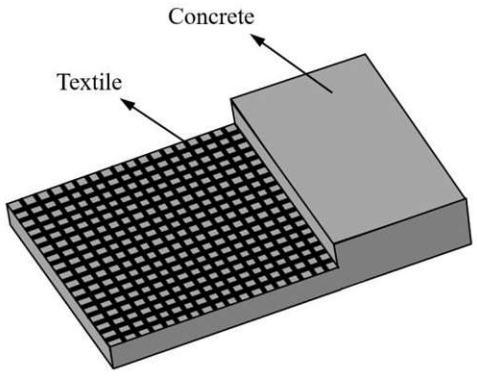

Fig. 2.1: "Step-wise cut through a TRC cross-section" (Adapted from [4])

2.1.1 Textile Manufacturing

Traditionally linked with clothing and domestic use, textiles now find extensive application across various industrial sectors. The production of robust reinforcing materials frequently employs fibers like glass, carbon, aramid, and basalt, renowned for their superior mechanical properties, including strength and modulus, which can match or surpass those of metals. This shift necessitates the adaptation of textile machinery to process these highly stiff, high-strength fibers efficiently [2].

2.1.1.1 Yarn Structures

In textile structures, a variety of yarns serve as reinforcement, selected for their superior mechanical properties to fulfill the demands of structural components. Primarily, for core structural uses, yarns of high-strength and high-modulus filaments are utilized. The selection of materials considers factors like mechanical performance, environmental resistance, and affordability. For instance, alkali-resistant glass fibers (AR-glass) are chosen for textile-reinforced concrete due to their excellent alkaline resistance and cost-effectiveness. These reinforcing yarns, applicable in civil engineering, are produced through diverse methods, such as cabling, friction spinning, and commingling [6]. In most cases, however, rovings are utilized for the production of textiles.

2.1.1.2 Planar Textile Structures

The creation of textile structures for reinforcing composite materials involves various textile techniques. These structures, known as planar textile structures, consist of fibers or yarns arranged flatly to carry loads in one or multiple directions. Specifically oriented yarns within these structures are ideal for reinforcing composites, as they align with the direction of applied forces [2]. The quantity of yarns used can be adjusted based on the tensile strength requirements of the composite [7]. The characteristics of fabrics are determined by several key aspects: the configuration of their components, the density of these elements per unit of width, how they are organized relative to each other, and the type of bonding between them, such as the frictional forces [2].

The key benefit of utilizing textile fabrics for composite reinforcement lies in the ability to tailor their properties across a wide spectrum. This customization is primarily enabled through various manufacturing technologies. The principal techniques for creating textile fabrics are [2]:

- weaving,
- knitting,
- and nonwoven technology.

Until recently, woven fabrics held a predominant role across various textile applications, largely due to traditional practices in garment and other textile product manufacturing, including reinforcement fabrics for composite materials. However, other textile technologies are now increasingly recognized and utilized in the production of reinforcing structures for composite materials, marking a shift in industry preferences and practices [2].

Woven Fabrics Weaving involves creating textiles by crossing two or more yarn sets on a loom, a specific device for this task. This technique produces fabric by intersecting two yarn or thread groups at perpendicular angles, generating a coherent textile structure. Woven fabrics employed in construction applications are commonly crafted from AR-glass, carbon, or sometimes basalt. Their applications primarily revolve around concrete or plaster reinforcement, geotextiles, and agrotextiles. Fig. 2.2 illustrates the weaving process [2].

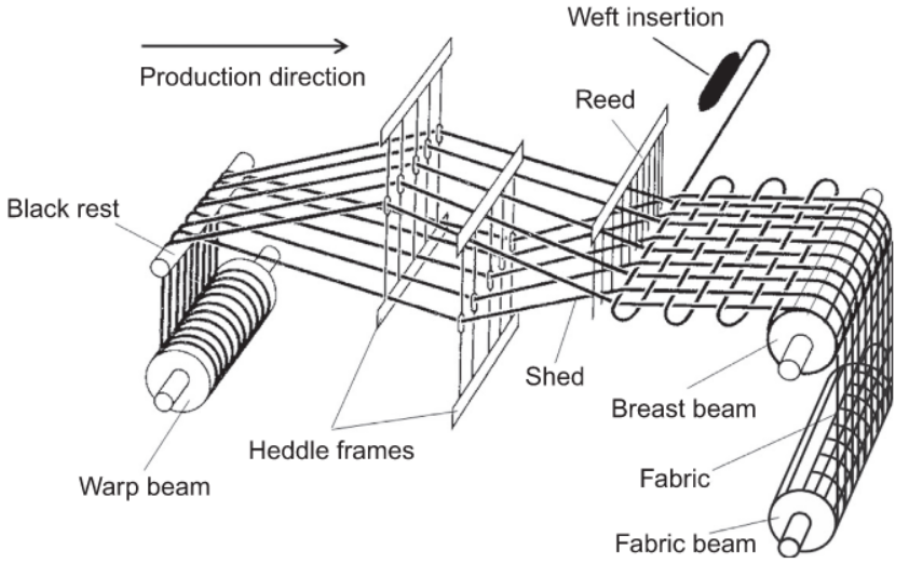

Fig. 2.2: "The weaving process" (Adapted from [2])

Knitted Fabrics Knitting fabric involves creating interlinked loops from one or more yarns, incorporating elements like open and closed laps, floats, and insertion of weft and warp yarns. This technique divides into two primary categories based on the knitting method: weft knitting, where loops form in a horizontal direction, and warp knitting, characterized by vertical loop formation [8], see Fig. 2.3. Fabric characteristics, such as elasticity, thickness, density, and texture, can be tailored for specific needs, from stretchable to non-stretchable and from lightweight to heavy-duty. Modifying the knit pattern allows for adjustments in strength, rigidity, and material efficiency. Depending on the intended application and production technique, different knitting patterns are employed to craft reinforcement structures, optimizing them for their specific use cases [2].

Nonwoven Fabrics Nonwoven fabrics are made from fibers that are not woven or knitted but rather entangled and bonded together through chemical, mechanical, or thermal methods. These materials are notable in civil engineering for their uniformity and porosity, offering unique advantages such as isotropic properties, which mean they have uniform strength and stretch in all directions [2].

2.1.1.3 Coating of Textiles (Impregnation)

Textile coating aims to stabilize and shape the internal structure of textiles, fixing their form. This process also enhances the tensile strength of textile-reinforced components by activating the inner filaments of the rovings. Typically, the coating is applied to thoroughly impregnate the entire roving, ensuring uniform strength and stability throughout the textile [2].

Without impregnation, concrete only infiltrates the exterior of the roving, engaging only a portion of the filaments with the concrete. At the core of the roving lies a less stressed zone, disconnected from concrete contact, potentially leading to roving pull-out failures. Impregnation ensures a uniform distribution of load across filaments, enhancing load endurance and the reaction of the component to stress. Impregnation lines for textile reinforcement typically comprise a raw material storage, impregnation section, drying area, and a storage for semi-finished goods [2].

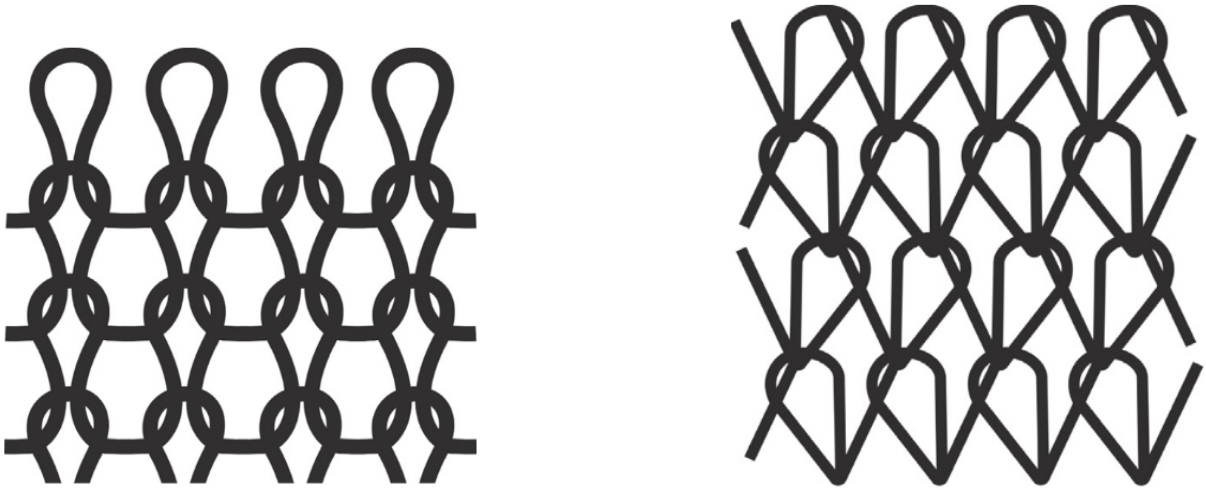

(a) "Weft-knitted structures" **(b)** "Warp-knitted structures"

Fig. 2.3: "Knitted structures" (Adapted from [2])

Fig. 2.4 shows the application of coating using a foulard, among techniques like knife-blade, transfer, and kiss coating. In this method, the textile goes through a resin dip, with rollers adjusted according to the thickness of textile for complete saturation. Another set of rollers then eliminates surplus resin. The fabric undergoes drying or curing in a heated area and is rolled up in a continuous operation. For textiles with rigid polymer coatings, this process also allows molding and hardening into precise shapes[2].

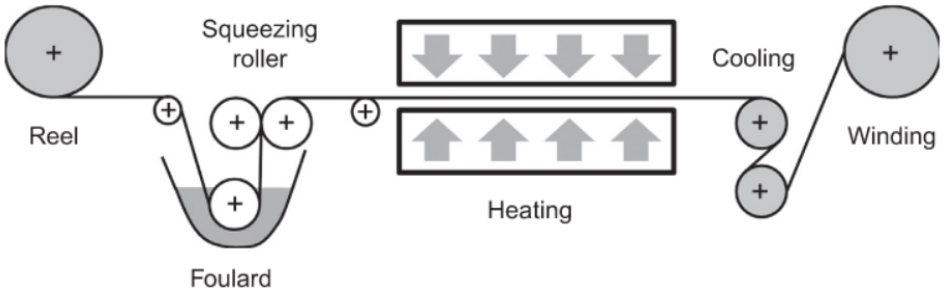

Fig. 2.4: "Schematic layout of the coating process" (Adapted from [2])

2.1.2 Matrix

Not only the properties of textile-reinforcement play an important role in the production of TRC but also the surrounding cementitous matrix. The matrix should meet the specific requirements to assure a solid embedding of the textile reinforcement. Due to the specific geoemtry of the textiles and the thin elements produced of TRC the maximum aggregate size of the concrete also has to be limited [9]. As defined in [10] such concrete with a maximum aggregate size of 4 mm are called mortars. In the literature and also in this thesis, this mortar is called concrete because of its similar properties to high performance concrete (HPC) and also because the matrix is used as structural concrete [9].

The fine concrete used in TRC must align with specific standards regarding the chemical compatibility with fiber materials, the rheological characteristics of the fresh concrete, and its

hardening process which is influenced by the chosen production technique. Spray techniques and lamination are often applied, with the latter being utilized to create the samples in this thesis. The fine concrete matrix is required to form a strong bond with both the reinforcing framework and any existing concrete substrate, while also meeting baseline tensile and compressive strength criteria. Fig. 2.5 illustrates the unbroken interface within the filaments of a dry carbon yarn embedded in a cement paste matrix, highlighting the effective integration and interaction between the carbon yarn and the surrounding cementitious material. For the application of reinforcement layers on overhead and vertical surfaces, the sprayed mixture must exhibit significant cohesion and adhere firmly to the substrate, particularly for multi-layered setups. Additional criteria must be considered for the fine concrete matrix based on the exposure conditions of the reinforcement layer [9].

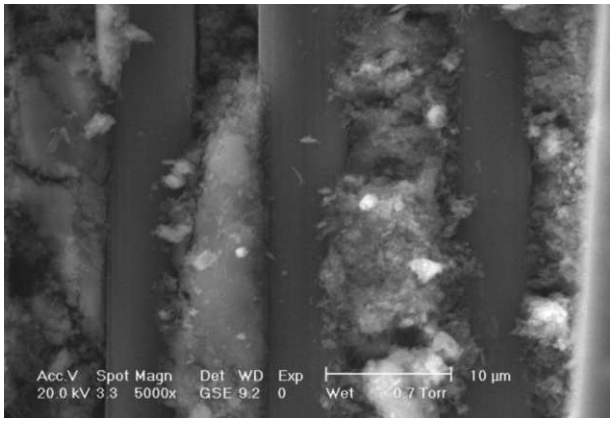

Fig. 2.5: "Morphology of the interphase between cement matrix and dry carbon fiber yarn after 360 days of accelerated aging" (Adapted from [9])

Fine concrete matrices distinguish themselves from traditional concrete through their high binder and fine aggregate content, essential for thoroughly encapsulating and penetrating multi-filament yarns to secure the bond with textile reinforcement. Typically, only the outer filaments of the yarns achieve full binder adhesion due to their packing density, aiding in the formation of a bond via hydration products. Inner filament strength is activated by friction. As mentioned earlier, applying an impregnating layer during textile production can enhance force transfer at filament interfaces, influencing the crack patterns of composite and stress-strain behavior. Fine concrete particles enter the edge filaments of yarn micrometer-scale interstices, varying with the coating type and amount [9].

Ensuring the fine concrete matrix is workable is crucial. Its consistency must be adjustable from soft to flowable, based on the application method, to embed the multifilament yarns in the reinforcement textile effectively. The matrix should be easily mixed, pumpable, and sprayable with standard equipment without causing segregation. The choice of maximum aggregate diameter is influenced by the geometric characteristics of the textile reinforcement, such as the opening width of grid structure, the spacing of layers, and the necessary surface coverage [9].

2.1.3 Testing and Mechanical Behavior

2.1.3.1 Tension Tests

Numerous studies have explored the load-bearing behavior of TRC. In Kadi et al. [11], tensile tests and four-point bending tests were specifically investigated. The methodology and outcomes of this research will be briefly outlined herein as discussed in Vervloet et al. [12].

The schematic representation of the tensile test setup can be found in Fig. 2.6a, with clamp specifications as detailed in RILENTC 232-TDT [13]. Each clamp is secured with six bolts tightened using a torque wrench. To minimize slippage, an additional pin is inserted through the thickness of specimen at the midpoint of the clamps. To safeguard the specimens from damage, rubber sheets approximately 5 mm thick are placed between them and the clamps. The tests are typically conducted with a consistent rate of 1 mm/min. The dimensions of the specimens tested in [12] are: $450 \times 59 \times 22$ mm (length/width/thickness). Fifteen specimens underwent tension testing.

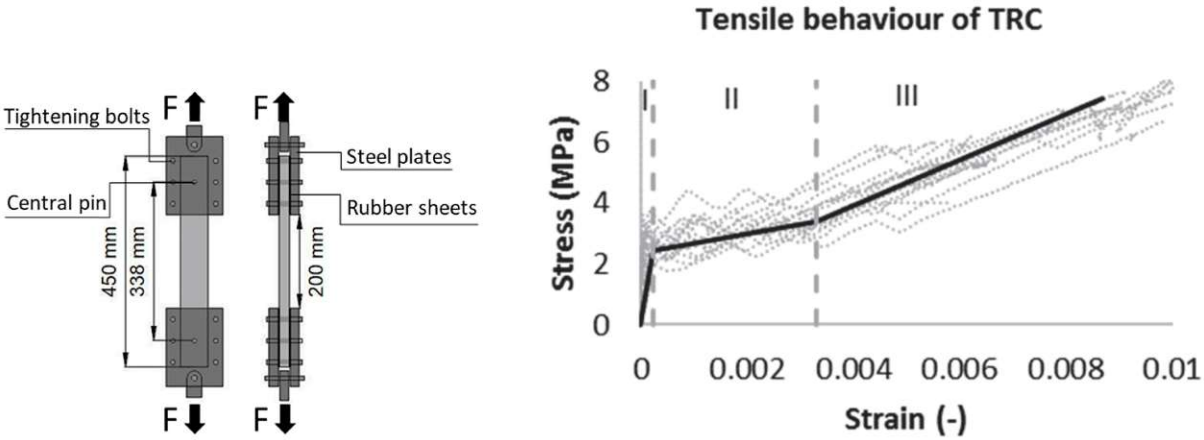

(a) Tensile test setup **(b)** Experimental stress-strain curves

Fig. 2.6: Tension Tests (Adapted from [12])

The stress–strain behavior obtained is illustrated in Fig. 2.6b, revealing distinct stages denoted by I, II, and III.

Stage I (Pre-cracking) In the pre-cracking stage, where the specimen remains uncracked the compound action of the matrix and textiles yielded an E-modulus of 10.7 GPa.

Stage II (Cracked Stage) When the matrix cracking stress of 2.28 MPa was reached, the material entered the second phase, characterized by the formation of multiple cracks until a state of crack saturation was reached at a strain level of 0.0033, resulting in an effective modulus of elasticity (E-modulus) of 0.34 GPa.

Stage III (Saturation crack) In the post-cracking third stage, the behavior was predominantly governed by the textile reinforcements, achieving an E-modulus of 0.75 GPa and an ultimate stress of the component of 7.43 MPa. These figures are the mean values derived from testing 15 specimens and were used to generate the average tri-linear tensile stress–strain curve illustrated in Fig. 2.6b.

2.1.3.2 Textile Pullout Tests

In Sueki et al. [14] the bond behavior of TRC has been investigated. Pullout experiments were carried out to assess the impacts of textile type, cement mixture design, and processing methods. Textile embedded in the cement matrix, comprising up to eighty yarns, were subjected to testing at a rate of 0.25 mm/s. The test setup is illustrated in Fig. 2.7a. The results will be briefly discussed here.

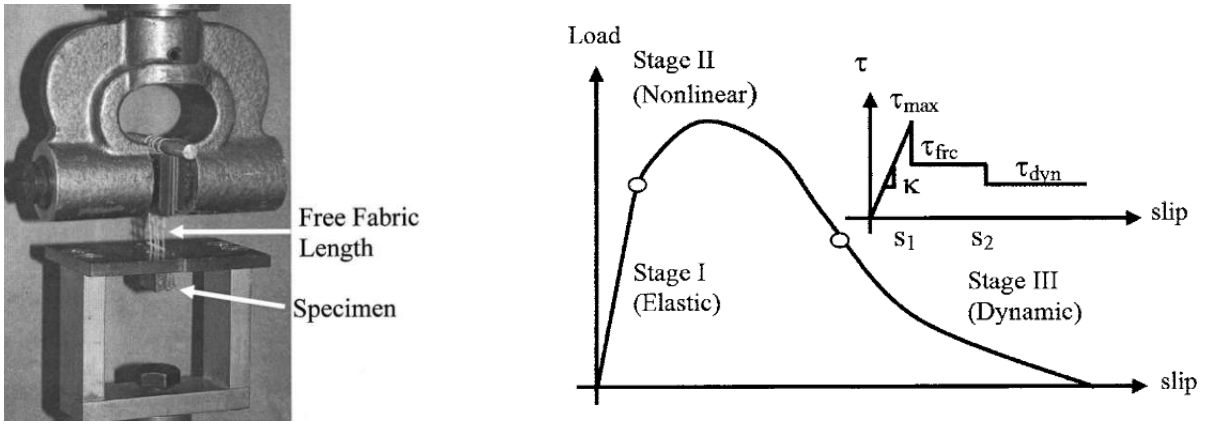

(a) Fabric pullout setup **(b)** Load-slip diagram

Fig. 2.7: Textile pullout tests (Adapted from [14])

The fundamental parameters of the pullout model are characterized by four variables: 1- Initial stiffness of the pullout curve, 2-Ultimate load, 3-Slip at ultimate, and 4-Toughness assessed up to the ultimate load, as depicted in Fig. 2.7b. The initial stiffness is determined from the slope of the linear portion of the curve. In instances involving textile materials, the pullout response may exhibit multiple peak loads. Toughness is quantified by the area under the pullout-slip curve. It is important to note that these parameters, rather than being inherent material properties, are contingent upon factors such as fiber length, diameter, and testing conditions. The three stages shown in Fig.2.7b are as follows:

Stage I (Elastic) Here, the linear behavior of textile bond is evident.

Stage II (Non-linear) The ultimate load is reached in this stage, and a decrease in force is visible afterward.

Stage III (Dynamic) In this stage, textile loses its force-bearing capability, meanwhile the displacement is increasing.

2.2 Damping

When a vibrating system is deflected and then released, it initiates oscillations that gradually decrease until the system comes to a halt. This process is facilitated by a phenomenon known as *damping*, which effectively reduces the motion of the system by dissipating the inherent energy. When external energy is introduced, such as through periodic force excitation, the system achieves a steady state of vibration where the applied energy is balanced by the energy dissipated [15].

The dissipation of energy primarily stems from frictional processes, where friction converts kinetic energy into heat, which is then irreversibly lost. Although the basic principles behind damping are generally understood, the detailed mechanisms can be complex and are sometimes only partially grasped. To accurately quantify these mechanisms, experimental studies on similar components or structures are often necessary [15].

Damping is attributed to both internal and external forces that arise or are induced by the motion of system. For a thorough understanding, it is beneficial to develop models that realistically depict the damping mechanism. These models are phenomenological and incorporate parameters that are interpreted as material properties. Such a damping model is integrated into a comprehensive model of the vibrating system, and the material constants specified within the damping model must invariably be determined through experimental methods [15].

In Section 2.2.1, the different types of damping are briefly discussed. Further discussion on the principles of theoretical modeling for dynamic systems is provided in Section 2.2.2, following the insights from Peterson and Werkle [15]. The derivation of motion equations, as outlined in Chopra [16], is addressed in Section 2.2.3, which also explores various types of motion. The thesis proceeds to Section 2.2.4, presenting an overview of modal analysis, including the shift from multi-degree-of-freedom (MDOF) systems to single-degree-of-freedom (SDOF) systems, as detailed in Chopra [16].

2.2.1 Types of damping

Damping is often divided into internal and external damping, or alternatively, material and system damping, based on whether the conversion of energy from reversible to irreversible forms occurs inside or outside the body in question. Hence, damping forces can come from within the vibrating system or from its environment [17].

Material damping involves the dissipation of energy within a material continuum and represents the intricate process by which kinetic and potential (strain) energy in a vibrating mechanical system is converted to thermal energy. Material damping is further divided into dynamic and static hysteresis damping [17].

Structural damping includes damping events that occur at the interfaces of different material particles within the material or between different materials within a structure [17].

System damping captures damping events that occur at the boundaries or within the domain of influence of a continuum. The energy dissipated by system damping is not lost within the material of the vibrating body, but rather in its immediate vicinity. This situation is common in support structures where vibration energy is dissipated through the ground, through friction in bearings, or through the use of artificial damping mechanisms [17].

2.2.2 Theoretical Modelling [15]

2.2.2.1 Basic concepts

To model the structures from real life into a solvable mathematical model, which is called mathematical modelling, one needs different model for different phenomena happening in the structure. To ensure precise calculation, the modelling has to be accurate. Fig. 2.8 shows the basic models used in the dynamic analysis of structures. Each of these models assumes a mathematical relationship between the force in the element f and the displacement u in the element or the velocity $\dot{u}$.

Hooke's model (Linearly elastic system) The Hooke's model shown in Fig. 2.8a is a spring with a linear characteristic:

$$f_S = k \cdot u \tag{2.1}$$

where k is defined as the stiffness; with a unit of force/length.

Coulomb model The Coulomb model refers to a scenario where a constant frictional force, not dependent on the magnitude of displacement or rotation, is induced as two elements move relative to each other, see fig. 2.8b. Although this law is elementary, its analytical implementation in a vibration model is challenging. The direction of the force is described by the sign of the velocity of the motion coordinate:

$$f_F = \operatorname{sign} \dot{u} \cdot R \tag{2.2}$$

Newtonian model (Linear viscous damping) Fig. 2.8c shows a viscous damper. This is known as the Newtonian model. The damping force f_D is assumed to be proportional to the velocity of the piston. Because of this proportionality between f_D and $\dot{u}$, the damping law is called *linear*; c is the damping constant, which, like the spring constant, is a material property.

$$f_D = c \cdot \dot{u} \tag{2.3}$$

where c is a constant defined as the viscous damping coefficient; with a unit of force $\times$ time/length.

Black Box Finally, Fig. 2.8d shows a "black box" model. This is to indicate that this is a damping mechanism whose effect is somewhat mysterious. This is the case, for example, with hysteretic damping, which is related to distortions in the material. The stress level reached during vibrations influences the amount of damping.

2.2.2.2 Models for the description of material behavior

The models shown in Fig. 2.8 are designed to describe the behavior of different materials more or less accurately in a phenomenological way. Further models can be constructed from these basic models, which are shown in Fig. 2.9. The models are given names: a) Maxwell model, b) Voigt-Kelvin model, c) Burger model, d) Lethersich model, e) Jeffrey model, f) Prandtl-Reusz model, g) Coulomb model. The *Voigt-Kelvin model* serves as the basis for the remainder of this thesis, with systems utilizing this model referred to as *viscoelastic systems*. In the following section, the dynamical behaviour of *viscoelastic systems* will be further explored.

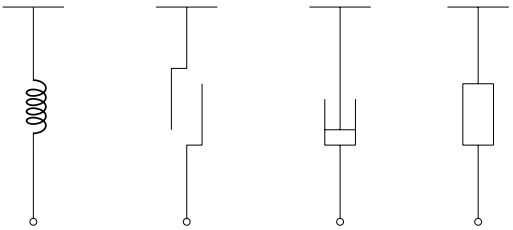

a) Hooke b) Coulomb c) Newton d) Black box

Fig. 2.8: Basic concepts (Adapted from [15])

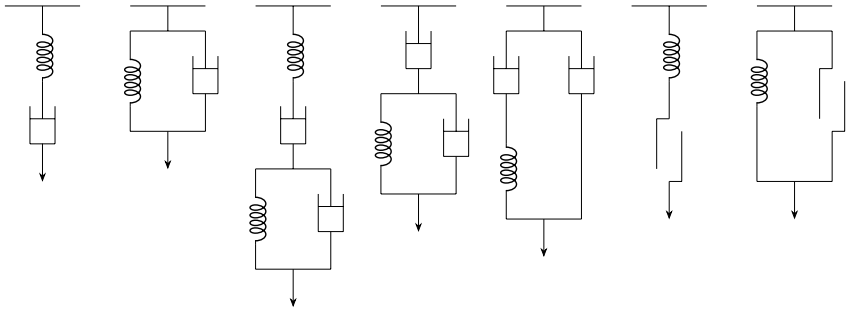

a) b) c) d) e) f) g)

Fig. 2.9: Models for the description of material behavior (Adapted from [15]) a) Maxwell-Model b) Voigt-Kelvin-Model c) Burger-Model d) Letherisich-Model e) Jeffrey-Model f) Prantdl-Reusz-Model g) Coulomb-Model

2.2.3 SDOF Viscoelastic System [16]

A SDOF viscoelastic system is a mechanical or structural system that is characterized by a single independent degree of freedom and exhibits both elastic and viscous damping properties. In such systems, the response to external forces or displacements is governed by a combination of elastic and damping elements. The elastic component is described by Hooke's law, which represents linear spring behavior, while the viscous damping is typically modeled by Newton's law, where the damping force f_D is assumed proportional to the velocity of the system. This viscoelastic behavior introduces time-dependent properties that allow for the consideration of material damping effects. The analysis of SDOF viscoelastic systems is essential for understanding the dynamic response of structures under various loading conditions, making it a fundamental concept in structural dynamics and mechanical engineering.

2.2.3.1 Equation of Motion

Utilizing Newton's second law of motion, the differential equations governing movement will be derived subsequently. The motion equation for a SDOF system, as depicted in Fig. 2.10, is formulated as follows. The diagram in Fig. 2.10b displays the forces at play on the mass at any given moment. These include the external force $p(t)$, the spring force f_S, and the damping force f_D. The positive direction of external force is assumed to be positive along the x axis by standard convention. In a similar vein, the displacement $u(t)$, velocity $\dot{u}(t)$, and acceleration $\ddot{u}(t)$ are considered positive when directed along the x-axis. f_S and f_D, which act in the reverse direction, serve as internal forces that oppose displacement and motion, respectively.

The net force in the x-direction can be written as $p - f_S - f_D$. In accordance with Newton's second law of motion, this yields:

$$\sum F_x = m\ddot{u} \Rightarrow p - f_S - f_D = m\ddot{u} \tag{2.4}$$

The equation could be reformed to a more familiar form:

$$m\ddot{u} + f_D + f_S = p(t) \tag{2.5}$$

Substituting eqs. 2.1 and 2.3 into 2.5:

$$m\ddot{u} + c\dot{u} + ku = p(t) \tag{2.6}$$

Eq. 2.6 describes the behavior of displacement u in the theoretical model shown in Fig. 2.10a. It is presumed that the dynamical structure behaves in a linear elastic manner and experiences the effects of an external dynamic force $p(t)$. Mass is quantified in terms of force per unit of acceleration.

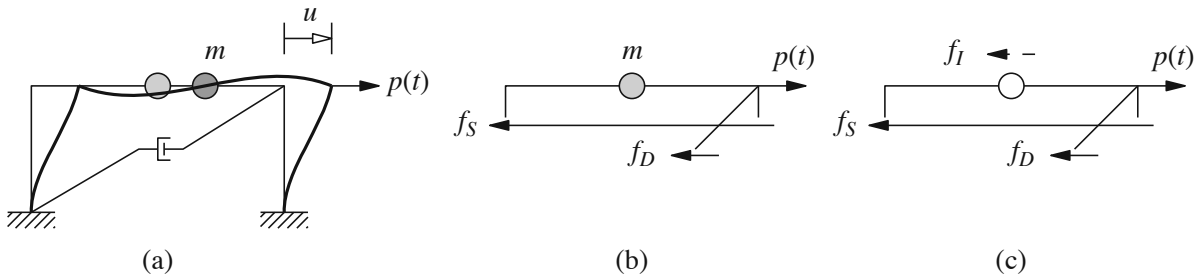

Fig. 2.10: SDOF System (Adapted from [16])

2.2.3.2 Free Vibration

By assigning $p(t) = 0$ in Eq. 2.6, we derive the differential equation that governs the damped free vibration of SDOF systems:

$$m\ddot{u} + c\dot{u} + ku = 0 \tag{2.7}$$

When divided by m and considering $\omega_n = \sqrt{k/m}$ and $\xi = \frac{c}{2m\omega_n} = \frac{c}{c_{\text{cr}}}$, it results in

$$\ddot{u} + 2\xi\omega_n\dot{u} + \omega_n^2 u = 0 \tag{2.8}$$

We will use the term

$$c_{\text{cr}} = 2m\omega_n = 2\sqrt{km} = \frac{2k}{\omega_n} \tag{2.9}$$

to symbolize the critical damping coefficient, whereas ξ denotes the *damping ratio* or the proportion of critical damping (c_{cr}). The damping constant (c) acts as an indicator of the energy dissipated during a cycle of free vibration or throughout a cycle of forced harmonic vibration. Conversely, the damping ratio (ξ), a dimensionless indicator of damping, reflects an intrinsic characteristic of the system that is affected by its mass and stiffness.

2.2.3.3 Types of Motion

Fig. 2.11 illustrates the behavior of the motion $u(t)$ from an initial displacement $u(0)$ across three distinct values of ξ. In scenarios where $c < c_{cr}$ or $\xi < 1$, the system experiences oscillations about its equilibrium point, with the oscillations' amplitude decreasing over time. For $c = c_{cr}$ or $\xi = 1$, the system reverts to its equilibrium state without oscillating. In contrast, for $c > c_{cr}$ or $\xi > 1$, the return to equilibrium is akin to the $\xi = 1$ case, albeit at a reduced pace. The designation of the critical damping coefficient c_{cr} as "critical" is due to it being the threshold value of c at which oscillations are entirely prevented, marking the transition between oscillatory and non-oscillatory behavior.

This thesis primarily addresses underdamped systems ($c < c_{cr}$), as structures of interest typically exhibit damping ratios below 0.10, situating them within this category. While the behavior of critically damped ($c = c_{cr}$) and overdamped ($c > c_{cr}$) systems is not the focus here, it is noteworthy that such systems do occur. For example, overdamped mechanisms are seen in devices like the automatic door closers, while critically damped responses are characteristic of instruments measuring steady-state values, like scales for dead weights. Automobile shock absorbers often have damping significantly less than the critical value ($\xi < 0.5$).

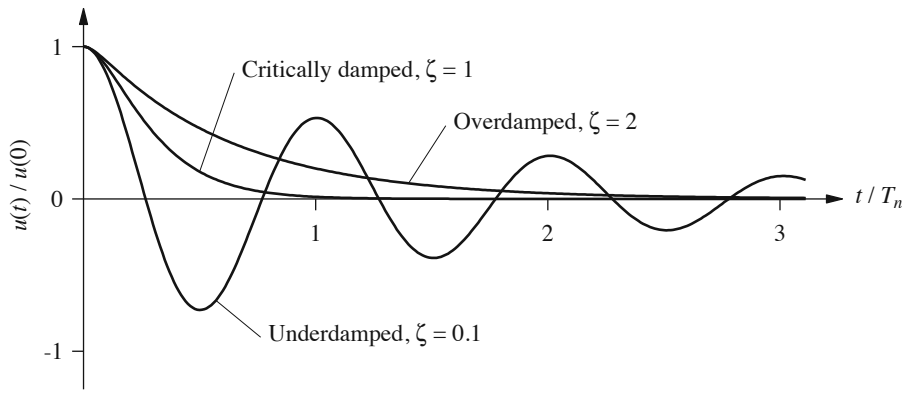

Fig. 2.11: Displacement-time diagram of different types of motion (Adapted from [16])

2.2.3.4 Underdamped Systems

The solution to Eq. 2.7 under the initial conditions of $u = u(0)$ and $\dot{u} = \dot{u}(0)$ for systems with $c < c_{\text{cr}}$ or $\xi < 1$ is expressed as:

$$u(t) = e^{-\xi\omega_n t}\left[u(0)\cos\omega_D t + \frac{\dot{u}(0) + \xi\omega_n u(0)}{\omega_D}\sin\omega_D t\right] \tag{2.10}$$

where

$$\omega_D = \omega_n\sqrt{1-\xi^2} \tag{2.11}$$

Eq. 2.10 is depicted in Fig. 2.12, displaying the free vibration behavior of an SDOF system characterized by a damping ratio $\xi = 0.05$, or 5% compared to an undamped system. The onset of free vibration for both systems is marked by identical initial displacement $u(0)$ and velocity $\dot{u}(0)$, leading both displacement-time graphs to start at $t = 0$ with the same ordinate and initial slope. Eq. 2.10 elucidates that the natural frequency of damped vibration is denoted as ω_D, which is linked to the undamped natural frequency of system ω_n via Eq. 2.11. Furthermore, the natural period of damped vibration, given by $T_D = 2\pi/\omega_D$, is associated with the undamped natural period T_n as follows:

$$T_D = \frac{T_n}{\sqrt{1-\xi^2}} \tag{2.12}$$

In every cycle of vibration, the amplitude of displacement for an undamped system stays uniform, whereas in a damped system, it oscillates with a progressively diminishing amplitude through each cycle. As denoted by Eq. 2.10, the amplitude of displacement reduces exponentially over time, a behavior illustrated in Fig. 2.12. The *envelope curve*, represented by $\pm\rho e^{-\xi\omega_n t}$, where ρ is defined in 2.13, envelops the displacement-time curve peaks.

$$\rho = \sqrt{[u(0)]^2 + \left[\frac{\dot{u}(0) + \xi\omega_n u(0)}{\omega_D}\right]^2} \tag{2.13}$$

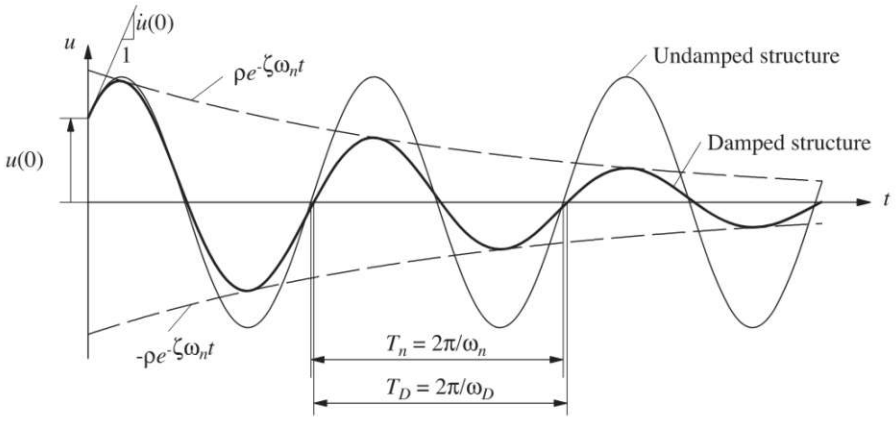

Fig. 2.12: Comparison of free vibration behaviour of a damped and undamped structure (Adapted from [16])

Damping plays a role in decreasing the natural frequency from ω_n to ω_D and in increasing the natural period from T_n to T_D. For damping ratios under 20%, which include the majority of structural cases, these impacts are minor, as illustrated in Fig. 2.13 where the ratio $\omega_D/\omega_n =$

T_n/T_D is graphed versus ξ. In such scenarios, the damped natural frequency ω_D and period T_D are nearly identical to their undamped counterparts ω_n and T_n, respectively. In critically damped systems, where $\omega_D = 0$ and $T_D = \infty$, there is an absence of oscillatory motion, a concept visually represented in Fig. 2.11.

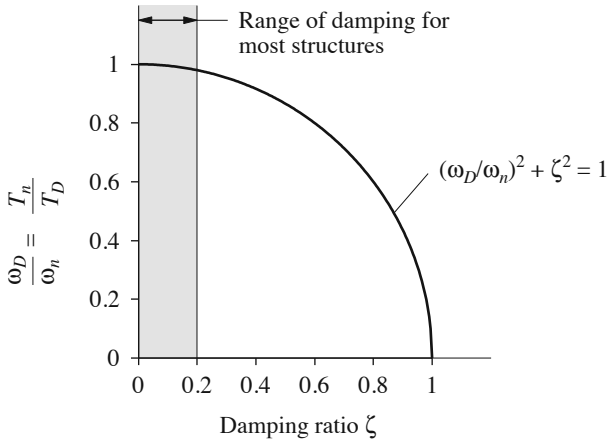

Fig. 2.13: "Effect of damping ratio (ξ) on damped angular frequncy" (Adapted from [16])

Most notable effect of damping is seen in its role in the decay rate during free vibration. This phenomenon is highlighted in Fig. 2.14, showcasing the free vibration originating from the initial displacement $u(0)$ for four systems that share the same natural period T_n but differ in damping ratios: $\xi = 2\%, 5\%, 10\%$, and 20%.

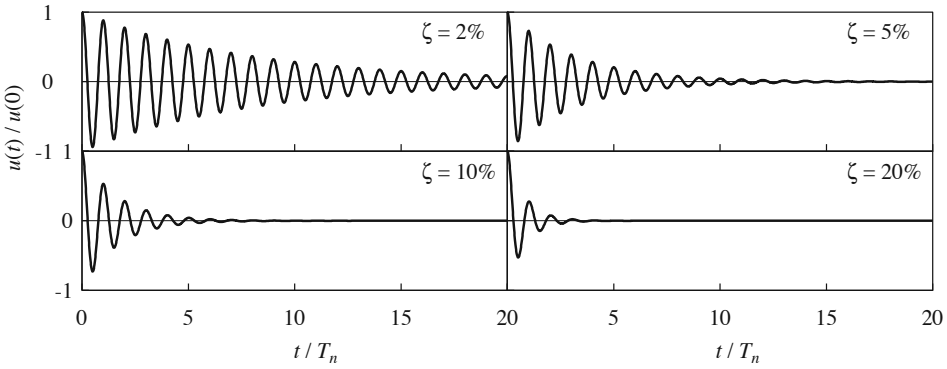

Fig. 2.14: Free vibration of systems with varying degrees of damping (Adapted from [16])

2.2.3.5 Free Vibration Tests

Experiments on free vibration are crucial for identifying the damping ratio (ξ) in real-world structures, as it is not possible to calculate it analytically. These experiments produce results as shown in Fig. 2.15. For systems with light damping, the damping ratio can be ascertained through the use of specific equations:

$$\begin{aligned} \xi &= \frac{1}{2\pi j} \ln \frac{u_i}{u_{i+j}} \\ &= \frac{1}{2\pi j} \ln \frac{\ddot{u}_i}{\ddot{u}_{i+j}} \end{aligned} \tag{2.14}$$

The second equation is analogous but formulated in terms of accelerations, which are simpler to measure compared to displacements. This approach has been proven effective for systems with light damping.

The natural period of system T_D, can also be calculated from the free vibration record by timing the duration needed to complete a single vibration cycle. Comparing this period with the natural period derived from the stiffness and mass of a theoretical model offers insight into the precision of these calculated properties and how well the idealization represents the actual structure.

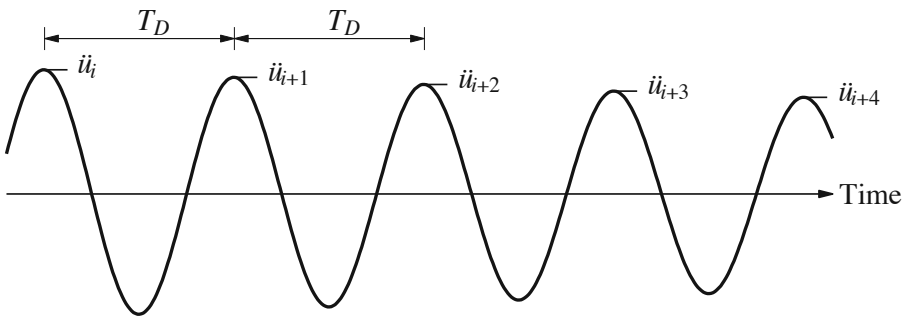

Fig. 2.15: Acceleration-time recording of free vibration test (Adapted from [16])

2.2.4 Modal Equations for Viscoelastic Damped Systems [16]

2.2.4.1 Modal Analysis with Damping

When considering damping in the equations of motion for a MDOF system, the following set of equations is obtained:

$$\mathbf{m}\ddot{\mathbf{u}} + \mathbf{c}\dot{\mathbf{u}} + \mathbf{k}\mathbf{u} = \mathbf{p}(t) \tag{2.15}$$

where $\mathbf{m}$ represents the mass matrix, $\mathbf{c}$ denotes the damping matrix, $\mathbf{k}$ is the stiffness matrix, $\mathbf{u}$ indicates the displacement vector, $\dot{\mathbf{u}}$ indicates the velocity vector ,$\ddot{\mathbf{u}}$ signifies the acceleration vector and $\mathbf{p}(t)$ indicates force vector. By utilizing the transformation:

$$\mathbf{u}(t) = \sum_{r=1}^{N} \phi_r q_r(t) = \mathbf{\Phi}\mathbf{q}(t) \tag{2.16}$$

where ϕ_r denotes the natural modes of the system in the absence of damping [1]. These equations can be reformulated in modal coordinates. Although damping terms may cause the modal equations of damped systems to be coupled, with certain plausible damping idealizations in many structures, these equations can be simplified to become uncoupled, mirroring the behavior of undamped systems [2]. The methodology is outlined below: Substituting Eq. 2.16 into Eq. 2.15 yields:

$$\sum_{r=1}^{N} \mathbf{m}\phi_r \ddot{q}_r(t) + \sum_{r=1}^{N} \mathbf{c}\phi_r \dot{q}_r(t) + \sum_{r=1}^{N} \mathbf{k}\phi_r q_r(t) = \mathbf{p}(t) \tag{2.17}$$

Premultiplying each term by ϕ_n^T results in:

$$\sum_{r=1}^{N} \phi_n^T\mathbf{m}\phi_r \ddot{q}_r(t) + \sum_{r=1}^{N} \phi_n^T\mathbf{c}\phi_r \dot{q}_r(t) + \sum_{r=1}^{N} \phi_n^T\mathbf{k}\phi_r q_r(t) = \phi_n^T\mathbf{p}(t) \tag{2.18}$$

This can be rewritten as:

$$M_n\ddot{q}_n(t) + \sum_{r=1}^{N} C_{nr}\dot{q}_r(t) + K_n q_n(t) = P_n(t) \tag{2.19}$$

where:

$$M_n = \phi_n^T\mathbf{m}\phi_n, \quad C_{nr} = \phi_n^T\mathbf{c}\phi_r, \quad K_n = \phi_n^T\mathbf{k}\phi_n, \quad P_n(t) = \phi_n^T\mathbf{p}(t) \tag{2.20}$$

The collection of N equations can be depicted in a matrix format:

$$\mathbf{M}\ddot{\mathbf{q}} + \mathbf{C}\dot{\mathbf{q}} + \mathbf{K}\mathbf{q} = \mathbf{P}(t) \tag{2.21}$$

Here, $\mathbf{M}$ is a diagonal matrix consisting of generalized modal masses M_n, $\mathbf{C}$ is a nondiagonal matrix filled with coefficients C_{nr}, $\mathbf{K}$ represents a diagonal matrix of generalized modal stiffnesses K_n, and $\mathbf{P}(t)$ is a column vector containing generalized modal forces $P_n(t)$. These N equations, expressed in modal coordinates $q_n(t)$, are interconnected through the damping terms. Nonetheless, in systems characterized by classical damping, these modal equations become independent. In such scenarios, $C_{nr} = 0$ for $n \neq r$, simplifying Eq. 2.19 to:

[1] Refer to section 10.2 in [16] for a detailed explanation of natural modes.
[2] For further details, see section 12.3 in [16].

$$M_n\ddot{q}_n + C_n\dot{q}_n + K_n q_n = P_n(t) \tag{2.22}$$

Here, C_n symbolizes the generalized damping coefficient. Eq. 2.22 is pivotal in modeling the behavior of the MDOF system, as illustrated in Fig. 2.16. Modifying Eq. 2.22 by dividing it by M_n leads to:

$$\ddot{q}_n + 2\xi_n\omega_n\dot{q}_n + \omega_n^2 q_n = \frac{P_n(t)}{M_n} \tag{2.23}$$

ξ_n denotes the *damping ratio for the nth mode*, often derived from empirical data for structures. Eq. 2.22 specifically addresses the nth modal coordinate $q_n(t)$, with the parameters M_n, K_n, C_n, and $P_n(t)$ exclusively reliant on the nth mode ϕ_n, independent of other modes. Consequently, there are N separate equations like Eq. 2.22, each correlating to a distinct natural mode. To encapsulate, the original set of N interrelated differential equations 2.15 concerning nodal displacements $u_j(t)$ has been converted into a collection of N independent equations 2.22 in modal coordinates $q_n(t)$. In the forthcoming Section 4.2, modal analysis will be employed to explore the free vibration of the test samples in its primary natural mode, treating it as an SDOF system, and to measure the damping ratio (ξ_1) as indicated in Eq. 2.14.

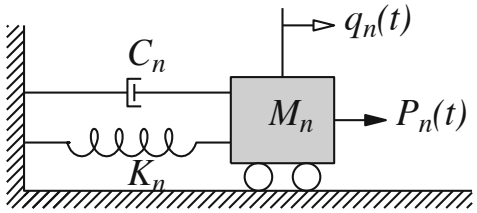

Fig. 2.16: "Generalized SDOF system for the nth natural mode" (Adapted from [16])

2.2.5 Damping Behavior of Concrete

While the damping properties of metallic building materials are well understood from numerous experimental and theoretical investigations, there are still many unanswered questions regarding concrete. In the case of concrete, it is much more difficult to understand the dependence of its damping properties on individual factors due to the considerable dispersion of numerous test results and the greater number of influencing factors compared to steel [17].

As mentioned in Dieterle [17], the factors considered crucial to damping properties in concrete include:

- Frequency
- Magnitude of stress
- Water content of mortar or concrete
- Age of mortar or concrete
- Cement content of concrete

2.2.5.1 Causes of the Internal Damping of Concrete

Dieterle [17] summarizes the reports of Teichen [18] and Ali et al. [19] on the different phenomena that are listed and attributed to different types of damping in concrete:

Material Damping

- *Liquid Friction:* The contribution of liquid friction to the internal damping of concrete components and structures is expected to be significant. Water molecules physically bound between cement gel particles dissipate vibrational energy by molecular diffusion.
- *Plasticization Effects:* Even in the so-called elastic stress range of a homogeneously perceived material, irreversible deformations are possible at the microscopic level (e.g. due to stress concentrations at particle contact points). However, the contribution of plastification effects to overall material damping is likely to be significant only at high stresses.
- *Intergranular Slip:* Disordered material may exist at the grain boundaries of adjacent gel particles, which becomes ordered under stress and dissipates energy. This mechanism is similar to liquid friction at grain boundaries in metals. If the gel particles of cement have a crystalline structure, this mechanism is also expected to contribute to energy dissipation in concrete.
- *Intracrystalline Slip:* This mechanism is expected to occur in both the gel particles of cement and the aggregates of concrete. Under applied stress, crystals can slip along a plane inclined to the crystal axis, thereby dissipating energy.
- *Loss of energy in capillary water:* The phase shift between the movement of the capillary water and that of the surrounding concrete dissipates energy as it vibrates.
- *Diffusion of Mixing Water:* In a vibrating concrete body, different stress states generally exist at different locations. Under such conditions, non-chemically bonded mix water will attempt to diffuse from highly stressed areas to less stressed areas, thereby dissipating energy.

- *Chemical Diffusion:* Gel water contains various dissolved salts. Under different stress conditions, their solubility can change. The dissolved salts will attempt to diffuse from a site of low solubility to a site of high solubility, resulting in energy loss.

Structural Damping

- *Cracking at Adhesion Surfaces:* Vibrational energy can be dissipated during fracture between groups of adjacent particles.
- *Dry Friction:* Dry friction, or Coulomb friction, can result from sliding motion between adjacent particles. The contribution of dry friction to the total material damping depends on, among other things, the stress state.

Measured damping values often do not reveal the nature of the energy dissipation. This is because the direct consequence of the internal processes in the material, namely the loss of vibrational energy, appears only as a general, macroscopic phenomenon. For the desired damping model for concrete structures, this means that it is practically impossible to develop a model composed of different elements that separately account for the numerous possible causes. Instead, a global model has to be found that is based on experimental results and explains them as accurately as possible [17].

2.2.5.2 Damping Behavior of Prestressed Concrete

Damping characteristics of prestressed concrete have been studied in Penzien [20]. The investigation focused on identifying the damping ratio of prestressed concrete beams subjected to dynamic loads. The experiment varied parameters such as the type and intensity of prestress, along with the concrete strength class. Two types of dynamic loadings have been investigated, "steady state harmonic forced vibration" and "free vibration around the static unloaded equilibrium position of beam". Following the application of steady state excitation, each beam was exposed to static concentrated loads of different intensities applied at the midpoint. These loads were then suddenly removed, inducing a condition of free vibration in the beams. It was found that internal damping is significantly influenced by the history of loading and the displacement amplitude. Furthermore, the study highlighted the critical role of concrete cracking in damping, indicating that the degree and type of prestress indirectly affect damping by controlling the extent of cracking. The measured damping ratios varied widely, ranging from 0.5 to 7.0 percent, largely dependent on the level of cracking allowed during each test [20].

The investigation led to several key conclusions regarding the behavior of prestressed concrete members under different conditions [20]:

- In *steady state conditions*, if prestressed concrete members are sufficiently prestressed to avoid the development of tension cracks, internal damping may be less than 1 percent of the critical level. Damping is expected to increase to around 2 percent of critical if microscopic tension cracks occur. Should larger, visible cracks form, a further increase in damping is anticipated.
- The presence of internal damping in prestressed concrete members under *transient conditions* is significantly influenced by the loading history and the magnitude of displacements encountered. For instances where the members have been subjected to dynamic loading a few times, causing considerable cracking, damping levels could vary between 3 to 6 percent of critical.

- The effect of the magnitude and type of prestress on internal damping is indirect, primarily through their role in controlling crack formation.

The study also identifies several areas requiring further investigation for a comprehensive understanding of damping in prestressed concrete systems, including the effects of loading history, support conditions, and vibration frequency on both internal and external damping mechanisms [20].

2.2.5.3 Damping Behavior of TRC

In Çilesiz [1] the effect of loading history (cracking level) on the damping ratio of TRC was investigated. The results obtained in this study are shown in Fig. 2.17. The cracking level was induced by applying a load at the end of the cantilever beam.

Upon closer examination of Fig. 2.17, there is a compelling observation: the applied load has a pronounced effect on the damping ratio. This finding prompts a deeper investigation into the underlying mechanisms at play. The key determinant identified in the study is the cracking level of the concrete specimens. As loads are applied, the concrete is subjected to stresses that lead to crack initiation and propagation. This phenomenon contributes significantly to the dissipation of energy within the material, thereby affecting the damping ratio [1].

There is a direct correlation between the number of cracks in the concrete and the resulting damping ratio. Essentially, the presence of more cracks in the concrete matrix translates into a greater capacity for energy dissipation between those cracks. This, in turn, manifests itself as an increased damping ratio [1].

The following is the labeling of the specimen shown in Fig. 2.17:

PK1-S Specimen number 1	Sanded surface of reinforcement
PK2-S Specimen number 2	Sanded surface of reinforcement
PK3-G Specimen number 3	Smooth surface of reinforcement
PK4-G Specimen number 4	Smooth surface of reinforcement

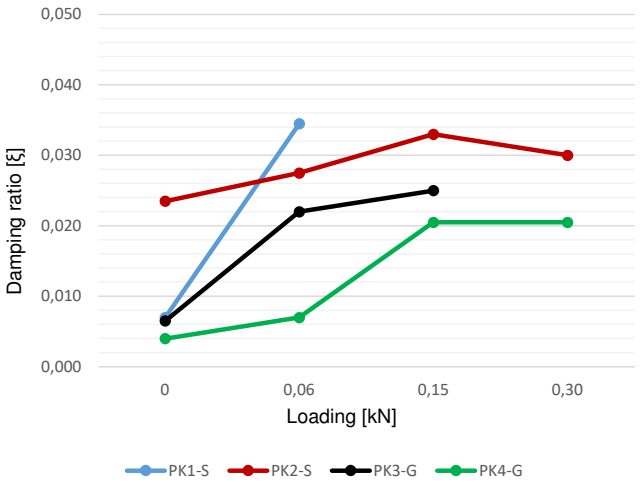

Fig. 2.17: Damping ratio (ξ) vs. load (Adapted from [1])

2.2.5.4 Damping Behavior of Non-Reinforced Concrete

The study in Gidrao et al. [21] investigated the damping ratio of non reinforced concrete in relation to variations in *water-cement ratio* and *aging*. Fig. 2.18 visually illustrates the effect of water-cement ratio on the damping ratio. As the water-cement ratio increases, so does the damping. The study also examines the influence of aging on concrete damping, emphasizing the critical role of water content in determining damping characteristics, as shown in Fig. 2.19. In particular, the damping of cement mortar shows a decrease with increasing mortar age, with a significant reduction observed, suggesting a continuing influence of drying on damping. Interestingly, after about four weeks of curing, the influence of mortar age on damping becomes negligible, adding a temporal dimension to this phenomenon [21].

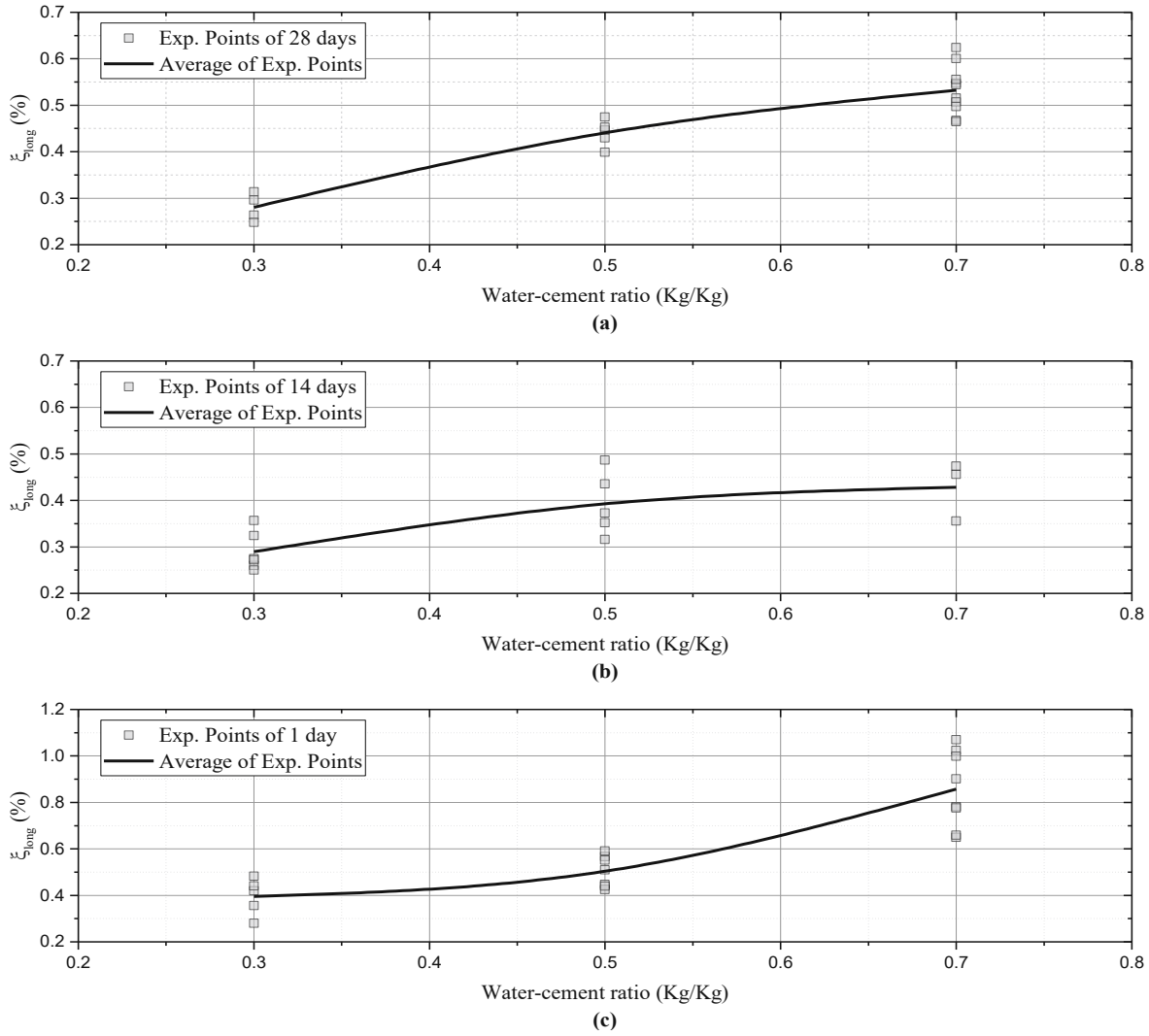

Fig. 2.18: Influence of water-cement ratio on internal damping ratio (ξ) (Adapted from [21])

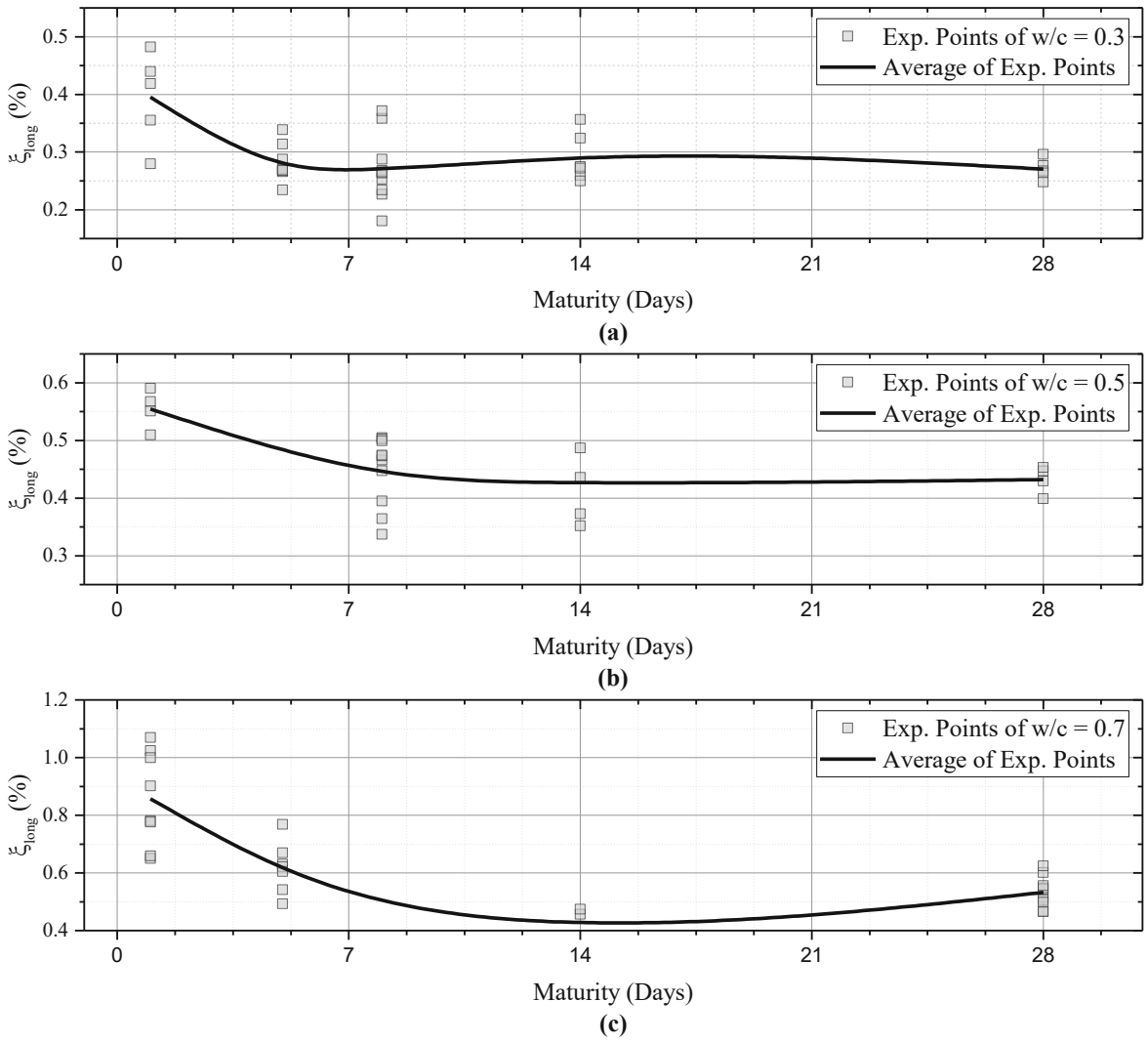

Fig. 2.19: Influence of aging on internal damping ratio (ξ) (Adapted from [21])

Chapter 3

Materials and Methods

3.1 Materials

3.1.1 Matrix

SikaGrout®-3350 is a single-component, cement-based grout with rapid hardening properties, excellent flowability, and shrinkage compensation. It attains exceptionally high early and ultimate strengths. The table 3.1 shows technical information for this product [22]. As suggested in the product data sheet, the mixture of 25 kg of grout with 2 liters of water was used, resulting in a mixing ratio of 8.0%.

Compressive strength	Time	Compressive strength
	1 day	~65 N/mm²
	3 days	~90 N/mm²
	7 days	~100 N/mm²
	28 days	~120 N/mm²
	Compressive Strength class	>C100/115
	Characteristic compressive strength at 28 days	>120 N/mm² (150 x 300 mm cylinders)
Modulus of elasticity in compression	~56000 N/mm²	
Tensile strength in flexure	Time	Strength
	1 day	~10 N/mm²
	28 days	~20 N/mm²
Maximum grain size	≈ 3 mm	

Tab. 3.1: SikaGrout®-3350 - Technical Information (Adopted from [22])

3.1.2 Reinforcement

Sika® CarboDur®-300 Grid is a bi-directional carbon fiber grid utilized for reinforcement and prestressing in specimen production, depicted in Fig. 3.1. Table 3.2 presents the technical specifications of this product [23]. This grid is a robust, bi-directional, non-woven, carbon fiber textile, made more durable by an acrylic resin impregnation. It features a carbon weight of 320 g/m^2. The manufacturer provide nominal values for the ultimate tensile resistance, Young's modulus, and ultimate tensile strain of the textile, detailed in Table 3.2. For the creation of all samples, strips approximately 9 cm wide were employed, achieving a nominal tensile resistance around 17 kN.

Fig. 3.1: Sika® CarboDur®-300 Grid

Fibre orientation	0° / 90°
Fibre type	Carbon fibre.
Dry fibre density	1,8 kg/l
Area Density	320 g/m2 embedded grid.
Modulus of elasticity in tension	∼230 000 N/mm2
Ultimate tensile strain	∼1,9 %
Tensile resistance	>9500 N/5 cm (grid)

Tab. 3.2: Sika® CarboDur®-300 Grid - Technical Information (Adopted from [23])

3.2 Specimen Preparation

3.2.1 Specimen Dimensions

Fig. 3.2 illustrates the dimensions of the specimens, including the placement of textiles and the concrete covering. The specimens featuring a 12 mm thickness and two textile layers (S9-10) are fabricated such that both layers of textile are directly on top of each other, leaving no gap between them. All specimens have a length of 1500 mm.

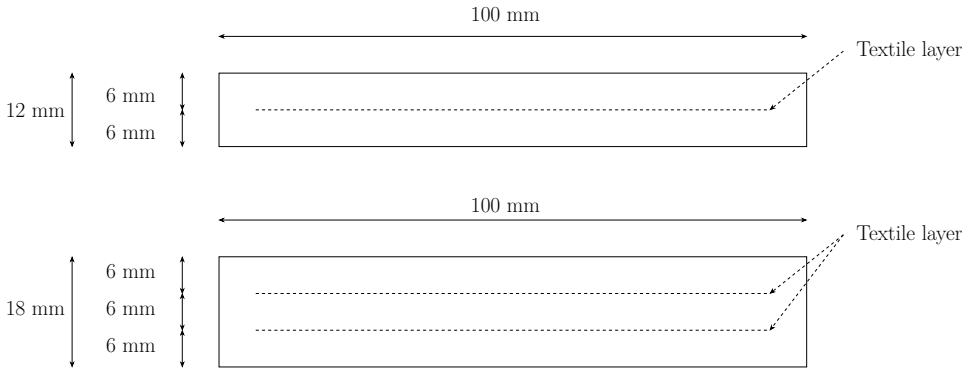

Fig. 3.2: Dimensions of specimens: (top) specimen with a thickness of 12 mm (S1-10), (bottom) specimen with a thickness of 18 mm (S11-12)

3.2.2 List of Specimens

There are six types of specimens, and each type is produced twice. One specimen of each type is subjected to static testing, while the other is subjected to dynamic testing. A total of 12 test specimens were produced and documented. Detailed information about these specimens can be found in the list in the table 3.3. The 1-layer specimens were produced at 4 different prestressing levels ranging from 0 kN to 6 kN with 2 kN intervals.

Specimen Nr.	t [mm]	P [kN]	Textile layers	Prism Nr.	Concreted on	Testing	Tested on	f_{cm} [MPa]	f_{ctm} [MPa]
S1	12	2	1-layer	P6	15.11.2023	Static	14.02.2024	121.51	14.08
S2	12	2	1-layer	P6	15.11.2023	Dynamic	19.02.2024	121.51	14.08
S3	12	4	1-layer	P2	18.10.2023	Static	17.02.2024	137.08	14.81
S4	12	4	1-layer	P2	18.10.2023	Dynamic	19.02.2024	137.08	14.81
S5	12	6	1-layer	P5	22.11.2023	Static	14.02.2024	123.95	11.96
S6	12	6	1-layer	P5	22.11.2023	Dynamic	19.02.2024	123.95	11.96
S7	12	-	1-layer	P1	04.10.2023	Static	14.02.2024	127.91	13.16
S8	12	-	1-layer	P3	13.11.2023	Dynamic	19.02.2024	129.74	12.61
S9	12	-	2-layer	P4	15.11.2023	Static	14.02.2024	119.71	13.16
S10	12	-	2-layer	P4	15.11.2023	Dynamic	19.02.2024	119.71	13.16
S11	18	-	2-layer	P3	13.11.2023	Static	14.02.2024	129.74	12.61
S12	18	-	2-layer	P3	13.11.2023	Dynamic	19.02.2024	129.74	12.61

Tab. 3.3: List of Specimens

3.2.3 Stability Analysis

There is no stability problem with immediate bond prestressing. This is because the prestressing element will return the prestressed element to its original shape in the event of deformation.

3.2.4 Formwork

Several formworks were constructed using precision-cut wooden planks, see Fig. 3.3.

Fig. 3.3: Formwork

3.2.5 Concreting

The concreting method used was the laminar method. This method involves the sequential concreting of the bottom layer, followed by the positioning of the textile-reinforcement in its designated place. If deemed necessary, pretensioning of the fabric is performed prior to the subsequent concreting of the top layer. For each batch prisms with the dimensions 40x40x160 mm^3 were cast and stored under the same conditions as the specimens. Accompanying the testing of the specimens also matrix properties including compressive strength and flexural strength were determined.

3.2.6 Prestressing Setup

The prestressing bed is constructed of rolled steel with equal leg angles, reinforced with multiple stiffeners for added strength. Detailed design specifications can be found in Fig. 3.4. The steel structure has been designed using linear Finite Element Method (FEM) analysis. The design

ensures minimal deformation (see Fig. 3.6b) and consistently meets the critical von Mises yield criterion, as shown in Fig. 3.6c. The entire design is based on a analysis of the maximum prestressing force required to produce the specimens, as shown in Fig. 3.6a. See the appendix for the steel shop drawings and FEM analysis.

The most challenging aspect of configuring the prestressing setup involved devising a solution to apply the required prestressing force through clamping elements onto the textile. After exploring various alternatives, the decision was made to employ rough steel for the clamping elements (See Fig. 3.5f), concurrently pre-tensioning the screws within these elements to achieve the desired friction between textile and clamping elements.

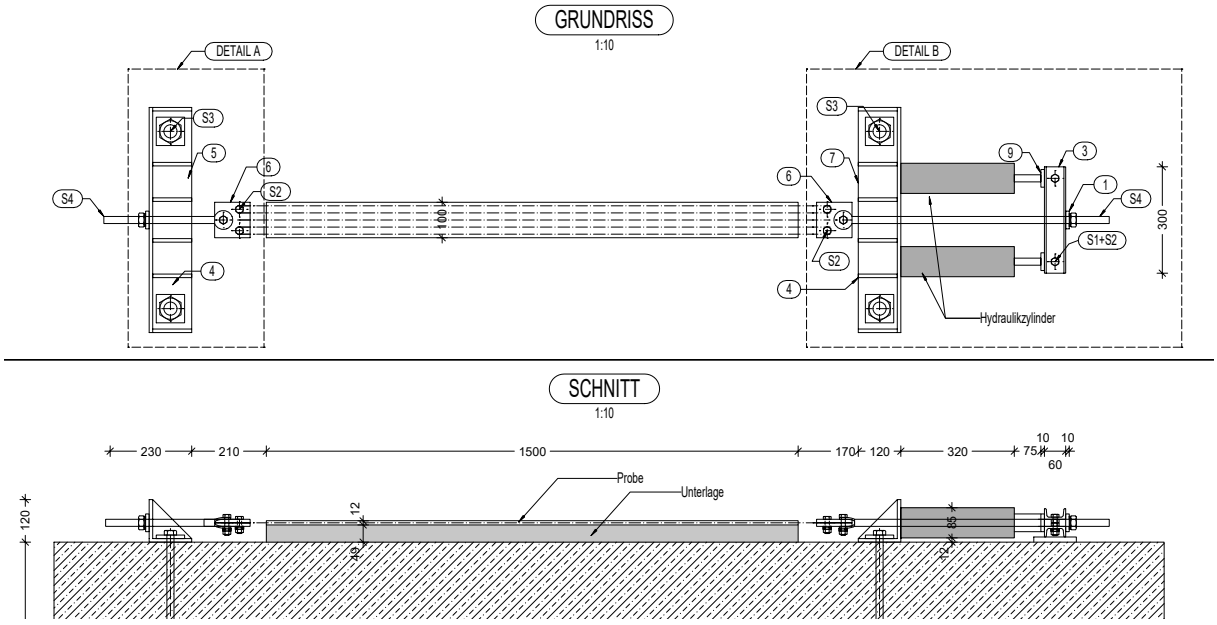

Fig. 3.4: Prestressing bed blueprint

The prestressing setup consists of 5 main components:

- Prestressing bed, See Fig. 3.5a
- Hydraulic cylinders, See Fig. 3.5b
- Hydraulic jack hand pump, See Fig. 3.5c
- Compression force transducer, See Fig. 3.5d
- Clamping element, See Fig. 3.5e and 3.5f

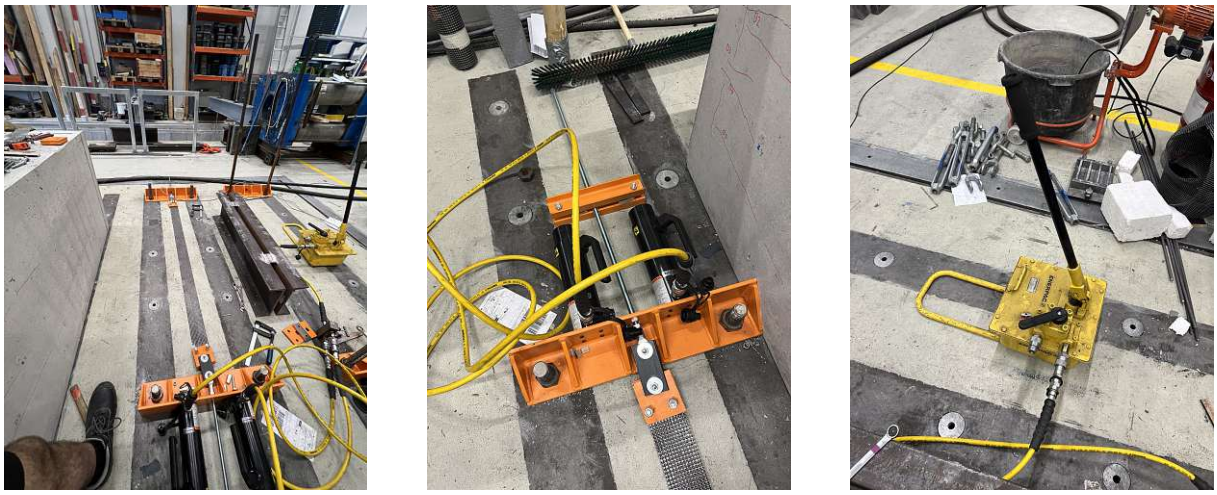

(a) (b) (c)

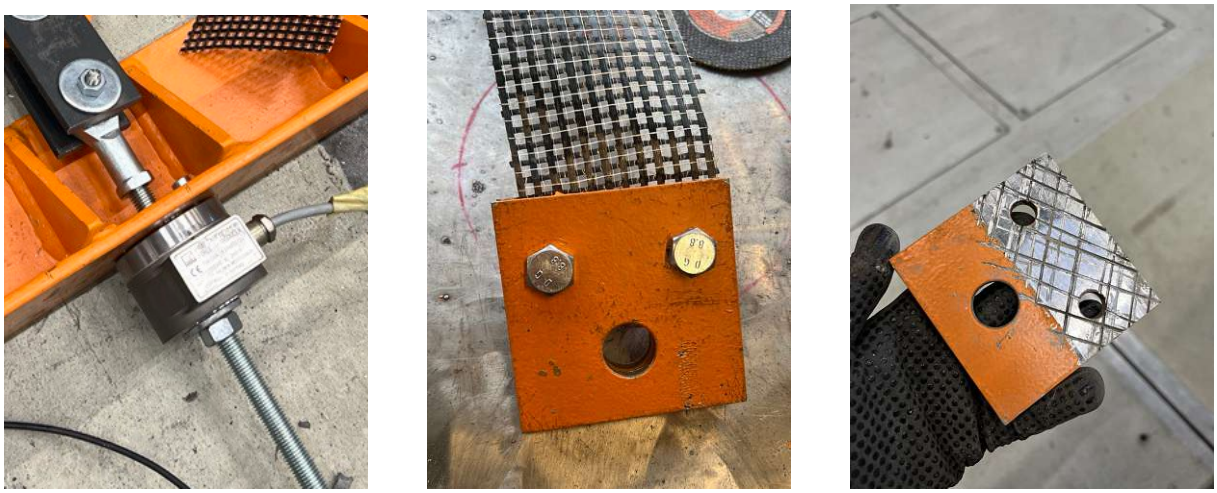

(d) (e) (f)

Fig. 3.5: Prestressing setup

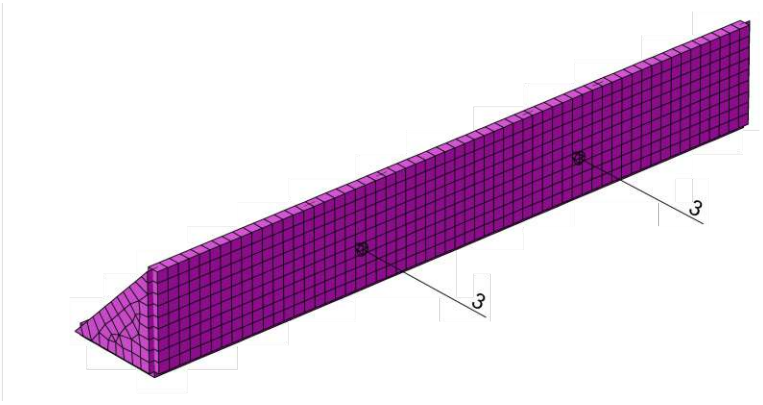

(a) Applied forces from prestressing

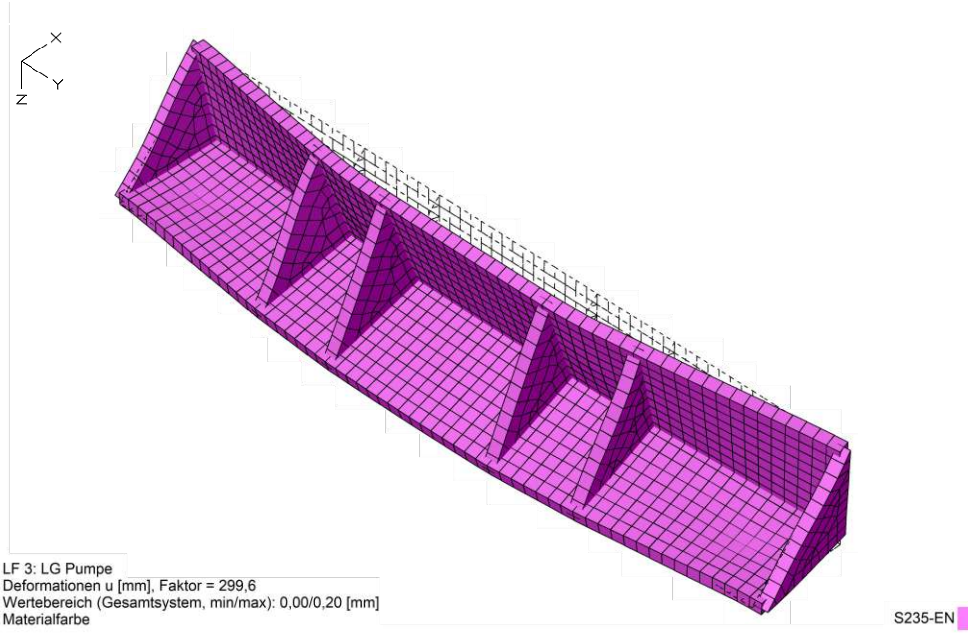

(b) Deformations

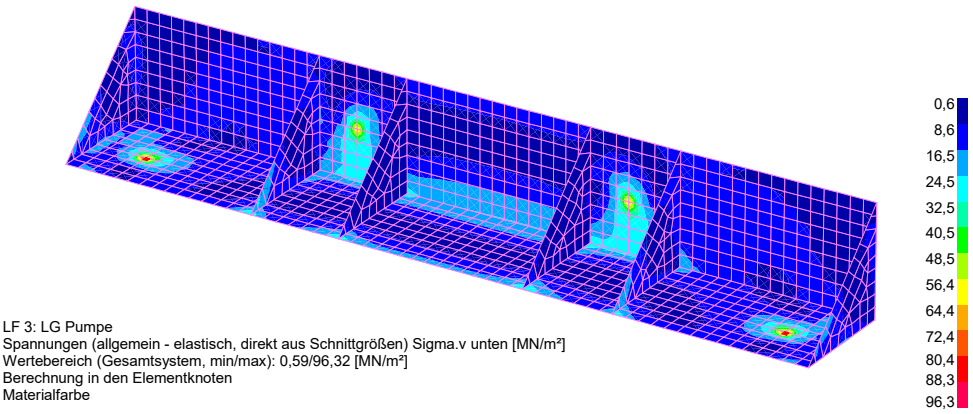

(c) von Mises yield criterion

Fig. 3.6: Prestressing bed - FEM analysis overview

3.2.7 Prestressing Force in Textiles over Time

Fig. 3.7 shows the evolution of prestressing forces in textiles over time. The increase in prestressing force after 12 hours may be attributed to the shrinkage of the mortar.

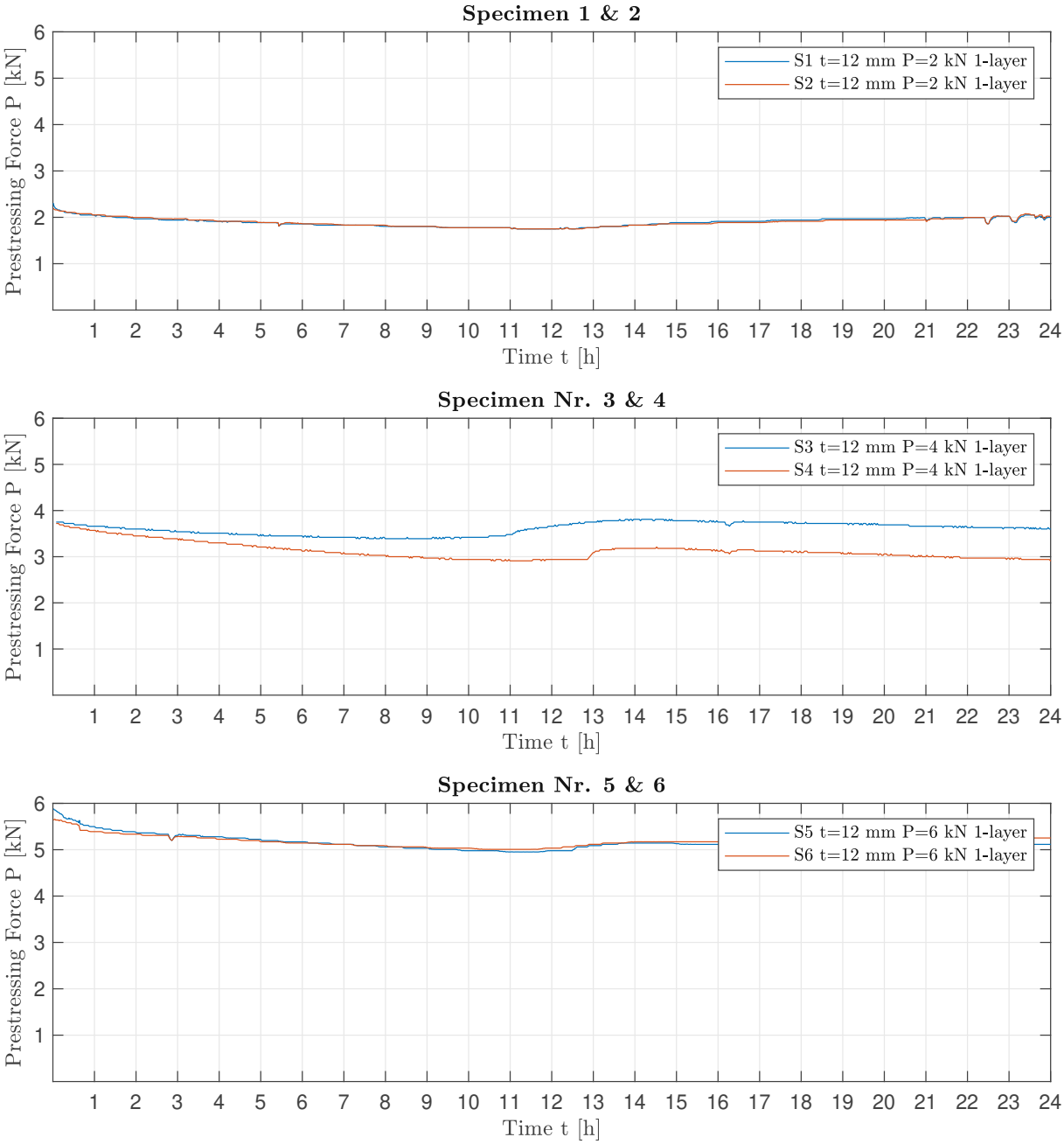

Fig. 3.7: Prestressing force in textiles over time

3.3 Tensile Test

Tensile tests were performed to determine the composite behavior of the TRC elements. In the experimental setup, the specimen was securely attached to the tensile testing machine using two hydraulic cylinders for clamping, one at the top and one at the bottom. This arrangement allowed a displacement-controlled tensile test to be performed at a constant speed of 10 mm/min. Accurate measurement of the specimen displacement was achieved by implementing four highly sensitive displacement transducers to ensure accurate data acquisition. At the same time, the force applied to the specimen during the test was recorded by a force transducer. In addition to these measurements, a camera system was integrated into the experimental setup to capture high-resolution images at regular 5-second intervals. This sampling allowed a detailed study of the specimen deformation during the test. The recorded data were later processed in MATLAB. The stress-strain diagram obtained from the test is shown in section 4.1.

(a) **(b)**

Fig. 3.8: Tensile test setup

3.4 Free Vibration Test

Free vibration tests were performed to experimentally investigate the damping behavior of TRC components. The test specimens were clamped in the middle, thus creating two cantilever beams with a length of 67.5 cm from a mechanical point of view. Each of these beams was mathematically modeled as a SDOF system. Steel components were used to clamp the specimens. The specimens were placed on the head plate of an I-beam and clamped between this plate and another steel plate over a length of 15 cm. An elastomeric bearing was placed between the steel plate and the surface of the specimen. The use of the elastomeric bearing was essential, otherwise, due to the uneven surface of the TRC elements, the elements would break after tightening the rods, making it impossible to impose a cantilever beam. The elastomeric bearing would affect the damping ratio, which was not considered in this research. Threaded rods were screwed into holes in the steel base plate to secure not only the specimens but also the entire test setup, see Fig. 3.9.

To measure acceleration and displacement, an accelerometer and a laser sensor were installed 30 cm from the end of the cantilever, see Fig. 3.10. Since the weight of the sensor was small compared to the weight of the specimen, it can be assumed that the vibration behavior was not affected by the additional weight. In addition, the vibrations were recorded without contact using a laser displacement sensor to compare the measurements. The distance from the laser sensor to the underside of the specimen was recorded during free vibration. At the same time, the double recording of the vibrations provided a safety measure in case of a possible failure of one of the two measuring devices.

Due to the geometry of the specimens, the vibrations required for dynamic testing were most easily achieved by initiating an initial displacement. For this purpose, the specimens were statically displaced at the beginning of the measurements and then released. An excitation weight with a mass of 0.6 kg was suspended from the end of the cantilever by a string for specimens S2-10 and an excitation weight with a mass of 1.3 kg for specimen S12. By cutting the string, the specimens were released from the displaced position and vibrations were generated. To analyze the specimen for different levels of cracking, after each test, the cantilever end of the specimen was moved 1 cm toward the ground to increase the level of internal cracking. After reaching a deflection of 10 cm (measured from the initial position), the increments were increased to 5 cm and continued until the specimen broke.

As shown in section 2.2.4, each MDOF system vibrates in one of its mode shapes, similar to an SDOF system. The first five mode shapes of the 12 mm thick specimen are calculated using linear elastic FEM and are shown in Figure 3.11. The aim is to induce vibrations in the first mode shape of the system, which is close to its elastic bending line under vertical displacement at its end. Therefore, the sample was modeled as a SDOF system in the analysis of the experiments. After the vibration was induced, the acceleration and displacement were recorded and later analyzed in MATLAB. The damping ratio (ξ) plots obtained from the tests are shown in the section 4.1.

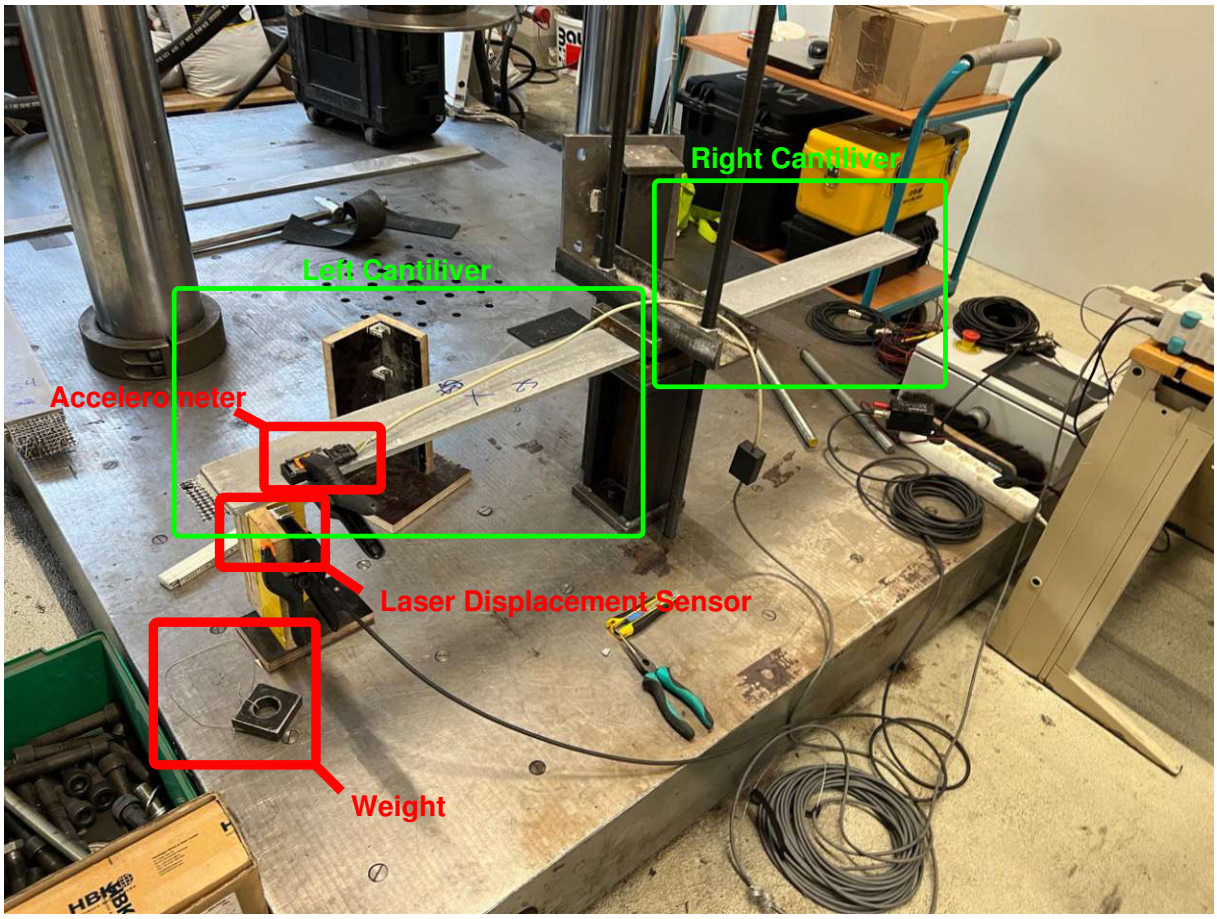

Fig. 3.9: Schematic of experimental setup

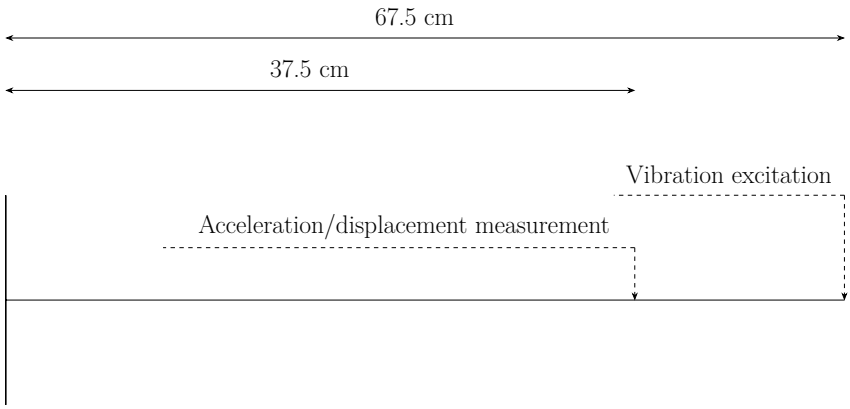

Fig. 3.10: Measurement principle and dimensions

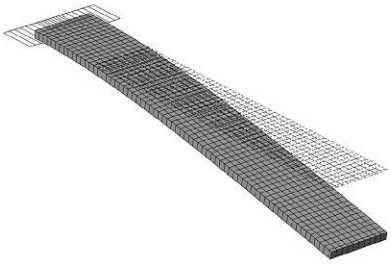

(a) 1. Mode shape
$F_{N,1} = 11.37$ Hz
$\omega_{N,1} = 71.40$ rad/s

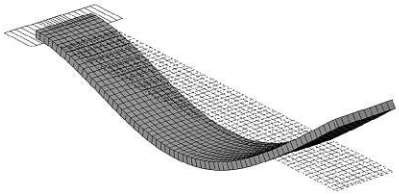

(b) 2. Mode shape
$F_{N,2} = 71.18$ Hz
$\omega_{N,2} = 447.26$ rad/s

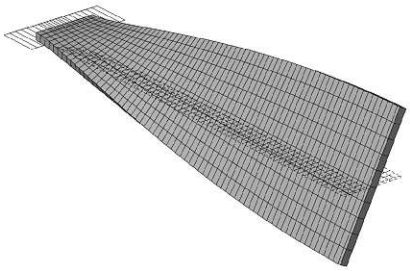

(c) 3. Mode shape
$F_{N,3} = 150.47$ Hz
$\omega_{N,3} = 945.45$ rad/s

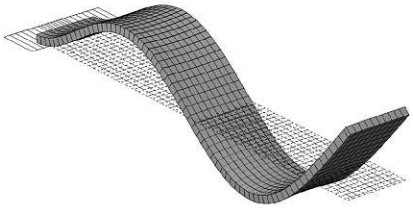

(d) 4. Mode shape
$F_{N,4} = 199.66$ Hz
$\omega_{N,4} = 1254.47$ rad/s

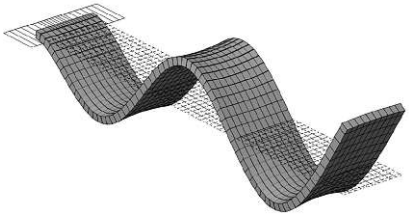

(e) 5. Mode shape
$F_{N,5} = 392.32$ Hz
$\omega_{N,5} = 2465.04$ rad/s

Fig. 3.11: Mode shapes and natural frequencies of specimen

Chapter 4

Experimental Test Results and Discussion

4.1 Tensile Loading Test

The stress-strain diagrams obtained from the tensile test are shown in Figure 4.2. It should be noted that specimen 7 slipped in the first test, so a second test was performed; therefore, two diagrams are shown for specimen 7, labeled S7.1 and S7.2. As expected, the three stages I, II, and III are visible in all plots, as shown in Fig. 2.6b. The fracture surfaces are shown in Figure 4.1. The following observations can be made from the results obtained:

Prestressing Comparing the results, it is obvious that prestressing prolongs stage I, which is reasonable because the compressive stresses from prestressing delay the cracking of the concrete.

Reinforcement Ratio An obvious increase in tensile strength was expected, but as the results show, doubling the reinforcement ratio (ρ) resulted in a slight decrease in tensile strength in S9 and an increase of only about 30% in S11, as shown in Fig. 4.2. The reason for this unexpected result can be the following.

The simplistic assumption that doubling the reinforcement doubles the tensile strength is derived from the behavior of steel-reinforced concrete. Steel has a high ductility, which allows it to develop plastic strains when the yield strength is reached in one rebar, allowing other rebars to also reach their maximum capacity. Carbon, on the other hand, has a much lower ultimate strain than steel and does not exhibit plastic behavior. This means that when the maximum load is reached at a weak point in one layer of fabric, it may not undergo plastic deformation until the second layer is able to contribute. As a result, the weak layer fails and the entire tensile force must be carried by the second layer, resulting in no noticeable difference between 1-layer and 2-layer reinforced TRC.

(a) S1 **(b)** S3 **(c)** S5

(d) S7 **(e)** S9 **(f)** S11

Fig. 4.1: Fracture surfaces

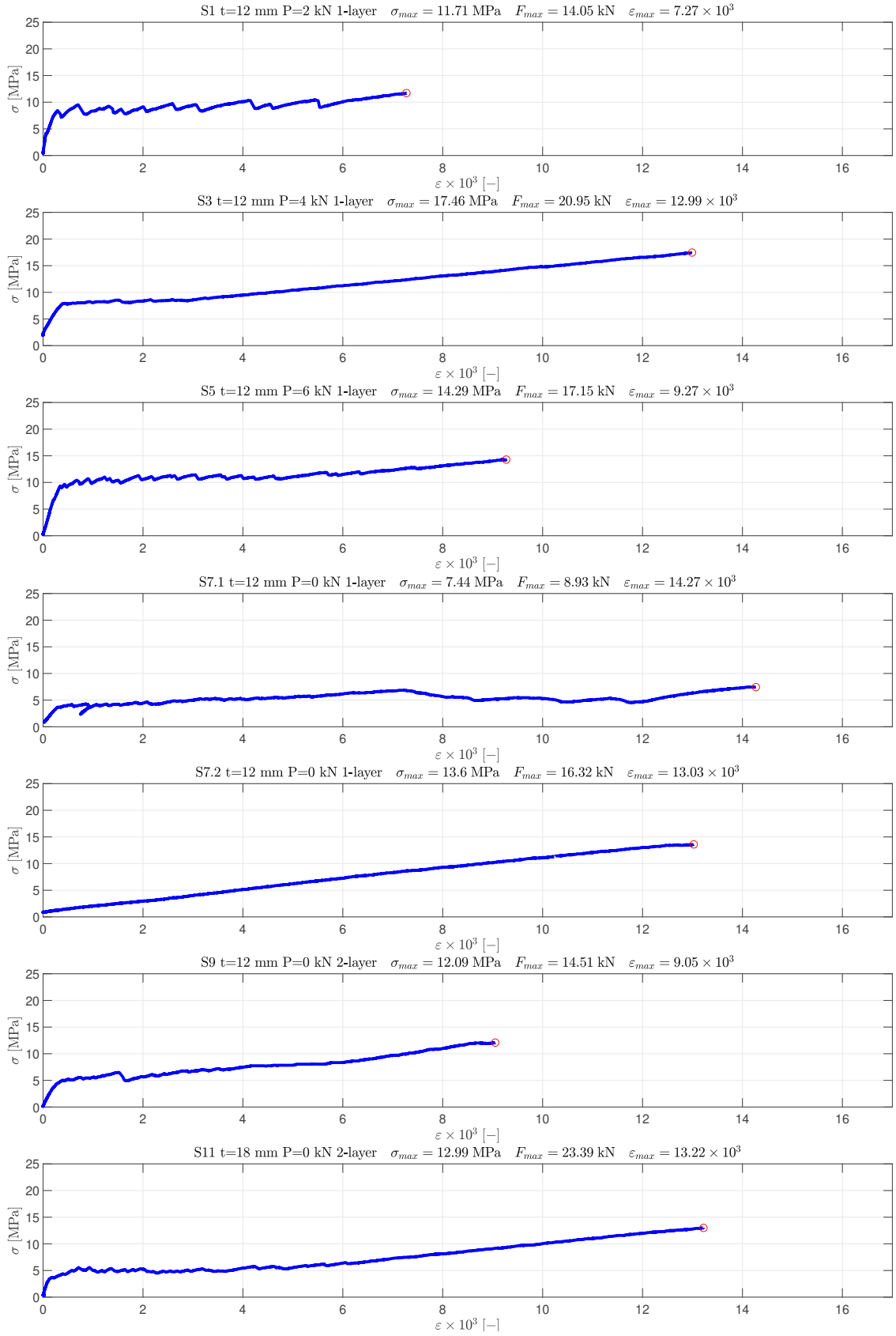

Fig. 4.2: Stress-strain diagram from tensile test

4.2 Free Vibration Test

The acceleration-time records of the free vibration tests are presented in Appendix C. In this section, these records are analyzed.

4.2.1 Damping Ratio (ξ)

In the acceleration-time records from the accelerometer, first and fifth peaks were used to calculate the damping ratio according to Eq. 2.14 using the MATLAB code in Appendix A. The damping ratios measured in the free vibration test are shown in Fig. 4.3. For clarity, the average results and the quadratic regression are also shown. The following observations can be made from the results obtained:

Prestressing indirectly affects the damping ratio as it decreases the tension stresses in concrete and therefore prevents cracking. The specimens with a single layer of textile reinforcement, as shown in Fig. 4.3, are arranged in the diagram according to their respective prestressing forces. In particular, the specimen with the lowest prestressing force occupies the top position, while the specimen with the highest prestressing force is at the bottom. The intermediate specimens maintain the same order between these two extremes.

Cracking Level directly affects the damping ratio because it increases the internal friction surfaces. The damping ratio shows an increasing trend with increasing crack levels. However, beyond a certain crack threshold, the damping ratio begins to decrease. This phenomenon diminishes as the prestressing force increases, which is consistent with the expectation that prestressing will mitigate internal cracking.

Reinforcement Ratio indirectly affects the damping ratio because cracking is limited at higher reinforcement ratios. It becomes evident that the damping ratio of the specimen with two layers of textile reinforcement is lower than that of the specimens with a single layer of textile reinforcement and no prestressing. This trend is further confirmed when examining the results of the specimens with two layers of reinforcement and a thicker section. It can be concluded that as the reinforcement ratio increases, the damping ratio decreases.

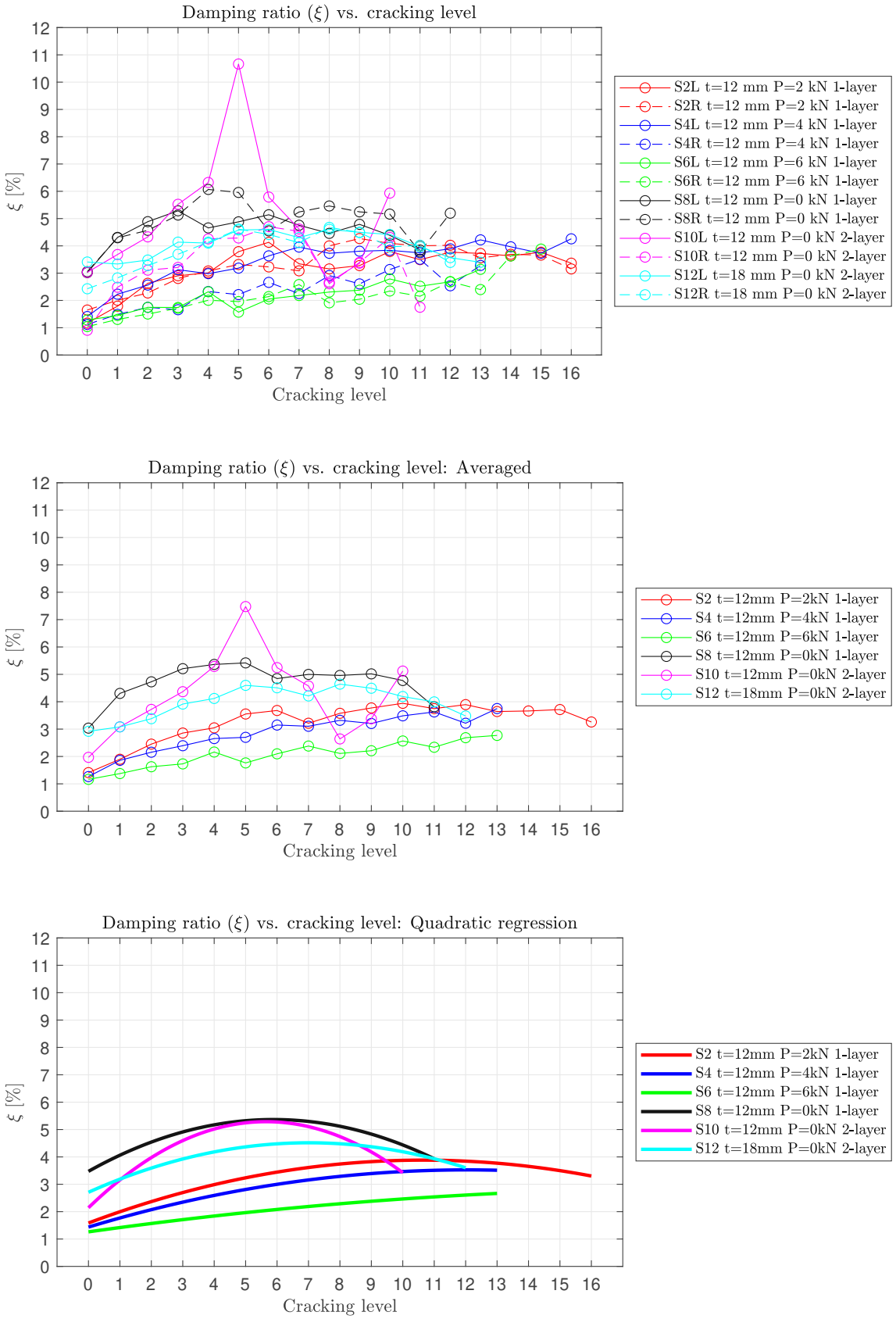

Fig. 4.3: Damping ratio (ξ) versus cracking level

4.2.2 Damped Natural Frequency (F_D)

In the acceleration-time records from the accelerometer, first and fifth peaks were used to calculate the damped natural frequency using the MATLAB code in Appendix A. The damped natural frequency measured in the free vibration test is shown in Fig. 4.4. For clarity, the average results and the quadratic regression are also shown. The following observations can be made from the results obtained:

Prestressing As shown in Fig. 4.4, the specimen S8 with a thickness of 12 mm and no prestressing has a damped natural frequency $F_D \approx 13$ Hz in stage I, which is quite close to the prediction of the FEM analysis shown in Fig. 3.11 with $F_{N,1} = 11.37$ Hz for the 1st mode shape. As the prestressing force increases in S2, S4, and S6, the damped natural frequency also increases, indicating an increase in the stiffness of the structure.

Cracking Level Looking at the overall trend in Fig. 4.4, it can be seen that as the cracking level increases, the damped natural frequency decreases. This means that, as expected, the higher the crack level, the lower the stiffness of the system. This trend continues until a certain threshold is reached, after which the damped natural frequency increases slightly.

Reinforcement Ratio Comparing the results of S10 with S8, it is clear that as the reinforcement ratio increases, the damped natural frequency also increases. This indicates that the reinforcement ratio has a significant effect on the stiffness of the structure.

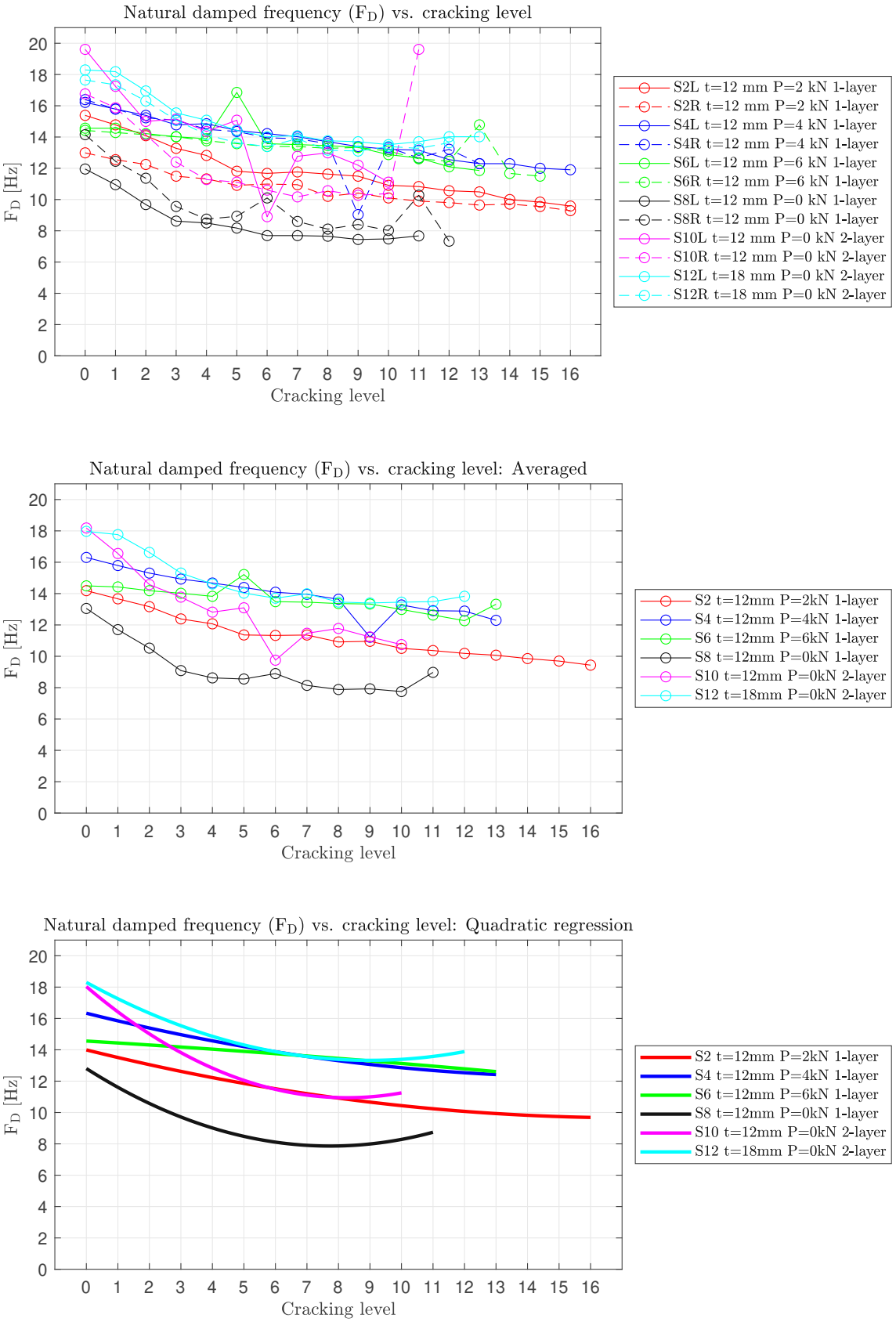

Fig. 4.4: Damped natural frequency (F_D) versus cracking level

Chapter 5

Conclusions

The primary objective of this study was to analyze the dynamic behavior of prestressed textile-reinforced concrete, with particular emphasis on the study of damping behavior. The damping ratio (ξ) was chosen as the parameter for measuring damping, a rational choice considering the light damping and the range of existing studies related to this parameter, which enhances the meaningfulness of comparisons. In addition, the viscoelastic behavior model of materials is widely accepted and applied in practice.

The first challenge in this research was to introduce the prestressing force into textiles. To achieve this, a prestressing bed was meticulously designed using FEM, and steel parts were ordered according to the shop drawings. Overcoming the hurdle of applying force to the textile structure without tearing or slipping was particularly challenging. There is potential for further research in this area to develop innovative clamping methods.

Twelve specimens with different prestressing levels, cross-sections, and reinforcement ratios were then built to allow a comprehensive study of the effects of each parameter. The results indicate that prestressing significantly affects the damping ratio, with an increase in prestressing correlating with a decrease in damping ratio. This phenomenon can be attributed to the preventive effect of prestressing on concrete cracking by reducing tensile stresses, as evidenced by the extension of stage I in the stress-strain diagram observed in tensile tests. In addition, it was observed that higher reinforcement ratios (ρ) lowers the damping ratio (ξ). In particular, a higher degree of cracking corresponds to a higher damping ratio, indicating increased internal energy dissipation between cracks. On the other hand, a decrease in damping ratio was observed beyond a certain level of cracking, and this decrease was also dependent on the level of prestressing.

Bibliography

[1] M. Y. Çilesiz. "Damping behavior of textile-reinforced concrete". Master's thesis. TU Wien, 2023.

[2] T. Gries, M. Raina, T. Quadflieg, and O. Stolyarov. *1 - Manufacturing of textiles for civil engineering applications*. Ed. by T. Triantafillou. Woodhead Publishing, 2016, pp. 3–24. ISBN: 978-1-78242-446-8. DOI: https://doi.org/10.1016/B978-1-78242-446-8.00002-1. URL: https://www.sciencedirect.com/science/article/pii/B9781782424468000021.

[3] R. Silva and F. Silva. "Carbon textile reinforced concrete: materials and structural analysis". In: *Materials and Structures* 53 (Feb. 2020).

[4] C. Wu, Y. Pan, and L. Yan. "Mechanical Properties and Durability of Textile Reinforced Concrete (TRC);A Review". In: *Polymers* 15.18 (2023). ISSN: 2073-4360. URL: https://www.mdpi.com/2073-4360/15/18/3826.

[5] N. Gattesco and I. Boem. "Characterization tests of GFRM coating as a strengthening technique for masonry buildings". In: *Composite Structures* 165 (2017), pp. 209–222. ISSN: 0263-8223. URL: https://www.sciencedirect.com/science/article/pii/S0263822316326666.

[6] G. Tyagi. "Yarn structure and properties from different spinning techniques". In: *Advances in Yarn Spinning Technology* (Sept. 2010), pp. 119–154. DOI: 10.1533/9780857090218.1.119.

[7] B. Wulfhorst. "Textile structures as reinforcements for concrete". In: *Concrete. Precast. Plant Technol* 64 (1998), pp. 133–138.

[8] D. Spencer, ed. *Knitting Technology. A Comprehensive Handbook and Practical Guide*. Woodhead Publishing, 2001.

[9] M. Lieboldt. "Feinbetonmatrix für Textilbeton". In: *Beton- und Stahlbetonbau* 110.S1 (2015), pp. 22–28. eprint: https://onlinelibrary.wiley.com/doi/pdf/10.1002/best.201400100. URL: https://onlinelibrary.wiley.com/doi/abs/10.1002/best.201400100.

[10] *Beton – Festlegung, Eigenschaften, Herstellung und Konformität*. DIN EN 206 - 2021-06. Beuth, July 2014.

[11] M. El Kadi, S. Verbruggen, J. Vervloet, M. De Munck, J. Wastiels, D. Van Hemelrijck, and T. Tysmans. "Experimental Investigation and Benchmarking of 3D Textile Reinforced Cementitious Composites". In: *Strain-Hardening Cement-Based Composites*. Ed. by V. Mechtcherine, V. Slowik, and P. Kabele. Dordrecht: Springer Netherlands, 2018, pp. 400–408. ISBN: 978-94-024-1194-2.

[12] J. Vervloet, T. Tysmans, M. El Kadi, M. De Munck, P. Kapsalis, P. Van Itterbeeck, J. Wastiels, and D. Van Hemelrijck. "Validation of a Numerical Bending Model for Sandwich Beams with Textile-Reinforced Cement Faces by Means of Digital Image Correlation". In: *Applied Sciences* 9.6 (2019). ISSN: 2076-3417. URL: https://www.mdpi.com/2076-3417/9/6/1253.

[13] W. BRAMESHUBER, M. Hinzen, A. Dubey, A. Peled, B. Mobasher, A. Bentur, C. Aldea, F. Silva, J. Hegger, T. Gries, J. Wastiels, K. Malaga, C. Papanicolaou, L. Taerwe, M. Curbach, V. Mechtcherine, A. Naaman, J. Orlowsky, H. Patrice, and F. Jesse. "Recommendation of RILEM TC 232-TDT: Test methods and design of textile reinforced concrete". In: *Materials and Structures* 10.1617/s11527-016-0839-z (May 2016).

[14] S. Sueki, C. Soranakom, and B. Mobasher. "Pullout-Slip Response of Fabrics Embedded in a Cement Paste Matrix". In: *Journal of Materials in Civil Engineering - J MATER CIVIL ENG* 19 (Sept. 2007). DOI: 10.1061/(ASCE)0899-1561(2007)19:9(718).

[15] C. Petersen and H. Werkle. *Dynamik der Baukonstruktionen*. Springer Fachmedien Wiesbaden, 2018. ISBN: 9783834821096. URL: https://books.google.at/books?id=AktjDwAAQBAJ.

[16] A. Chopra. *Dynamics of Structures*. Prentice-Hall international series in civil engineering and engineering mechanics. Pearson Education, 2007. ISBN: 9788131713297. URL: https://books.google.at/books?id=0dU1bDaRyP4C.

[17] R. Dieterle. *Modelle fur das Dampfungsverhalten von schwingenden Stahlbetontragern ,im ungerissenen und gerissenen Zustand*. Springer, 1981.

[18] K. Teichen. *Über die innere Dämpfung von Beton*. Otto-Graf-Institut Stuttgart: Schriftenreihe. na, 1968. URL: https://books.google.at/books?id=StpLHAAACAAJ.

[19] I. Ali and C. E. Kesler. "Rheology of concrete: a review of research". In: *University of Illinois Engineering Experiment Station bulletin; no. 476* (1965).

[20] J. Penzien. "Damping characteristics of prestressed concrete". In: *Journal Proceedings*. Vol. 61. 9. 1964, pp. 1125–1148.

[21] G. de Miranda Saleme Gidrão. "Characterization of concrete internal damping". In: *3o Encontro Luso-Brasileiro de Degradação em Estrutur* (2018).

[22] SIKA. *PRODUCT DATA SHEET SikaGrout®-3350*. https://industry.sika.com/dam/dms/ca01/z/sikagrout-3350.pdf. 2022. (Visited on 07/03/2024).

[23] SIKA. *PRODUCT DATA SHEET Sika® CarboDur®-300 Grid*. https://hkg.sika.com/dms/getdocument.get/0aa4367e-c5bd-4473-b05d-7c2804db051e/sika-carbodur-300grid.pdf. 2021. (Visited on 07/03/2024).

Appendix A

Matlab Codes

Listings

Program Code A.1: Free vibration test

```
%% Damped Oscillation Test for Multiple Specimens
clear
clc
close all

%% General Parameters
j = 5; %Number of Peaks used to calculate zeta
time_tolerance = 0.01;
Threshold_a = 0.05;
Threshold_u = 0.01;
color =          [[1 0 0 1], [0 1 0 1], [0 0 1 1], [1 0 1 1], [1 1 1 1], [0
    1 1 1]];
color_trans =    [[1 0 0 0.3], [0 1 0 0.3], [0 0 1 0.3], [1 0 1 0.3], [1 1 1
     0.3], [0 1 1 0.3]];

%% File names and starting point of Tests
file_name = ["S2L", "S2R", "S4L", "S4R", "S6L", "S6R", "S8L", "S8R", "S10L
    ", "S10R", "S12L", "S12R"];
Specimen_Name = ["S2L t=12 mm P=2 kN 1-layer", "S2R t=12 mm P=2 kN 1-layer
    ", "S4L t=12 mm P=4 kN 1-layer", "S4R t=12 mm P=4 kN 1-layer", "S6L t
    =12 mm P=6 kN 1-layer", "S6R t=12 mm P=6 kN 1-layer", "S8L t=12 mm P=0
    kN 1-layer", "S8R t=12 mm P=0 kN 1-layer", "S10L t=12 mm P=0 kN 2-layer
    ", "S10R t=12 mm P=0 kN 2-layer", "S12L t=18 mm P=0 kN 2-layer", "S12R
    t=18 mm P=0 kN 2-layer"];
Specimen_Name_ave=["S2  t=12mm P=2kN 1-layer ", "S4  t=12mm P=4kN 1-layer",
     "S6 t=12mm P=6kN 1-layer ", "S8  t=12mm P=0kN 1-layer ", "S10 t=12mm P
    =0kN 2-layer ", "S12 t=18mm P=0kN 2-layer "];

Start = zeros(12,20);
%S2L
Start(1, 1:17) = [35.1767, 123.118, 188.13, 310.393, 374.58, 491.67,
    534.048, 580.323, 627.12, 748.077, 915.73, 1021.46, 1220.08, 1338.09,
    1543.14, 1587.07, 1658.23];
%S2R
Start(2, 1:17) = [81.03, 133.582, 172.832, 215.002, 249.28, 297.573,
    335.212, 392.743, 506.51, 556.935, 605.605, 656.577, 714.755, 764.023,
    869.098, 913.762, 1001.64];
%S4L
Start(3, 1:17) = [19.10, 75.1917, 102.077, 133.702, 185.447, 241.848,
    270.742, 305.572, 373.858, 404.362, 428.31, 483.972, 504.705, 540.482,
    604.667, 641.577, 685.87];
%S4R
Start(4, 1:14) = [24.395, 88.7233, 130.453, 165.663, 221.808, 257.885,
    282.402, 312.363, 351.923, 375.327, 395.538, 429.078, 489.73, 533.432];
%S6L
Start(5, 1:14) = [149.45, 180.882, 206.057, 240.792, 300.15, 339.647,
    368.395, 410.23, 439.148, 467.657, 526.175, 579.662, 619.592, 653.375];
%S6R
Start(6, 1:16) = [11.4483, 71.7233, 112.555, 158.202, 213.815, 246.03,
    274.25, 345.292, 387.565, 415.948, 445.927, 529.367, 593.732, 656.008,
    694.355, 737.068];
%S8L
Start(7, 1:12) = [79.0433, 110.855, 174.808, 195.737, 220.930, 249.61,
    281.135, 320.927, 363.178, 416.548, 455.802, 522.095];
%S8R
Start(8, 1:13) = [81.345, 111.647, 139.093, 172.34, 215.807, 258.277,
    310.267, 353.812, 380.808, 407.147, 446.33, 483.14, 517.052];
%S10L
```

```
Start(9, 1:11) = [7.04667, 37.8483, 69.015, 101.318, 168.913, 190.5,
    237.36, 247.08, 274.128, 304.503, 317.97];
%S10R
Start(10, 1:12) = [197.373, 247.205, 277.272, 310.68, 350.315, 395.343,
    426.87, 498.415, 553.415, 553.25, 598.025, 637.987];
%S12L
Start(11, 1:14) = [9.7, 31.9133, 54.9067, 93.9283, 119.483, 147.77,
    168.337, 185.72, 216.375, 238.385, 259.82, 288.99, 344.323, 390.528];
%S12R
Start(12, 1:13) = [44.98, 67.01, 97.26, 124.942, 164.147, 204.081, 223.07,
    259.65, 279.897, 317.66, 344.088, 368.373, 398.827];


%% First loop
for f = 1:12

    Number_Levels(f) = nnz(Start(f, :));
    remove_t_from = Start(f, 1:Number_Levels(f)) + 0;
    remove_t_till = Start(f, 1:Number_Levels(f)) + 4;
    file_path = "C:\Users\Shahriyar Azadi\OneDrive\BI\TU Wien\-
        Diplomarbeit\Versuchsdaten\Ausschwing\" + file_name(f) + ".txt";

    data_master = readmatrix(file_path, 'Delimiter', '\t', 'HeaderLines',
        3, 'DecimalSeparator', ',');
    time_master = data_master(:, 1);


    figure('Position', [1500, 200, 800, 1000]);
    sgtitle(Specimen_Name(f), 'Interpreter', 'latex');

    % Initialize an empty table to store results
    results_table = table('Size', [0, 6], 'VariableTypes', {'string', '
        double', 'double', 'double', 'double', 'double'}, ...
                          'VariableNames', {'Cracking level', 'T_D [s]', '
                              F_D [Hz]', 'zeta_1 [%]','zeta_20 [%]', '
                              omega_D [rad/s]'});



    %% Second loop
    for i = 1:Number_Levels(f)
        %% Load data for the current specimen

        data = data_master(find(abs(time_master-remove_t_from(i))<
            time_tolerance):find(abs(time_master-remove_t_till(i))<
            time_tolerance), :, :);
        time = data(:, 1);
        acceleration = data(:, 2)*9.81;

        %% Analysis of Acceleration Data

        [peaks, locations_peaks] = findpeaks(acceleration, '
            MinPeakProminence', Threshold_a);
        T_D = (time(locations_peaks(1+j)) - time(locations_peaks(1))) / j;
        F_D(f,i) = 1 / T_D;
        omega_D(f,i)=F_D(f,i)*2*pi;
        zeta(f,i)=log(peaks(1)/peaks(1+j)) / (2*pi*j);
        %delta_acceleration = (1 / (j+1)) * log(peaks(1) / peaks(j+1));
        %zeta(f,i) = delta_acceleration / ((4 * pi()^2 + delta_acceleration
            ^2)^(1/2));
```

```
84
85          omega_N(f,i)=omega_D(f,i)/sqrt(1-zeta(f,i)^2);
86          envelope_acceleration = acceleration(locations_peaks(1)) .* exp(-
                zeta(f,i) * omega_D(f,i) .* (time - time(locations_peaks(1))));
87
88          current_results_table = table({num2str(i)}, ...
89                                        round(T_D,2), ...
90                                        round(F_D(f,i),2), ...
91                                        round(zeta(f,i)*100,2), ...
92                                        round(zeta(f,i)*100,2), ...
93                                        round(omega_D(f,i),2), ...
94                                        'VariableNames', {'Cracking level', '
                                              T_D [s]', 'F_D [Hz]', 'zeta_1 [%]
                                              ','zeta_20 [%]', 'omega_D [rad/s]
                                              '});
95
96          results_table = [results_table; current_results_table];
97
98          %% Subplotting
99
100         subplot(round(Number_Levels(f)/2,0), 2, i)
101         plot(time, acceleration, 'b', 'LineWidth', 0.7)
102         hold on
103         plot(time(locations_peaks(1:j+1)), peaks(1:j+1), 'ro', 'MarkerSize'
                , 3,'LineWidth', 0.7)
104         plot(time, envelope_acceleration, 'k--', 'LineWidth', 1)
105         plot(time, -envelope_acceleration, 'k--', 'LineWidth', 1)
106         grid on
107         box on
108
109         title("\textbf{Cracking level }"+num2str(i-1)+"$\quad \xi = $"+
                num2str(round(zeta(f,i)*100,2))+ "$ \; \% \quad F_D = $" +
                num2str(round(F_D(f,i),2))+ "$ \; \mathrm{[Hz]}$", 'Interpreter
                ', 'latex')
110         xlabel("$\mathbf{t} \mathrm{[s]}$", 'Interpreter', 'latex')
111         ylabel("$\mathrm{\mathbf{\ddot{u}}\;[m/s^2]}$", 'Interpreter', '
                latex')
112
113         if i==1
114             h=legend('{Oscillation Curve}', "First "+num2str(j)+"{ Max
                    Amplitudes}", '{Envelope Curve}', 'Interpreter', 'latex', '
                    Location','eastoutside');
115             set(h,'Position',[0.70 0.93 0.2 0.05]);
116
117         end
118
119         hold off
120         xlim([remove_t_from(i), remove_t_till(i)]);
121
122     end
123
124     saveas(gcf,'Figures\Damping\'+strrep(file_name(f), ' ', '_'),'epsc')
125
126 %     disp('Final Results Table:');
127 %     disp(results_table);
128 %     writetable(results_table, 'Result_Tables\damping_ratios_table_'+
        strrep(Specimen_Name(f), ' ', '_')+'.csv');
129
130 end
131
```

```
%close all

%% Damping Ratio zeta
    figure('Position', [100, 100, 850, 1200]);

    % All
    subplot(3, 1, 1)
    grid on
    box on
    hold on
    color = ['r', 'b', 'g', 'k', 'm', 'c'];
    for i= 1:12
        if mod(i, 2) == 0
            p=plot(0:1:nnz(zeta(i, :))-1, zeta(i, 1:nnz(zeta(i, :)))*100, '
                --o');
        else
            p=plot(0:1:nnz(zeta(i, :))-1, zeta(i, 1:nnz(zeta(i, :)))*100, '
                -o');
        end
        set(p, 'Color', color(round(i/2)));

    end
    legend(Specimen_Name, 'Interpreter', 'latex', 'Location','eastoutside')
    title("Damping ratio $(\xi)$ vs. cracking level", 'Interpreter', 'latex
        ')
    xlabel("Cracking level", 'Interpreter', 'latex')
    ylabel("$\mathbf{\xi}\;[\%]$", 'Interpreter', 'latex')
    xticks(0:1:16);
    yticks(0:1:12);
    xlim([-1 17])
    ylim([0 12])

    % Mean
    subplot(3, 1, 2)
    grid on
    box on
    hold on

    for i = 1:2:12
        zeta_len = min(nnz(zeta(i, :)), nnz(zeta(i+1, :)));
        zeta_average=(zeta(i, 1:zeta_len)+zeta(i+1, 1:zeta_len))/2;
        q= plot(0:1:zeta_len-1, zeta_average(1:zeta_len)*100, '-o');
        set(q, 'Color', color(round(i/2)));
    end

    legend(Specimen_Name_ave, 'Interpreter', 'latex', 'Location','
        eastoutside')
    title("Damping ratio $(\xi)$ vs. cracking level: Averaged", '
        Interpreter', 'latex')
    xlabel("Cracking level", 'Interpreter', 'latex')
    ylabel("$\xi\;[\%]$", 'Interpreter', 'latex')
    xticks(0:1:16);
    yticks(0:1:12);
    xlim([-1 17])
    ylim([0 12])

    % Regression
    subplot(3, 1, 3)
    grid on
    box on
```

```
187     hold on
188
189     for i = 1:2:12
190         zeta_len = min(nnz(zeta(i, :)), nnz(zeta(i+1, :)));
191         zeta_average = (zeta(i, 1:zeta_len) + zeta(i+1, 1:zeta_len)) / 2;
192
193         % Plotting the original data
194         %q = plot(0:1:zeta_len-1, zeta_average(1:zeta_len) * 100, '-o');
195         set(q, 'Color', color(round(i/2)));
196
197         % Adding square regression line with the same color as the plot
198         x_values = 0:1:zeta_len-1;
199         y_values = zeta_average(1:zeta_len) * 100;
200         p = polyfit(x_values, y_values, 2);  % Fit a second-degree
                polynomial (square regression)
201         x_fit = 0:0.1:zeta_len-1;  % Generate x values for the fitted curve
202         y_fit = polyval(p, x_fit);  % Evaluate the polynomial at the x
                values
203
204         % Plotting the regression line with the same color as the plot
205         plot(x_fit, y_fit, '-', 'Color', color(round(i/2)), 'LineWidth', 2)
                ;
206     end
207
208     legend(Specimen_Name_ave, 'Interpreter', 'latex', 'Location','
            eastoutside')
209     title("Damping ratio $(\xi)$ vs. cracking level: Quadratic regression",
             'Interpreter', 'latex')
210     xlabel("Cracking level", 'Interpreter', 'latex')
211     ylabel("$\xi\;[\%]$", 'Interpreter', 'latex')
212     xticks(0:1:16);
213     yticks(0:1:12);
214     xlim([-1 17])
215     ylim([0 12])
216
217     saveas(gcf, 'Figures\Damping\xi', 'epsc')
218
219 % %% Damping Ratio Subfigure
220 %     figure('Position', [1000, 200, 850, 1000]);
221 %     grid on
222 %     box on
223 %     xticks(0:1:20);
224 %     yticks(0:1:10);
225 %     hold on
226 %
227 %     for i= 1:6
228 %         subplot(6, 1, i)
229 %         hold on
230 %         box on
231 %         grid on
232 %         p1=plot(0:1:nnz(zeta(2*i-1, :))-1, zeta(2*i-1, 1:nnz(zeta(2*i-1,
        :)))*100, '--o');
233 %         set(p1, 'Color', 'b');
234 %         p2=plot(0:1:nnz(zeta(2*i, :))-1, zeta(2*i, 1:nnz(zeta(2*i, :)))
        *100, '-o');
235 %         set(p2, 'Color', 'b');
236 %         hold off
237 %         legend(Specimen_Name(2*i), Specimen_Name(2*i-1), 'Location', '
        southeast', 'Interpreter', 'latex')
238 %         %title("Specimen "+num2str(i*2), 'Interpreter', 'latex')
```

```
239 %           xlabel("Cracking level", 'Interpreter', 'latex')
240 %           ylabel("$\mathbf{\xi}\;[\%]$", 'Interpreter', 'latex')
241 %           xticks(0:1:16);%max(nnz(zeta(2*i, :)),nnz(zeta(2*i-1, :)))-1);
242 %           yticks(0:2:20);
243 %           xlim([-1 17])
244 %           ylim([0 1+100*max(max(zeta(2*i-1, :)), max(zeta(2*i, :)))])
245 %       end
246 %       saveas(gcf,'Figures\Damping\xi_overview','epsc')
247 
248 % %% omega_D Diagram
249 %       figure('Position', [2300, 200, 600, 600]);
250 %       grid on
251 %       box on
252 %       %xticks(0:1:20);
253 %       %yticks(0:1:12);
254 %       hold on
255 %       color = ['r', 'b', 'g', 'k', 'm', 'c'];
256 %       for i= 1:12
257 %           if mod(i, 2) == 0
258 %               p=plot(0:1:nnz(omega_D(i, :))-1, omega_D(i, 1:nnz(omega_D(i,
    :))), '--o');
259 %           else
260 %               p=plot(0:1:nnz(omega_D(i, :))-1, omega_D(i, 1:nnz(omega_D(i,
    :))), '-o');
261 %           end
262 %           set(p, 'Color', color(round(i/2)));
263 %
264 %       end
265 %       legend(Specimen_Name, 'Interpreter', 'latex')
266 %       title("", 'Interpreter', 'latex')
267 %       xlabel("Cracking level", 'Interpreter', 'latex')
268 %       ylabel("$\omega_D\;\mathrm{[rad/s]}$", 'Interpreter', 'latex')
269 %       saveas(gcf,'Figures\Damping\omega_D_all','epsc')
270 %
271 % %% omega_N Diagram
272 %       figure('Position', [2300, 200, 600, 600]);
273 %       grid on
274 %       box on
275 %       %xticks(0:1:20);
276 %       %yticks(0:1:12);
277 %       hold on
278 %       color = ['r', 'b', 'g', 'k', 'm', 'c'];
279 %       for i= 1:12
280 %           if mod(i, 2) == 0
281 %               p=plot(0:1:nnz(omega_N(i, :))-1, omega_N(i, 1:nnz(omega_N(i,
    :))), '--o');
282 %           else
283 %               p=plot(0:1:nnz(omega_N(i, :))-1, omega_N(i, 1:nnz(omega_N(i,
    :))), '-o');
284 %           end
285 %           set(p, 'Color', color(round(i/2)));
286 %
287 %       end
288 %       legend(Specimen_Name, 'Interpreter', 'latex')
289 %       title("", 'Interpreter', 'latex')
290 %       xlabel("Cracking level", 'Interpreter', 'latex')
291 %       ylabel("$\omega_N\;\mathrm{[rad/s]}$", 'Interpreter', 'latex')
292 %       saveas(gcf,'Figures\Damping\omega_N_all','epsc')
293 
294 %% Natural damped frequency F_D
```

```
295     % All
296     figure('Position', [500, 100, 850, 1200]);
297     subplot(3, 1, 1)
298     grid on
299     box on
300     hold on
301     color = ['r', 'b', 'g', 'k', 'm', 'c'];
302     for i= 1:12
303         if mod(i, 2) == 0
304             p=plot(0:1:nnz(F_D(i, :))-1, F_D(i, 1:nnz(F_D(i, :))), '--o');
305         else
306             p=plot(0:1:nnz(F_D(i, :))-1, F_D(i, 1:nnz(F_D(i, :))), '-o');
307         end
308         set(p, 'Color', color(round(i/2)));
309     end
310     legend(Specimen_Name, 'Interpreter', 'latex', 'Location','eastoutside')
311     title("Natural damped frequency $\mathrm{(F_D)}$ vs. cracking level", '
            Interpreter', 'latex')
312     xlabel("Cracking level", 'Interpreter', 'latex')
313     ylabel("$\mathrm{F_D\;[Hz]}$", 'Interpreter', 'latex')
314     xticks(0:1:16);
315     yticks(0:2:20);
316     xlim([-1 17])
317     ylim([0 21])
318
319     % Mean
320     subplot(3, 1, 2)
321     grid on
322     box on
323     hold on
324
325     for i = 1:2:12
326         F_D_len = min(nnz(F_D(i, :)), nnz(F_D(i+1, :)));
327         F_D_average=(F_D(i, :)+F_D(i+1, :))/2;
328         q= plot(0:1:F_D_len-1, F_D_average(1:F_D_len), '-o');
329         set(q, 'Color', color(round(i/2)));
330     end
331
332     legend(Specimen_Name_ave, 'Interpreter', 'latex', 'Location','
            eastoutside')
333     title("Natural damped frequency $\mathrm{(F_D)}$ vs. cracking level:
            Averaged", 'Interpreter', 'latex')
334     xlabel("Cracking level", 'Interpreter', 'latex')
335     ylabel("$\mathrm{F_D\;[Hz]}$", 'Interpreter', 'latex')
336     xticks(0:1:16);
337     yticks(0:2:20);
338     xlim([-1 17])
339     ylim([0 21])
340
341     % Regression
342     subplot(3, 1, 3)
343     grid on
344     box on
345     hold on
346
347     for i = 1:2:12
348         F_D_len = min(nnz(F_D(i, :)), nnz(F_D(i+1, :)));
349         F_D_average = (F_D(i, 1:F_D_len) + F_D(i+1, 1:F_D_len)) / 2;
350
351         % Plotting the original data
```

```
352         %q= plot(0:1:F_D_len-1, F_D_average(1:F_D_len), '-o', 'Color',
                color_trans(round(i/2)));
353         %set(q, 'Color', color_trans(round(i/2)));
354
355         % Adding square regression line with the same color as the plot
356         x_values = 0:1:F_D_len-1;
357         y_values = F_D_average(1:F_D_len);
358         p = polyfit(x_values, y_values, 2);  % Fit a second-degree
                polynomial (square regression)
359         x_fit = 0:0.1:F_D_len-1;  % Generate x values for the fitted curve
360         y_fit = polyval(p, x_fit);  % Evaluate the polynomial at the x
                values
361
362         % Plotting the regression line with the same color as the plot
363         plot(x_fit, y_fit, '-', 'Color', color(round(i/2)), 'LineWidth', 2)
                ;
364     end
365
366     legend(Specimen_Name_ave, 'Interpreter', 'latex', 'Location','
            eastoutside')
367     title("Natural damped frequency $\mathrm{(F_D)}$ vs. cracking level:
            Quadratic regression", 'Interpreter', 'latex')
368     xlabel("Cracking level", 'Interpreter', 'latex')
369     ylabel("$\mathrm{F_D\;[Hz]}$", 'Interpreter', 'latex')
370     xticks(0:1:16);
371     yticks(0:2:20);
372     xlim([-1 17])
373     ylim([0 21])
374
375     saveas(gcf, 'Figures\Damping\F_D', 'epsc')
```

Program Code A.2: Prestressing force over time

```
%% Generals
clc
close all
clear all
TimeCst = 3600;
Achse_X = 24;
%Achse_Y = 10;

%% Read the data from the text file
file_path = 'C:\Users\Shahriyar Azadi\OneDrive\BI\TU Wien\- Diplomarbeit\
    Versuchsdaten\Vorspannung\Matlab\2kN.txt';
data_2kN = readmatrix(file_path, 'Delimiter', '\t', 'HeaderLines', 5, '
    DecimalSeparator', ',');

file_path = 'C:\Users\Shahriyar Azadi\OneDrive\BI\TU Wien\- Diplomarbeit\
    Versuchsdaten\Vorspannung\Matlab\4kN.txt';
data_4kN = readmatrix(file_path, 'Delimiter', '\t', 'HeaderLines', 5, '
    DecimalSeparator', ',');

file_path = 'C:\Users\Shahriyar Azadi\OneDrive\BI\TU Wien\- Diplomarbeit\
    Versuchsdaten\Vorspannung\Matlab\6kN.txt';
data_6kN = readmatrix(file_path, 'Delimiter', '\t', 'HeaderLines', 5, '
    DecimalSeparator', ',');

%% Extract data into separate arrays
%TimeAbs_2kn = data_2kN(:, 1);
Time_2kn_S = data_2kN(:, 2);
Time_2kn = Time_2kn_S./TimeCst;
F1_2kn = data_2kN(:, 3);
F2_2kn = data_2kN(:, 4);

%TimeAbs_4kn = data_4kN(:, 1);
Time_4kn_S = data_4kN(:, 1);
Time_4kn = Time_4kn_S./TimeCst;
F1_4kn = data_4kN(:, 2);
F2_4kn = data_4kN(:, 3);

%TimeAbs_6kn = data_6kN(:, 1);
Time_6kn_S = data_6kN(:, 2)-815;
Time_6kn = Time_6kn_S./TimeCst;
F1_6kn = data_6kN(:, 3);
F2_6kn = data_6kN(:, 4);


%% Plot

%plot(TimeD, F1);

% Create a new figure
figure('Position', [100, 100, 800, 800]);
box on

% Plot the first subplot
subplot(3, 1, 1);
plot(Time_2kn, F1_2kn);
hold on
grid on
plot(Time_2kn, F2_2kn);
```

```
53 title('\textbf{Specimen 1 \& 2}', 'Interpreter', 'latex');
54 xlabel('Time t [h]', 'Interpreter', 'latex'); % Set y-label with LaTeX font
55 ylabel('Prestressing Force P [kN]', 'Interpreter', 'latex'); % Set y-label
       with LaTeX font
56 legend('S1 t=12 mm P=2 kN 1-layer', 'S2 t=12 mm P=2 kN 1-layer', '
       Interpreter', 'latex');
57 xlim([0, Achse_X]);
58 ylim([0, 6]);
59 xticks(1:1:24);
60 yticks(1:1:10);
61
62 % Plot the second subplot
63 subplot(3, 1, 2);
64 plot(Time_4kn, F1_4kn);
65 hold on
66 grid on
67 plot(Time_4kn, F2_4kn);
68 title('\textbf{Specimen Nr. 3 \& 4}', 'Interpreter', 'latex');
69 xlabel('Time t [h]', 'Interpreter', 'latex'); % Set y-label with LaTeX font
70 ylabel('Prestressing Force P [kN]', 'Interpreter', 'latex'); % Set y-label
       with LaTeX font
71 legend('S3 t=12 mm P=4 kN 1-layer', 'S4 t=12 mm P=4 kN 1-layer', '
       Interpreter', 'latex');
72 xlim([0, Achse_X]);
73 ylim([0, 6]);
74 xticks(1:1:24);
75 yticks(1:1:10);
76
77 % Plot the third subplot
78 subplot(3, 1, 3);
79 plot(Time_6kn, F1_6kn);
80 hold on
81 grid on
82 plot(Time_6kn, F2_6kn);
83 title('\textbf{Specimen Nr. 5 \& 6}', 'Interpreter', 'latex');
84 xlabel('Time t [h]', 'Interpreter', 'latex'); % Set y-label with LaTeX font
85 ylabel('Prestressing Force P [kN]', 'Interpreter', 'latex'); % Set y-label
       with LaTeX font
86 legend('S5 t=12 mm P=6 kN 1-layer', 'S6 t=12 mm P=6 kN 1-layer', '
       Interpreter', 'latex');
87 xlim([0, Achse_X]);
88 ylim([0, 6]);
89 xticks(1:1:24);
90 yticks(1:1:10);
91
92 %sgtitle('Prestressing Force in Textiles over Time', 'Interpreter', 'latex
       ');
93 saveas(gcf,'Figures\Prestressing_Force','epsc')
```

Program Code A.3: Tensile test

```
%% Generals
clc
close all
clear all



%% Read the data from the text file
file_name = ["Versuch_1-Sample_1.001.txt", "Versuch_6_Sample_3.001.txt", "
    Versuch_3-Sample_5.001.txt", "Versuch_5-Sample_7.002.txt", "Versuch_5-
    Sample_7.003.txt","Versuch_2-Sample_9.001.txt", "Versuch_4-Sample_11
    .001.txt"];

Specimen_name = {'S1 t=12 mm P=2 kN 1-layer','S3 t=12 mm P=4 kN 1-layer', '
    S5 t=12 mm P=6 kN 1-layer', 'S7.1 t=12 mm P=0 kN 1-layer', 'S7.2 t=12
    mm P=0 kN 1-layer', 'S9 t=12 mm P=0 kN 2-layer', 'S11 t=18 mm P=0 kN 2-
    layer'};
b=[100, 100, 100, 100, 100, 100, 100];
h=[12, 12, 12, 12, 12, 12, 18];
l=[1000, 500, 1000, 1000, 1000, 1000, 1000];

figure('Position', [700, 100, 850, 1200]);


%% Subplots
for i = 1:length(Specimen_name)
    file_path = "C:\Users\Shahriyar Azadi\OneDrive\BI\TU Wien\-
        Diplomarbeit\Versuchsdaten\Arbeitslinie\" + file_name(i);
    data = readmatrix(file_path, 'Delimiter', '\t', 'HeaderLines', 3, '
        DecimalSeparator', ',');

    % Extract data into separate arrays
    T = data(:, 2);
    F = data(:, 3);
    stress = F*1000/(b(i)*h(i));
    W1 = data(:, 4);
    W2 = data(:, 5);
    W3 = data(:, 6);
    W4 = data(:, 7);
    WM = (W1+W2+W3+W4)/4;
    strain_1 = -W1/l(i)*1000;
    strain_2 = -W2/l(i)*1000;
    strain_3 = -W3/l(i)*1000;
    strain_4 = -W4/l(i)*1000;
    strain_M = -WM/l(i)*1000;

    Index_Max=find(F==max(F));

%     if i ~= 4
%         subplot(length(Specimen_name), 1, i);
%     end
    %subplot(length(Specimen_name), 1, i);
    subplot('Position', [0.05 1-i/length(Specimen_name)+0.025 0.90 1/(
        length(Specimen_name)+3)]); % Adjust the position and height
    title([Specimen_name(i)+"$\quad \sigma_{max} = " + num2str( round(
        stress(Index_Max) ,2) ) + "\;\mathrm{MPa} \quad F_{max} = " +
        num2str( round( F(Index_Max) ,2) ) + "\; \mathrm{kN} \quad \
```

```
        varepsilon_{max} = " + num2str( round( strain_M(Index_Max) ,2) ) +
        " \times 10^3$"], 'Interpreter', 'latex');
47      hold on
48
49      %plot(strain_1(1:Index_Max),stress(1:Index_Max), 'Color',  [.7 .7 .7],
        'LineWidth', 1);
50      %plot(strain_2(1:Index_Max),stress(1:Index_Max), 'Color',  [.7 .7 .7],
        'LineWidth', 1);
51      %plot(strain_3(1:Index_Max),stress(1:Index_Max), 'Color',  [.7 .7 .7],
        'LineWidth', 1);
52      %plot(strain_4(1:Index_Max),stress(1:Index_Max), 'Color',  [.7 .7 .7],
        'LineWidth', 1);
53      plot(strain_M(1:Index_Max),stress(1:Index_Max), 'b-', 'LineWidth', 2);
54
55      plot(strain_M(Index_Max), stress(Index_Max), 'ro', 'MarkerSize', 5); %
        Red circle marker at the maximum point
56      %text(strain(Index_Max)+0.5, stress(Index_Max)+3, ['$\sigma_{max} = ',
        num2str( round( stress(Index_Max) ,2) ), '\;\mathrm{MPa}$'], '
        Interpreter', 'latex', 'Color', 'k');
57      %text(strain(Index_Max)+0.5, stress(Index_Max)-3, ['$\varepsilon_{max}
        = ', num2str( round( strain(Index_Max) ,2) ), ' \times 10^3$'], '
        Interpreter', 'latex', 'Color', 'k');
58
59      grid on
60      box on
61      xlabel("$\varepsilon\times 10^3\;[-] $", 'Interpreter', 'latex')
62      ylabel("$\sigma\;[\mathrm{MPa}]$", 'Interpreter', 'latex')
63
64      xlim([0, 17]);
65      ylim([0, 25]);
66      %xticks(0:1:17);
67      %yticks(0:5:25);
68      % plot(-W1,F);
69      % plot(-W2,F);
70      % plot(-W3,F);
71      % plot(-W4,F);
72      %legend(Specimen_name(i), 'Interpreter', 'latex', 'Location', '
        northwest');
73
74  end
75
76  saveas(gcf,'Figures\Stress_Strain_Diagram','epsc')
77
78  %% One Plot
79  figure('Position', [700, 100, 800, 400]);
80  hold on
81  grid on
82  box on
83  xlabel("$\varepsilon\times 10^3\;[-] $", 'Interpreter', 'latex')
84  ylabel("$\sigma\;[\mathrm{MPa}]$", 'Interpreter', 'latex')
85  xlim([0, 17]);
86  ylim([0, 25]);
87
88
89  for i = 1:length(Specimen_name)
90      file_path = "C:\Users\Shahriyar Azadi\OneDrive\BI\TU Wien\-
        Diplomarbeit\Versuchsdaten\Arbeitslinie\" + file_name(i);
91      data = readmatrix(file_path, 'Delimiter', '\t', 'HeaderLines', 3, '
        DecimalSeparator', ',');
92
```

```
93      % Extract data into separate arrays
94      T = data(:, 2);
95      F = data(:, 3);
96      stress = F*1000/(b(i)*h(i));
97      W1 = data(:, 4);
98      W2 = data(:, 5);
99      W3 = data(:, 6);
100     W4 = data(:, 7);
101     WM = (W1+W2+W3+W4)/4;
102     strain_1 = -W1/l(i)*1000;
103     strain_2 = -W2/l(i)*1000;
104     strain_3 = -W3/l(i)*1000;
105     strain_4 = -W4/l(i)*1000;
106     strain_M = -WM/l(i)*1000;
107
108     Index_Max=find(F==max(F));
109
110     plot(strain_M(1:Index_Max),stress(1:Index_Max), 'LineWidth', 1);
111
112     %plot(strain_M(Index_Max), stress(Index_Max), 'ro', 'MarkerSize', 5); %
            Red circle marker at the maximum point
113
114 end
115 legend(Specimen_name)
116 %sgtitle('Stress-Strain Diagrams from Tensile Test', 'Interpreter', 'latex
        ');
117 saveas(gcf,'Figures\Stress_Strain_Diagram_one','epsc')
```

Appendix B

Prestressing Bed - Blueprint

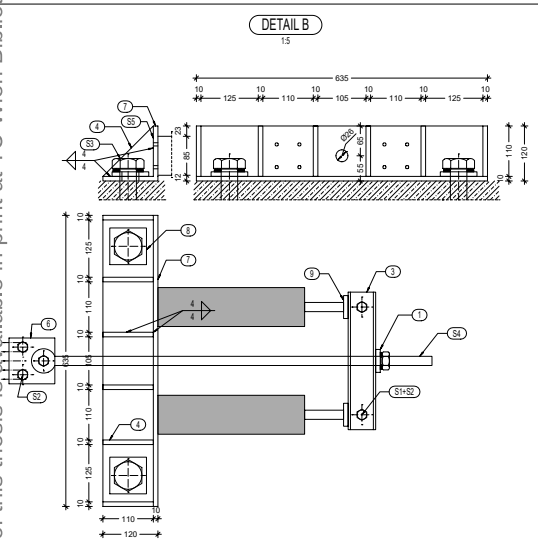

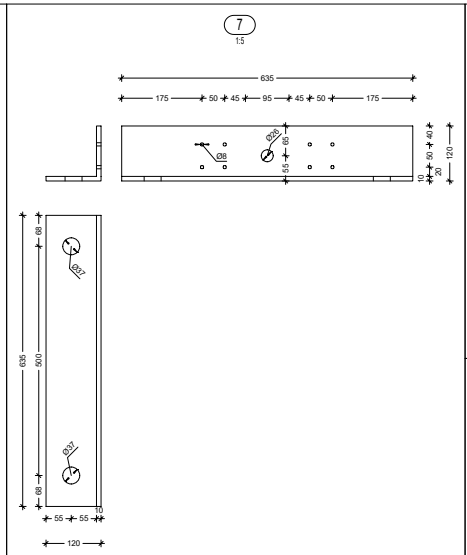

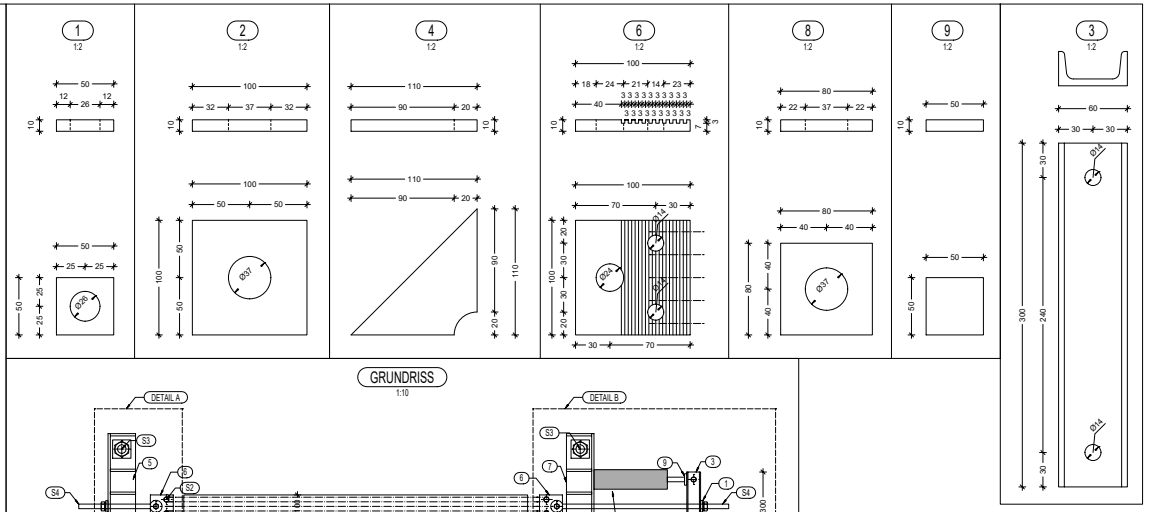

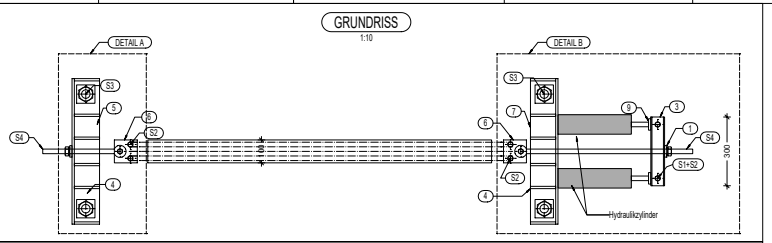

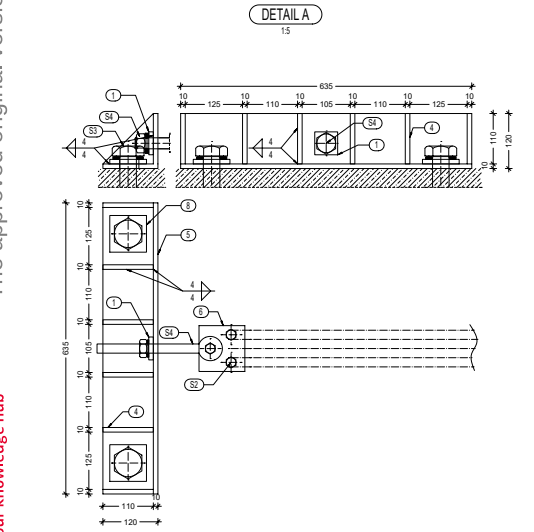

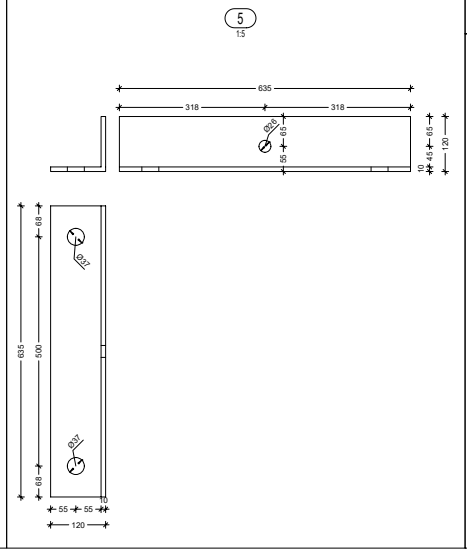

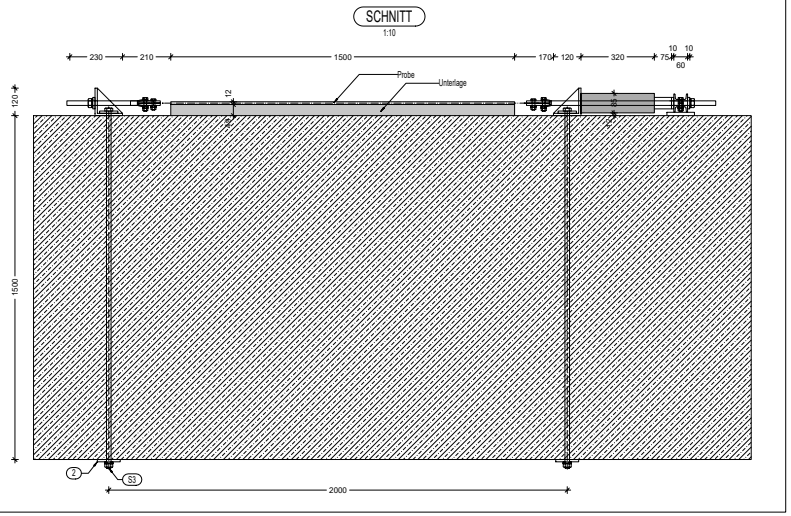

STÜCKLISTE

Herstellen		1x				
				Abmessungen		
Pos.	Werkstoff	Bezeichnung	Stk.	Querschnitt [mm]	[mm]	Länge / Dicke [mm]
1	S235	Lastplatte	3	50	50	10
2	S235	Lastplatte	4	100	100	10
3	S235	U-Profil	2	U60		300
4	S235	Steifen	12	110.110.10		
5	S235	Winkelprofil	1	120.120.10		635
6	S235	Blech	4	100.100.10		
7	S235	Winkelprofil	1	120.120.10		635
8	S235	Blech	4	80.80.10		
9	S235	Blech	2	50.50.10		
S1	8.8	*NUR* Mutter	4	M12		
S2	8.8	Schrauben + Mutter + Beilagscheibe	6	M12x40		
S3		vorh. im Labor	4	M36		
S4		vorh. im Labor	2	Schelle M24		
S5		vorh. im Labor	8	M6		

Planinhalt: **Versuchseinrichtung**	Maßstab: **1:10 / 1:5 / 1:2**
TU WIEN TECHNISCHE UNIVERSITÄT WIEN Vienna University of Technology	Plannummer: **1**
	Planverfasser: **Mohammadhossein AZADI**

H/B = 510 / 980 (0.50m²)

Allplan 2022

Appendix C

Free Vibration Test Results

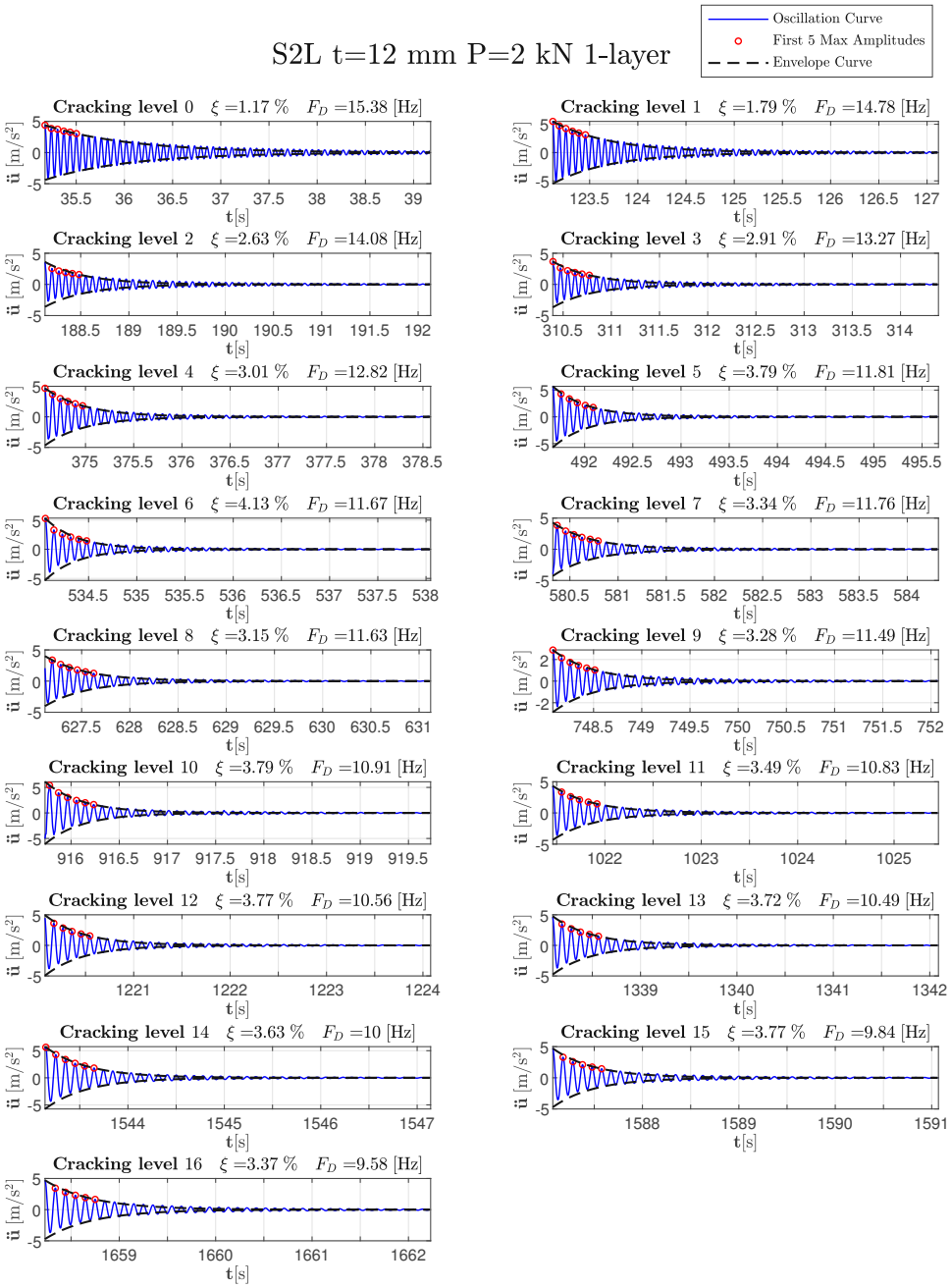

Fig. C.1: Free Vibration Test Result - Specimen S2L

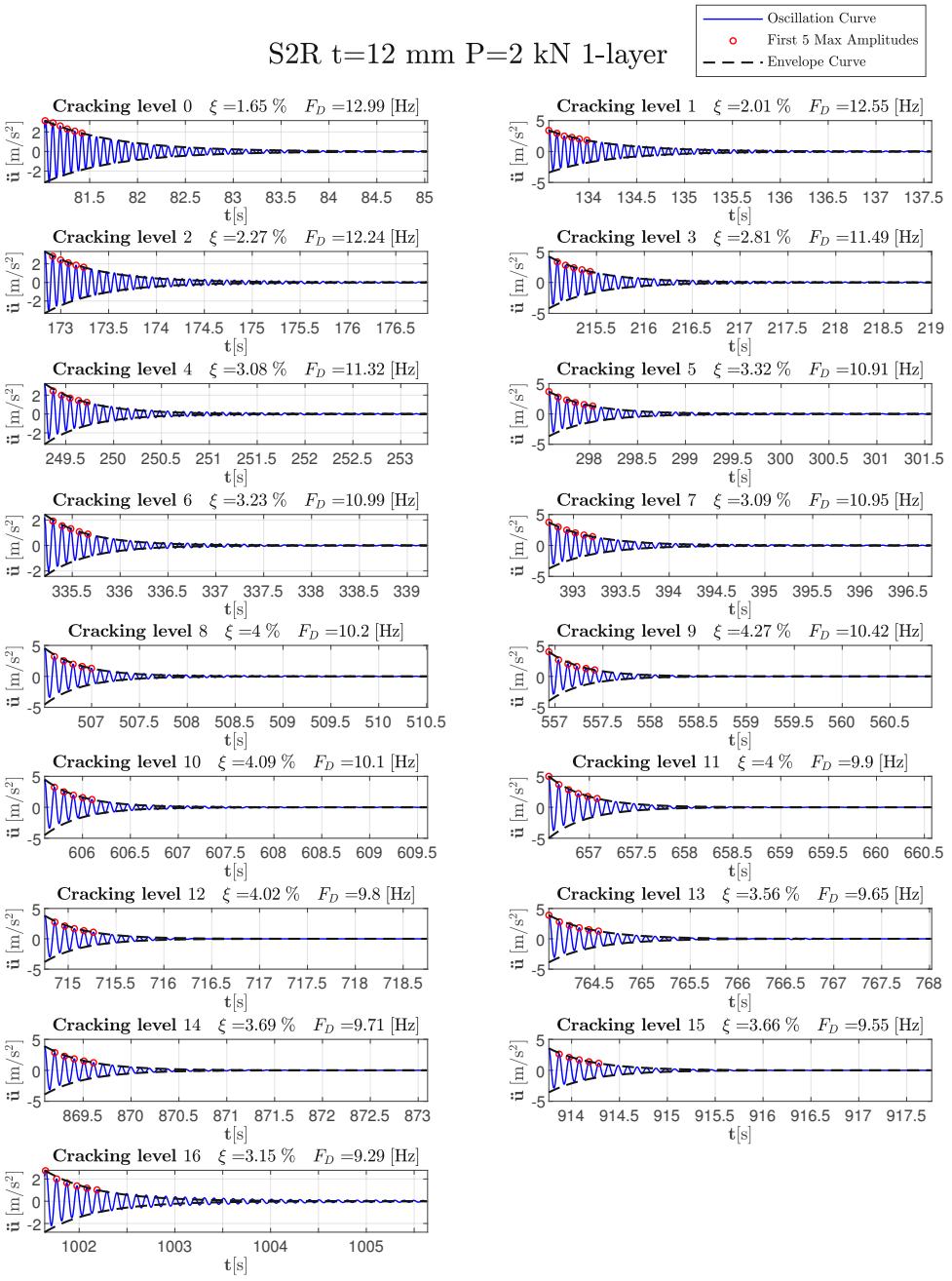

Fig. C.2: Free Vibration Test Result - Specimen S4R

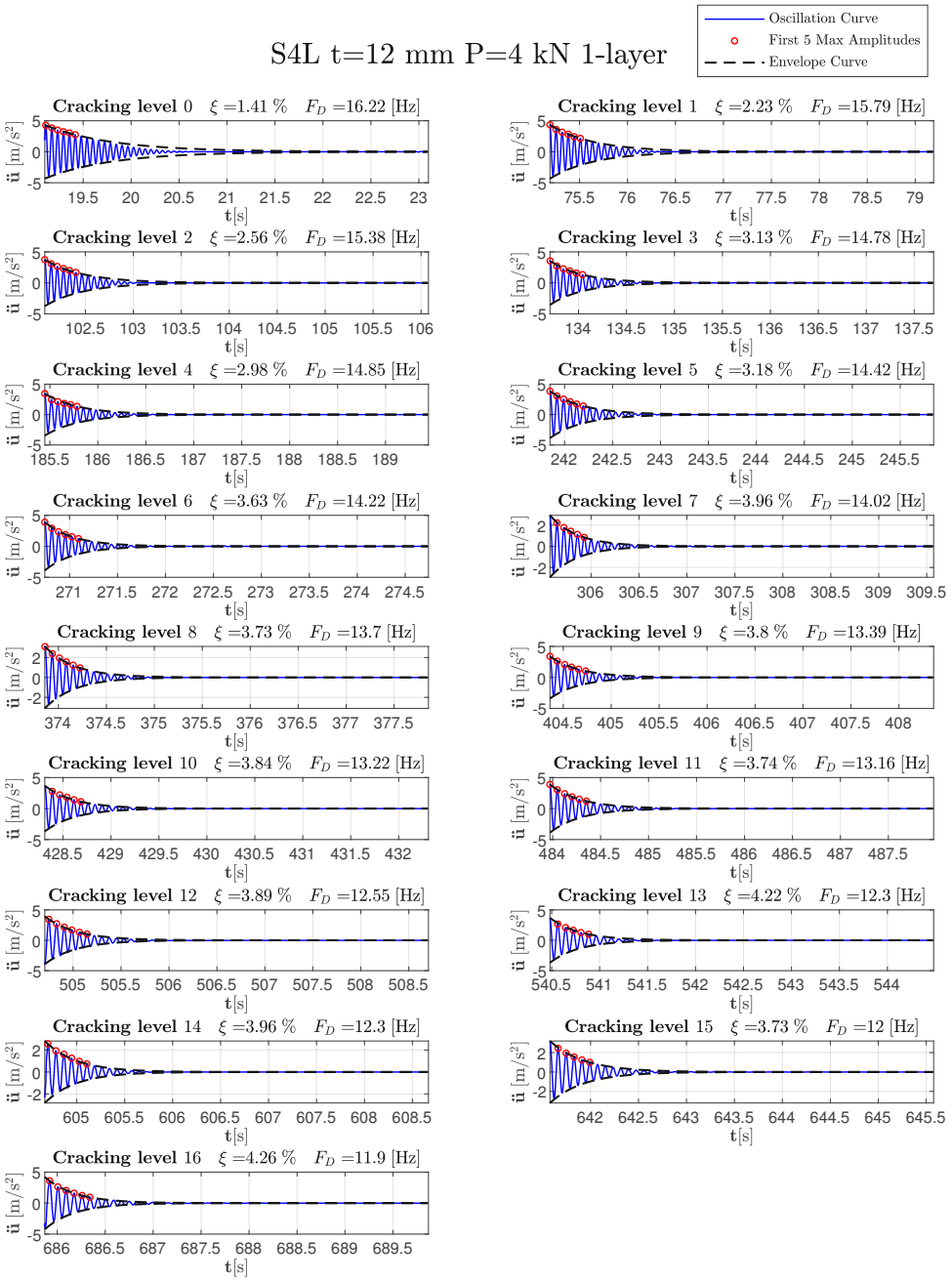

Fig. C.3: Free Vibration Test Result - Specimen S4L

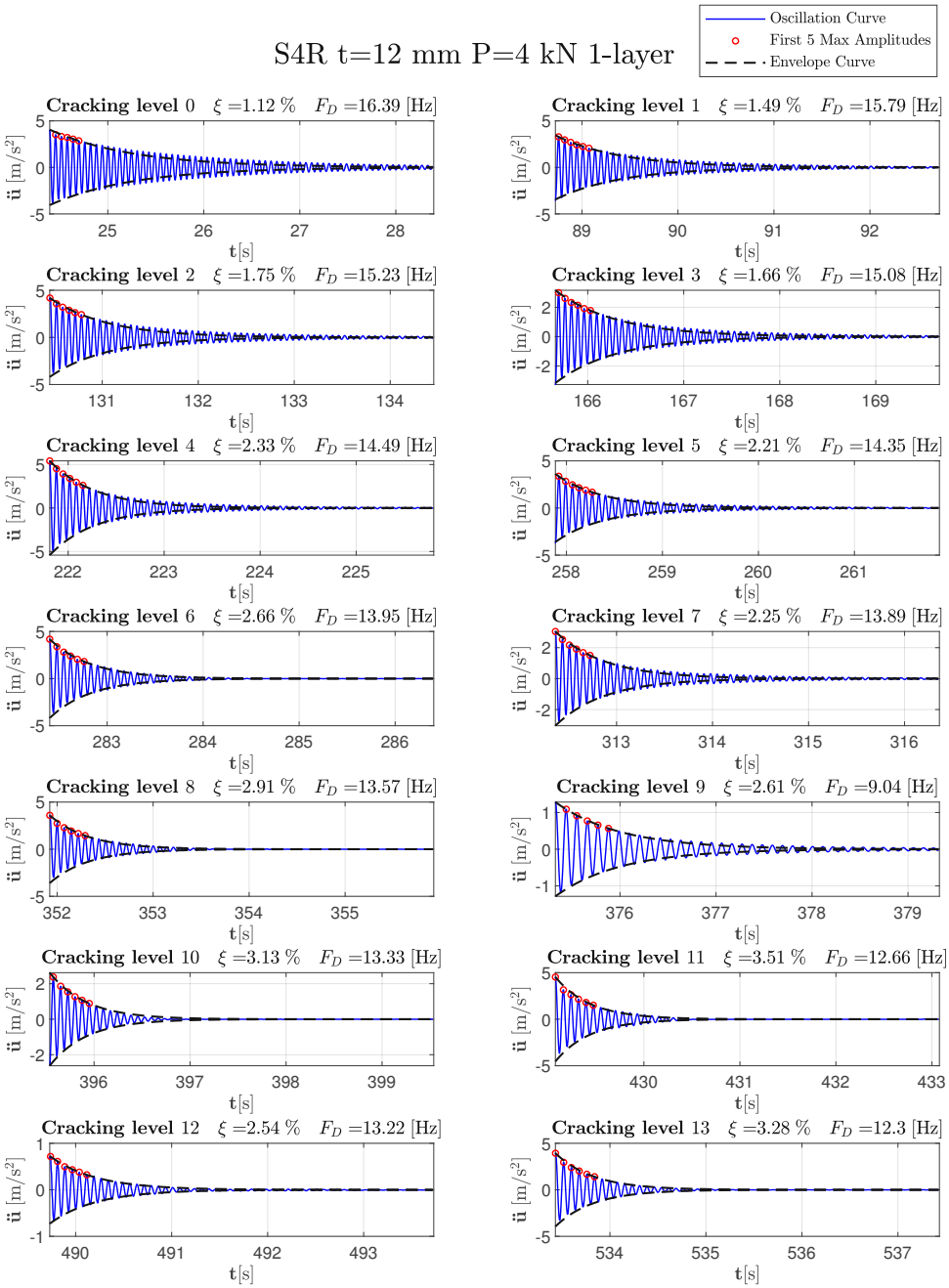

Fig. C.4: Free Vibration Test Result - Specimen S4R

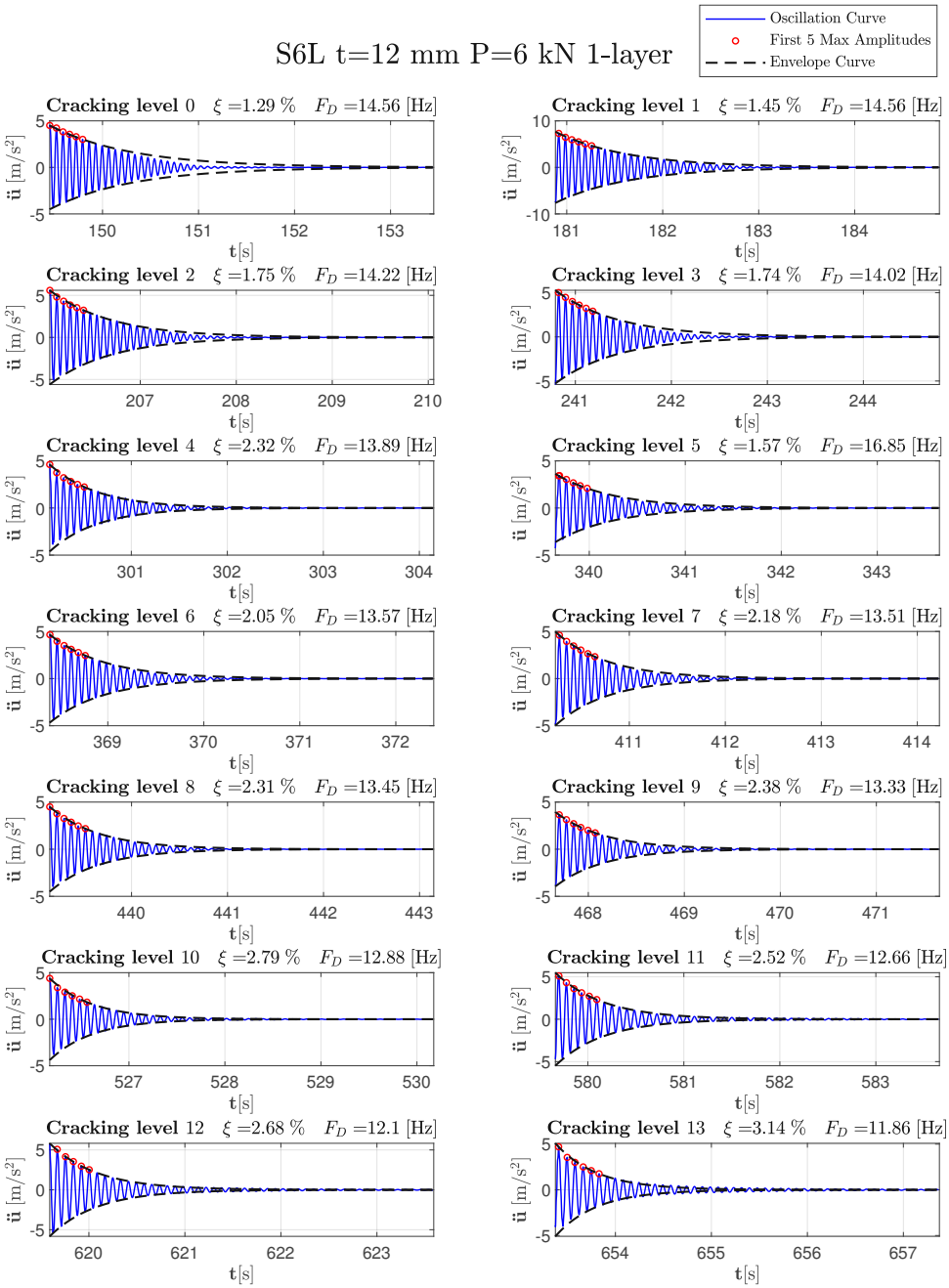

Fig. C.5: Free Vibration Test Result - Specimen S6L

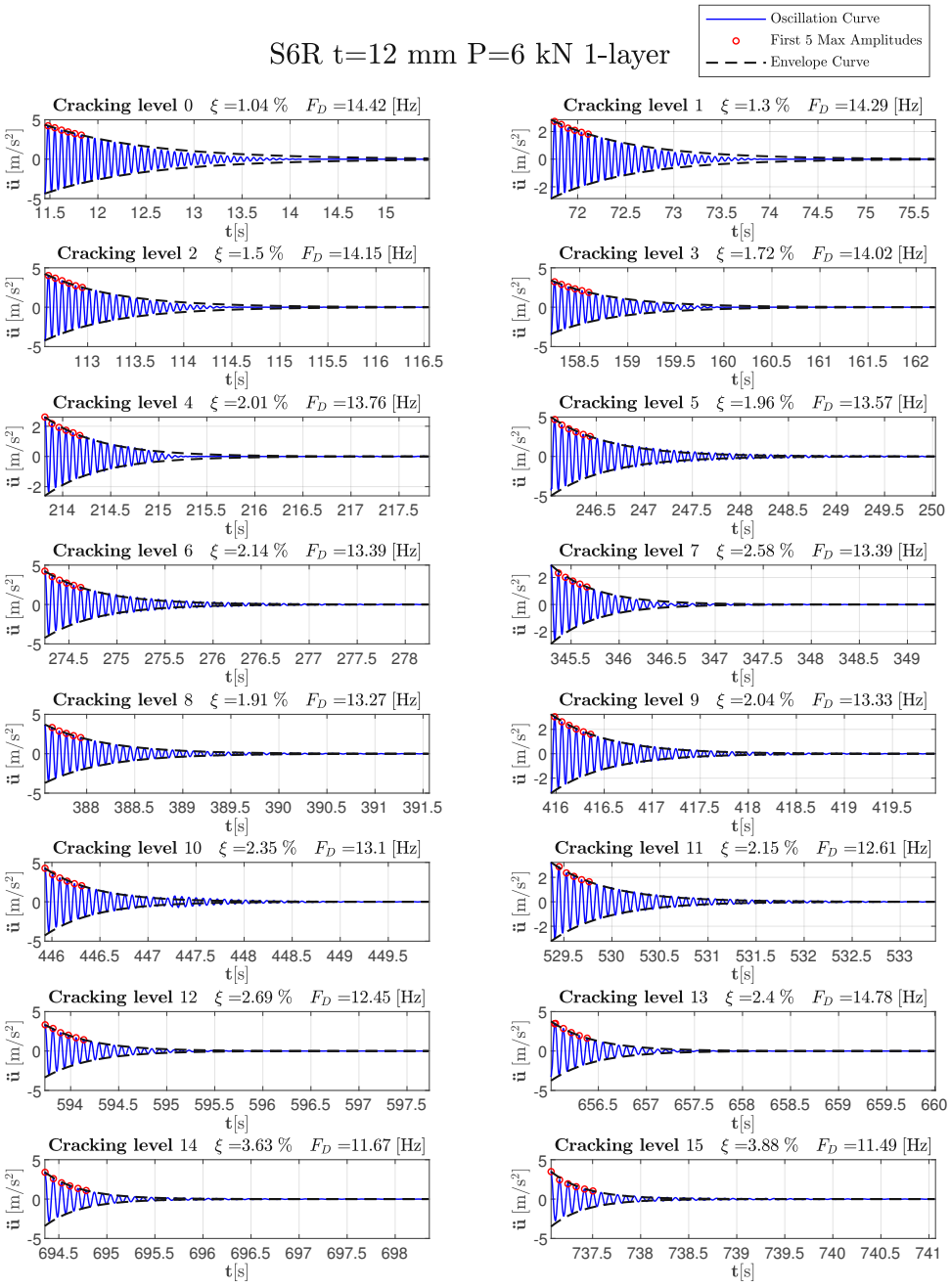

Fig. C.6: Free Vibration Test Result - Specimen S6R

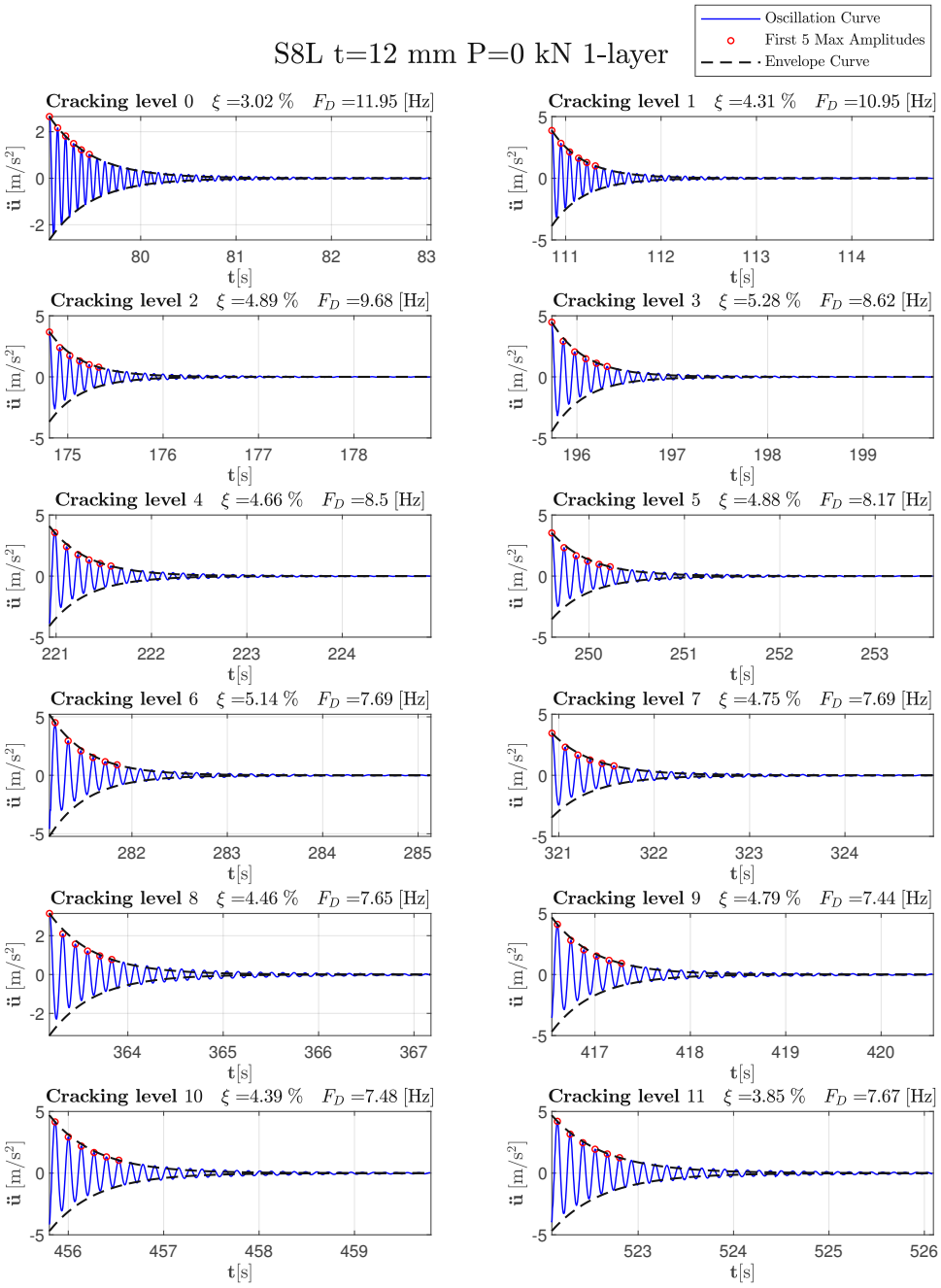

Fig. C.7: Free Vibration Test Result - Specimen S8L

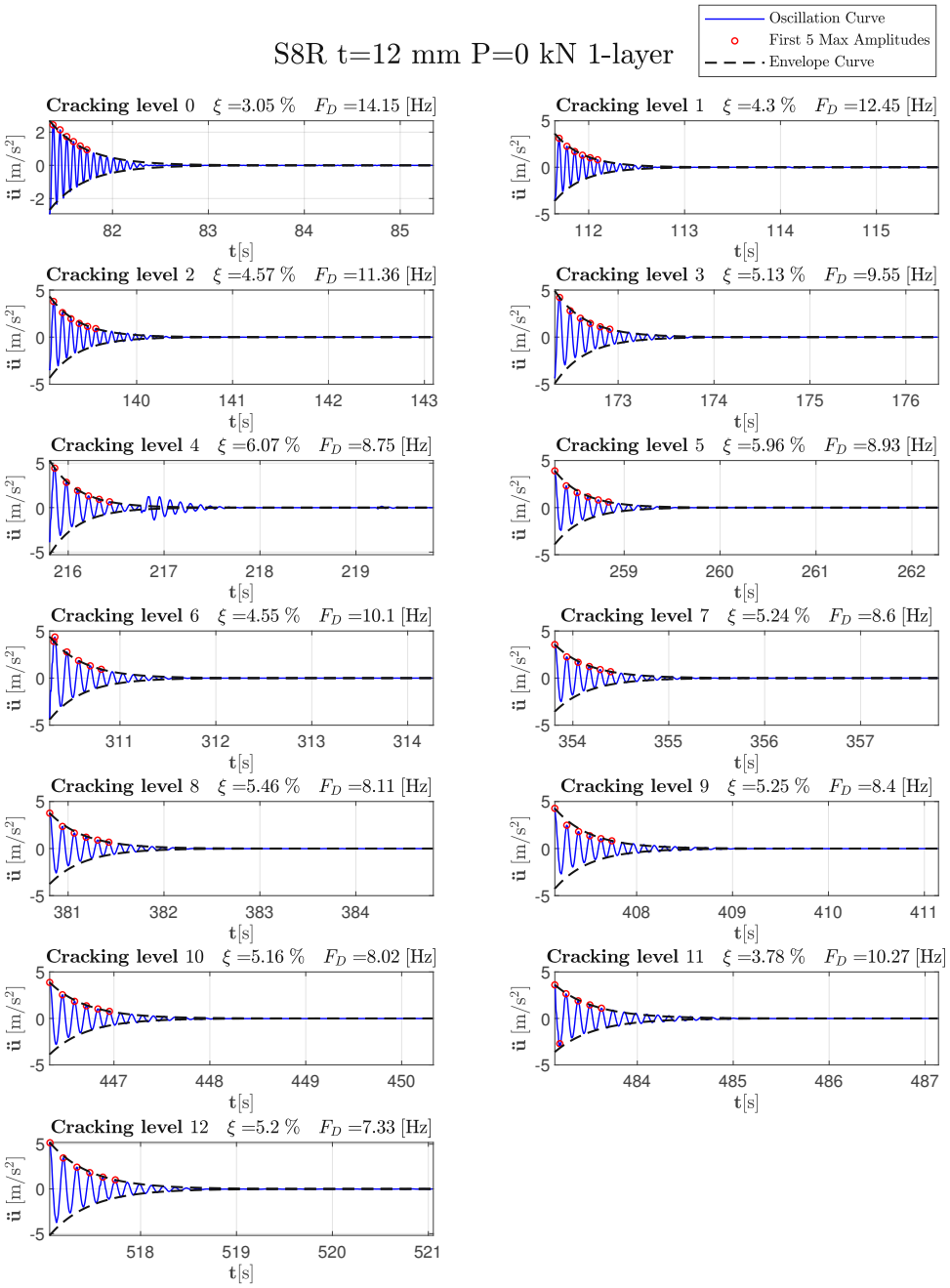

Fig. C.8: Free Vibration Test Result - Specimen S8R

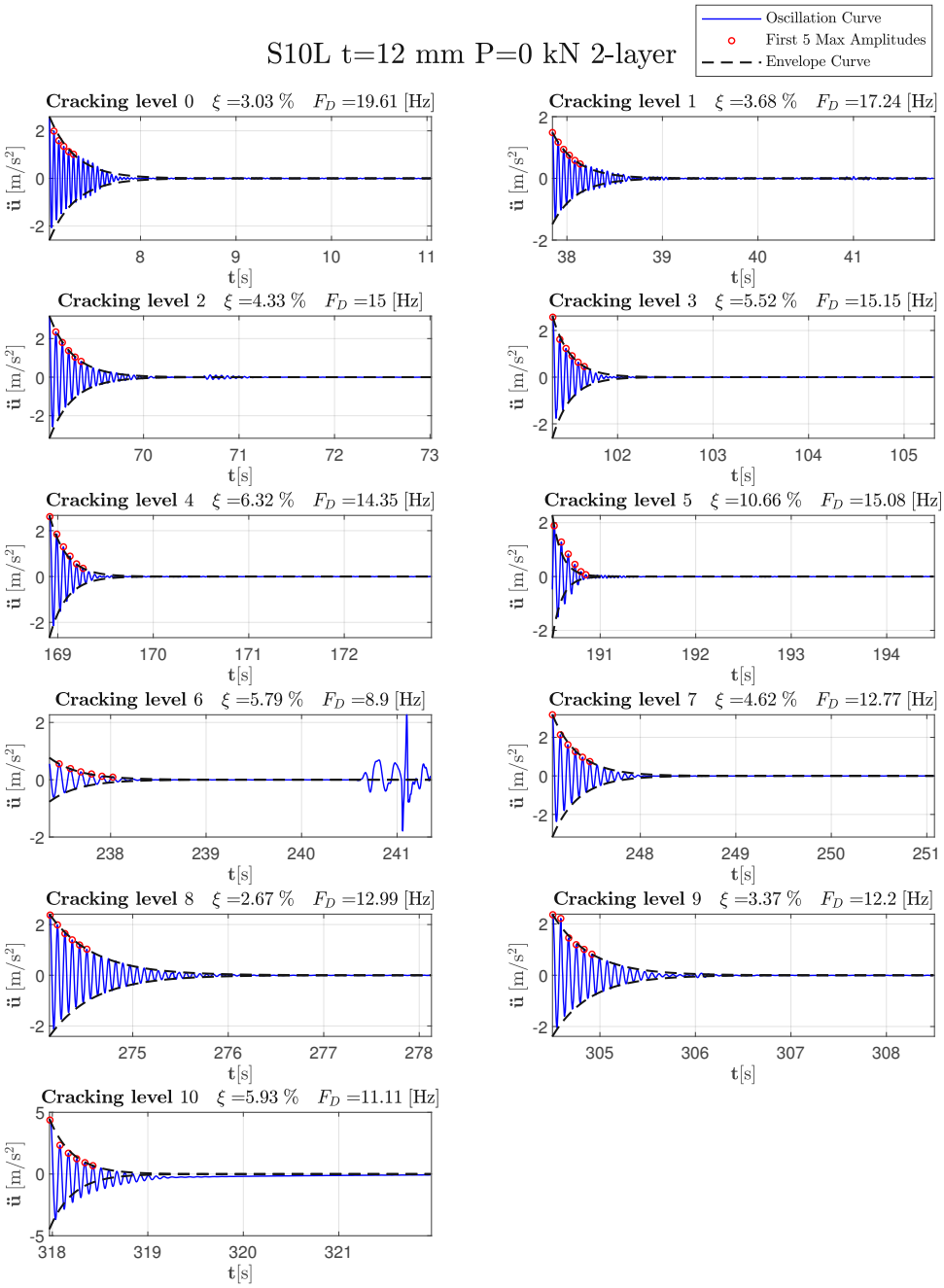

Fig. C.9: Free Vibration Test Result - Specimen S10L

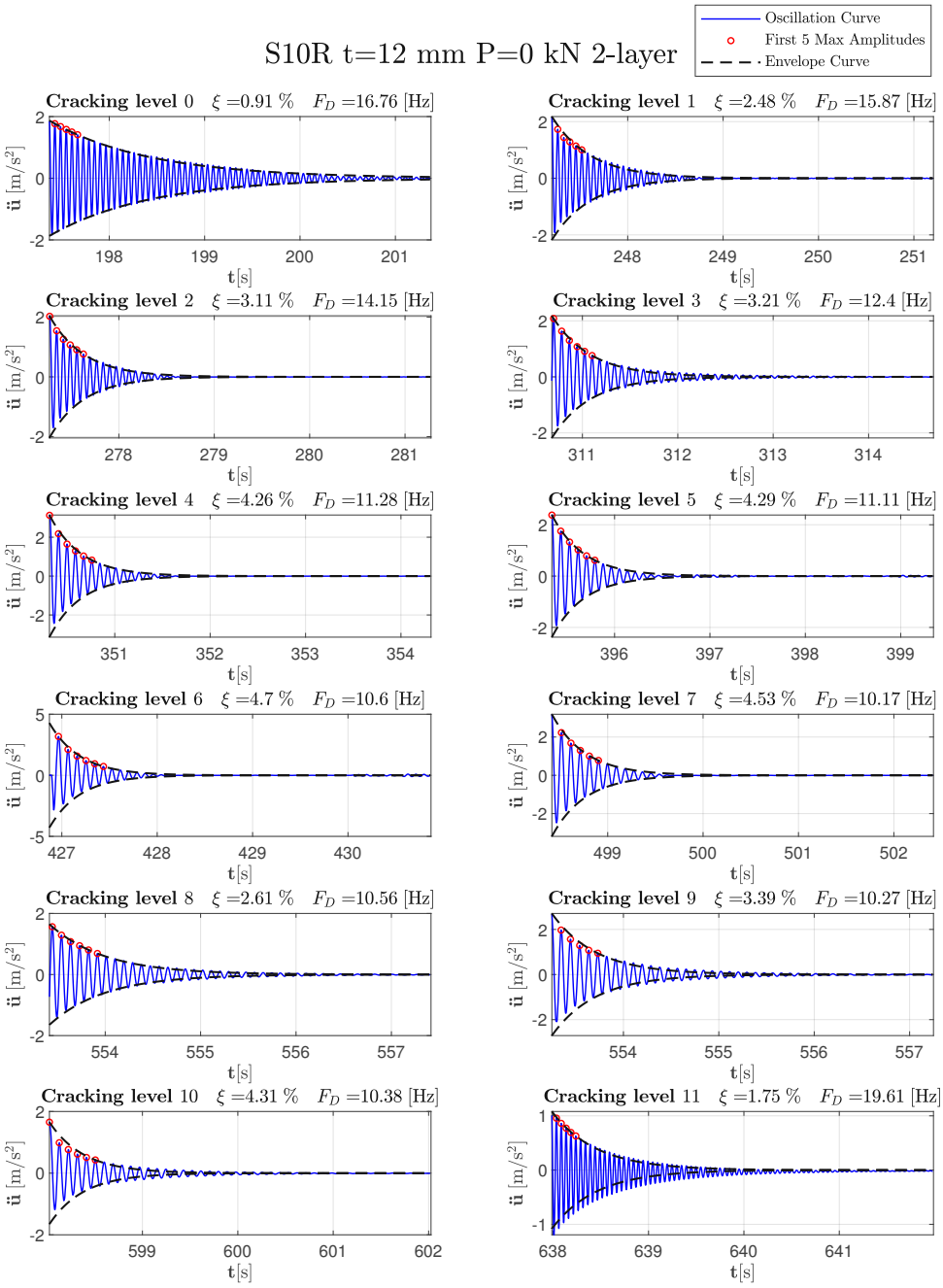

Fig. C.10: Free Vibration Test Result - Specimen S10R

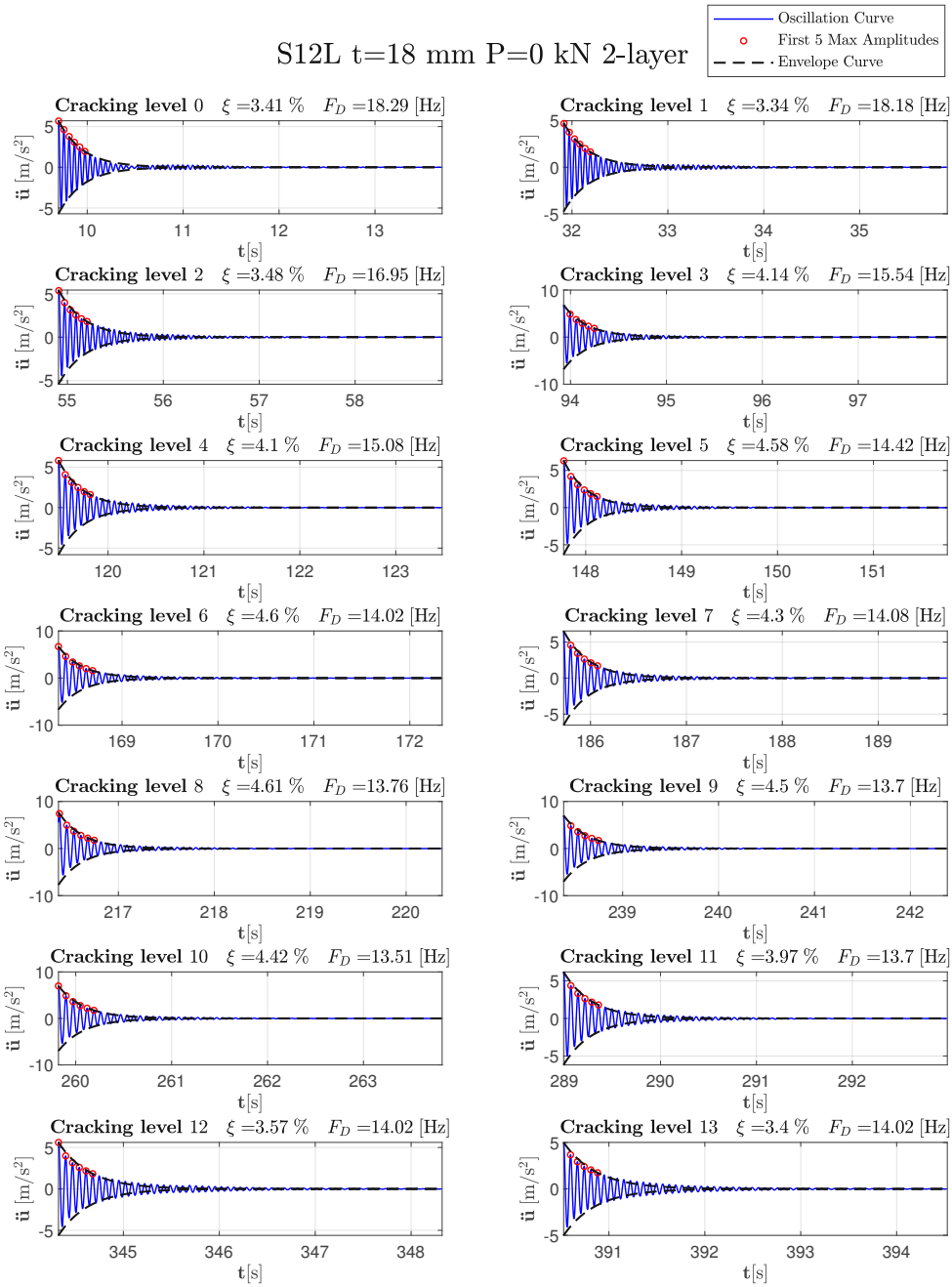

Fig. C.11: Free Vibration Test Result - Specimen S12L

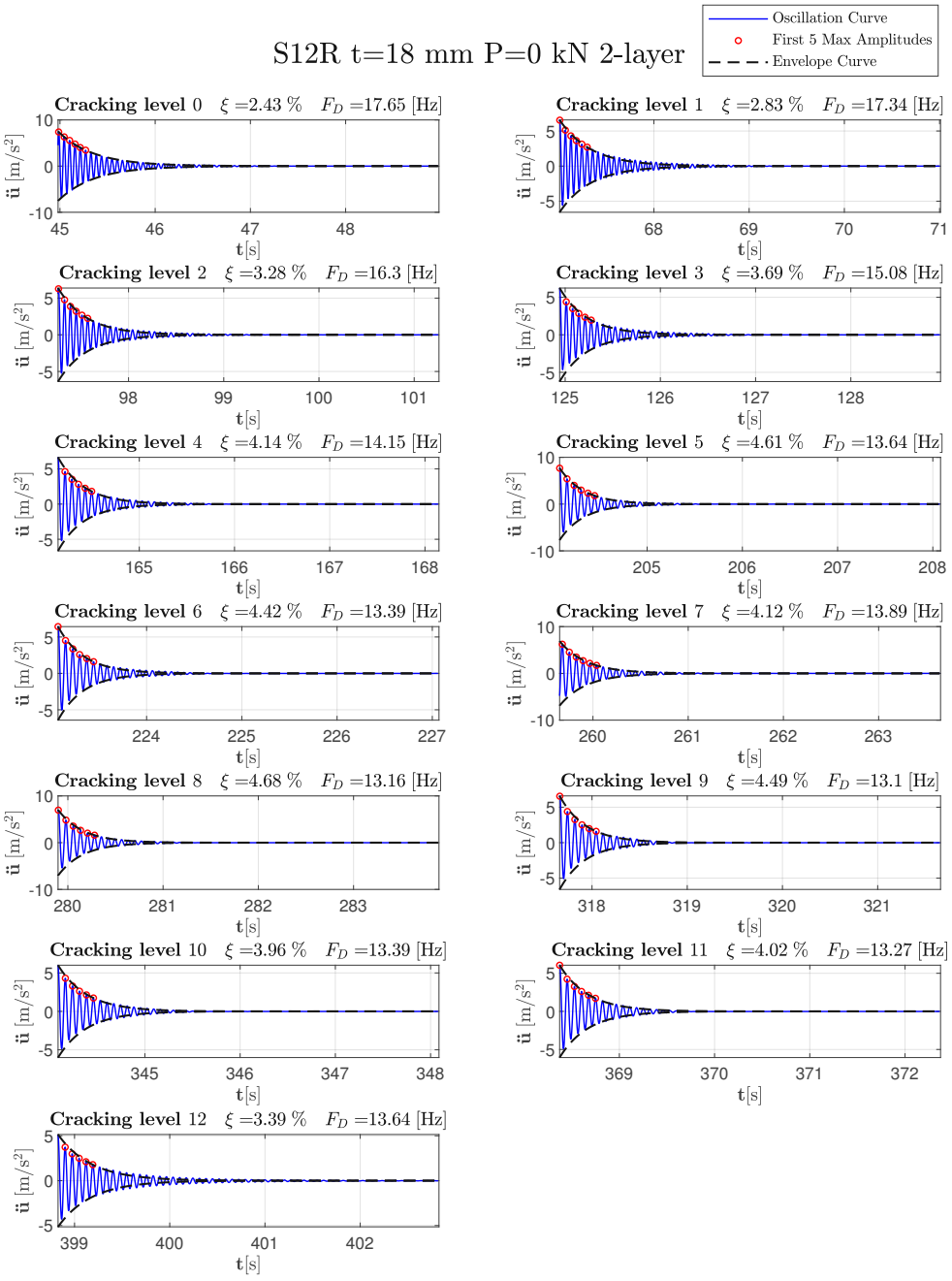

Fig. C.12: Free Vibration Test Result - Specimen S12R

Appendix D

Flexural and Compressive Strength Tests on Mortar Prisms

		Concreted on	Tested on	Age	Dimensions			Volume	Weight	Density	Compressive strength			Bending tensile strength
					h	b	l				$f_{c,1}$	$f_{c,2}$	$f_{c,M}$	f_{ct}
				[days]	[mm]	[mm]	[mm]	[mm^3]	[gr]	[kg/m^3]	[N/mm^2]	[N/mm^2]	[N/mm^2]	[N/mm^2]
P1	I	04.10.2023	01.11.2023	28	40,1	40,0	160,0	256640	546,1	2127,88	126,13	127,88	127,00	14,27
	II				40,0	40,0	160,0	256000	545,2	2129,69	130,06	128,75	129,41	12,48
	III				40,1	40,0	160,0	256640	544,9	2123,21	126,81	127,81	127,31	12,73
									Mean Value:	**2126,93**			**127,91**	**13,16**

		Concreted on	Tested on	Age	Dimensions			Volume	Weight	Density	Compressive strength			Bending tensile strength
					h	b	l				$f_{c,1}$	$f_{c,2}$	$f_{c,M}$	f_{ct}
				[days]	[mm]	[mm]	[mm]	[mm^3]	[gr]	[kg/m^3]	[N/mm^2]	[N/mm^2]	[N/mm^2]	[N/mm^2]
P2	I	18.10.2023	26.02.2024	131	40,3	41,0	159,7	263872	639,5	2423,52	124,50	139,81	132,16	14,70
	II				40,0	40,0	160,0	256000	652,3	2548,05	141,32	137,97	139,65	15,00
	III				40,1	40,0	160,0	256640	644	2509,35	138,21	140,64	139,43	14,74
									Mean Value:	**2493,64**			**137,08**	**14,81**

		Concreted on	Tested on	Age	Dimensions			Volume	Weight	Density	Compressive strength			Bending tensile strength
					h	b	l				$f_{c,1}$	$f_{c,2}$	$f_{c,M}$	f_{ct}
				[days]	[mm]	[mm]	[mm]	[mm^3]	[gr]	[kg/m^3]	[N/mm^2]	[N/mm^2]	[N/mm^2]	[N/mm^2]
P3	I	13.11.2023	26.02.2024	105	39,1	39,8	160,2	249300	614,7	2465,70	131,59	132,18	131,89	12,43
	II				40,5	38,5	160,0	249480	604,1	2421,44	124,53	121,48	123,01	12,86
	III				40,0	40,2	160,1	257441	628,2	2440,17	127,85	140,79	134,32	12,53
									Mean Value:	**2442,44**			**129,74**	**12,61**

		Concreted on	Tested on	Age	Dimensions			Volume	Weight	Density	Compressive strength			Bending tensile strength
					h	b	l				$f_{c,1}$	$f_{c,2}$	$f_{c,M}$	f_{ct}
				[days]	[mm]	[mm]	[mm]	[mm^3]	[gr]	[kg/m^3]	[N/mm^2]	[N/mm^2]	[N/mm^2]	[N/mm^2]
P4	I	15.11.2023	26.02.2024	103	40,2	39,7	160,0	255350	617,8	2419,42	131,41	119,60	125,51	14,27
	II				40,4	38,8	159,8	250490	614,1	2451,60	116,35	118,35	117,35	12,48
	III				40,2	39,1	159,3	250391	610,2	2436,99	115,11	117,46	116,29	12,73
									Mean Value:	**2436,00**			**119,71**	**13,16**

		Concreted on	Tested on	Age	Dimensions			Volume	Weight	Density	Compressive strength			Bending tensile strength
					h	b	l				$f_{c,1}$	$f_{c,2}$	$f_{c,M}$	f_{ct}
				[days]	[mm]	[mm]	[mm]	[mm^3]	[gr]	[kg/m^3]	[N/mm^2]	[N/mm^2]	[N/mm^2]	[N/mm^2]
P5	I	22.11.2023	26.02.2024	96	40,3	41,0	159,0	262716	627,2	2387,37	112,12	118,47	115,30	11,57
	II				40,4	39,4	159,2	253408	608,8	2402,45	122,98	135,98	129,48	11,95
	III				40,6	38,0	158,9	245151	585,3	2387,51	130,10	124,05	127,08	12,36
									Mean Value:	**2392,44**			**123,95**	**11,96**

		Concreted on	Tested on	Age	Dimensions			Volume	Weight	Density	Compressive strength			Bending tensile strength
					h	b	l				$f_{c,1}$	$f_{c,2}$	$f_{c,M}$	f_{ct}
				[days]	[mm]	[mm]	[mm]	[mm^3]	[gr]	[kg/m^3]	[N/mm^2]	[N/mm^2]	[N/mm^2]	[N/mm^2]
P6	I	15.11.2023	26.02.2024	103	40,4	41,0	160,0	265024	641,1	2419,03	115,92	98,91	107,42	15,70
	II				41,0	40,5	161,0	267341	654,9	2449,68	132,54	135,03	133,79	13,33
	III				41,0	40,3	159,4	263377	644,5	2447,07	121,78	124,88	123,33	13,21
									Mean Value:	**2438,59**			**121,51**	**14,08**